

Tor Briseid Tjugum
Meron Tesfamariam Teclé

Estimation of Long-Term Extreme Response of Floating Bridges

Master's thesis in Civil and Environmental Engineering
Supervisor: Ole Andre Øiseth
Co-supervisor: Aksel Fenerci, Knut Andreas Kvåle
June 2021



(Photo: John Spooner, 2016)

Tor Briseid Tjugum
Meron Tesfamariam Teclé

Estimation of Long-Term Extreme Response of Floating Bridges

Master's thesis in Civil and Environmental Engineering
Supervisor: Ole Andre Øiseth
Co-supervisor: Aksel Fenerci, Knut Andreas Kvåle
June 2021



Norwegian University of Science and Technology
Faculty of Engineering
Department of Structural Engineering





MASTER THESIS 2021

SUBJECT AREA: Structural Dynamics	DATE: 12.06.21	NO. OF PAGES: 150 29 + 105 + 16
--------------------------------------	-------------------	------------------------------------

TITLE: Estimation of Long-Term Extreme Response of Floating Bridges Estimering av langtids ekstremrespons for flytebruer	
BY: Tor Briseid Tjugum	
BY: Meron Tesfamariam Tecele	

SUMMARY:

In the estimation of long-term extreme responses of a structure, the method of Full Integration is often recognized as the most accurate approach. However, challenges arise when complex structures such as floating bridges are to be investigated. Despite the accuracy of the method, the computational expense and run-time of this approach cannot be ignored. Therefore, in this thesis alternative methods for estimation of long-term extreme responses for floating bridges are compared to the Full Integration approach. In this comparison, emphasis is laid on both the accuracy and efficiency of these methods.

Among the considered methods in this project are the Inverse First-Order Reliability Method (IFORM), the Environmental Contour Method (ECM) and Monte Carlo Simulation (MCS) with Importance Sampling (IS). Finally, the potential application of Gaussian Process Regression (GPR) in performing long-term structural response analysis is investigated. For demonstration, all these methods are applied in long-term analyses of a simplified floating bridge model. This model resembles the Bergsøysund Bridge, located between Aspøya and Bergsøya in the north-western part of Norway. The modelling and analysis of the waterborne pontoons are carried out in GenieE and HydroD, both being software solutions developed by Det Norske Veritas (DNV). The simplified finite element model of the bridge superstructure including the pontoon data from HydroD is generated and analysed in Abaqus from which the undamped natural frequencies and the mass normalized modal vectors are retrieved. By use of the WAWI-toolbox developed at the Department of Structural Engineering at NTNU the response spectrum of the structure is calculated.

Regarding the methods for long-term analysis, both IFORM and ECM showed quite high accuracy with a maximum deviation of less than 5.7 % towards the conservative side when compared to Full Integration. This modest deviation is also to a certain degree compensated by the high efficiency of these methods. Monte Carlo Simulation with Importance Sampling based on the results obtained from IFORM overestimated the response but showed in general sufficient accuracy as well as efficiency.

RESPONSIBLE TEACHER: Ole Andre Øiseth

SUPERVISOR(S): Ole Andre Øiseth, Aksel Fenerci, Knut Andreas Kvåle

CARRIED OUT AT: Department of Structural Engineering, NTNU

Preface

This thesis is written as a finalization of our master's degree program at the Department of Structural Engineering at the Norwegian University of Science and Technology (NTNU) in Trondheim. The research and writing of this dissertation is conducted from January to June 2021.

Developing this thesis has been both interesting and highly educational. Our understanding of methods for estimation of long-term extreme responses as well as for structural dynamics in general has gained great depth.

We would like to thank our main supervisor Professor Ole Andre Øiseth for his guidance and for the opportunity to work with this fascinating topic. Our gratitude also goes to Associate Professor Aksel Fenerci and postdoctoral fellow Knut Andreas Kvåle for their continuous support from start to finish. Their eagerness to assist even long past working hours has been highly appreciated. This thesis would not have been possible without their essential input.

Meron Tesfamariam Tecele

Tor Briseid Tjugum

Trondheim, June 2021

Summary

In the estimation of long-term extreme responses of a structure, the method of Full Integration is often recognized as the most accurate approach. However, challenges arise when complex structures such as floating bridges are to be investigated. Despite the accuracy of the method, the computational expense and run-time of this approach cannot be ignored. Therefore, in this thesis alternative methods for estimation of long-term extreme responses for floating bridges are compared to the Full Integration approach. In this comparison, emphasis is laid on both the accuracy and efficiency of these methods.

Among the considered methods in this project are the Inverse First-Order Reliability Method (IFORM), the Environmental Contour Method (ECM) and Monte Carlo Simulation (MCS) with Importance Sampling (IS). Finally, the potential application of Gaussian Process Regression (GPR) in performing long-term structural response analysis is investigated. For demonstration, all these methods are applied in long-term analyses of a simplified floating bridge model. This model resembles the Bergsøysund Bridge, located between Aspøya and Bergsøya in the north-western part of Norway. The modelling and analysis of the waterborne pontoons are carried out in GenieE and HydroD, both being software solutions developed by Det Norske Veritas (DNV). The simplified finite element model of the bridge superstructure including the pontoon data from HydroD is generated and analysed in Abaqus from which the undamped natural frequencies and the mass normalized modal vectors are retrieved. By use of the WAWI-toolbox developed at the Department of Structural Engineering at NTNU the response spectrum of the structure is calculated.

Regarding the methods for long-term analysis, both IFORM and ECM showed quite high accuracy with a maximum deviation of less than 5.7 % towards the conservative side when compared to Full Integration. This modest deviation is also to a certain degree compensated by the high efficiency of these methods. Monte Carlo Simulation with Importance Sampling based on the results obtained from IFORM overestimated the response but showed in general sufficient accuracy as well as efficiency.

Sammendrag

Ved beregning av langtids ekstremrespons for en gitt konstruksjon er som oftest metoden kalt Full Integrasjon anerkjent som den mest nøyaktige. Enkelte utfordringer kan likevel oppstå når komplekse konstruksjoner slik som flytebruer skal undersøkes. Til tross for metodens høye nøyaktighet kan hverken beregningskostnaden eller kjøretiden for denne metoden ignoreres. I denne avhandlingen blir derfor alternative metoder for estimering av langtids ekstremrespons av flytebruer undersøkt og sammenlignet med Full Integrasjon-tilnærmingen. I sammenligningen rettes fokuset både på nøyaktigheten og effektiviteten til disse alternative metodene.

Blant de undersøkte metodene i dette prosjektet er den såkalte Inverse First-Order Reliability Method (IFORM), Environmental Contour Method (ECM) og Monte Carlo Simulering (MCS) med Importance Sampling (IP). I tillegg undersøkes potensialet til Gaussian Process Regression (GPR) for bruk i forbindelse med langtids responsanalyse. Alle de undersøkte metodene er eksemplifisert ved bruk av en forenklet flytebrumodell. Modellen er basert på parametere fra Bergsøysundbrua, en bru som ligger mellom Aspøya og Bergsøya på nordvestlandet. Modelleringen og analysen av bruas pongtonger er utført i GenieE og HydroD, som begge er programvareløsninger utviklet av Det Norske Veritas (DNV). Den forenklete elementmodellen av bruas bæresystem inkludert pongtongdata fra HydroD er generert og analysert i Abaqus. Derfra hentes de udempede naturlige frekvensene og de massenormaliserte modevektorene. Ved hjelp av WAWI-pakken utviklet ved institutt for konstruksjonsteknikk ved NTNU blir responspekteret for konstruksjonen beregnet.

Når det gjelder metodene for langtidsanalyse viste både IFORM og ECM høy grad av nøyaktighet med et maksimalt avvik på mindre enn 5.7 % mot den konservative siden, sammenlignet med Full Integrasjon. Dette beskjedne avviket kompenseres dessuten til en viss grad av den høye effektiviteten til disse metodene. Monte Carlo Simulering med Importance Sampling basert på resultatene fra IFORM overestimerte responsen, men viste generelt tilstrekkelig nøyaktighet og effektivitet.

Abbreviations and Symbols

The following lists describe the abbreviations used throughout the whole thesis, as well as the symbols used in each section.

Abbreviations

NTNU	Norwegian University of Science and Technology
PDF	Probability Density Function
CDF	Cumulative Distribution Function
FORM	First-Order Reliability Method
IFORM	Inverse First-Order Reliability Method
ECM	Environmental Contour Method
FEM	Finite Element Method
DOFs	Degrees-of-Freedom
MCS	Monte Carlo Simulation
DNV	Det Norske Veritas
GPR	Gaussian Process Regression
IS	Importance Sampling
JONSWAP	Joint North Sea Wave Project
WADAM	Wave Analysis by Diffraction and Morison Theory
ISMCS	Importance Sampled Monte Carlo Simulation
SINTEF	The Foundation for Scientific and Industrial Research at the Norwegian Institute of Technology

Symbols

Stochastic Loading and Random Vibrations

$x_i(t)$	Stochastic realization of load or response process
t_i	Time variable for a given time series i
R_{x_i}	Auto-correlation function for the stochastic process x_i
$\mathbb{E}[\cdot]$	Expected value operator
τ	Time lag
$R_{x_i x_j}$	Cross-correlation function for the stochastic processes x_i and x_j

Fourier Transform and Frequency Analysis

$x(t)$	Stochastic process in the time domain
$x(\omega)$	Stochastic process in the frequency domain
i	Imaginary unit

Modal Analysis

\mathbf{M}	Mass matrix
\mathbf{K}	Stiffness matrix
$\ddot{\mathbf{u}}$	Acceleration vector
\mathbf{u}	Displacement vector
\mathbf{u}_0	Displacement amplitude
t	Time variable
ω	Frequency variable
n	Number of DOFs in considered structural system
ω_i	Eigenfrequency corresponding to mode i
$\mathbf{u}_{0,i}$	Eigenvector corresponding to mode i
ϕ_i	Mass normalized mode shape vector for mode i

α Mass normalization scaling factor

The Frequency Response Method

$\mathbf{p}(t)$ Load vector

$\dot{\mathbf{u}}(t)$ Velocity vector

ω_n^2 Squared natural frequency

ξ Damping ratio

β Frequency ratio

$\mathbf{H}(\omega)$ Frequency response function

θ Phase angle

y_0 Response amplitude

x_0 Load amplitude

Spectral Densities and Moments

S_{x_i} Two-sided auto-spectral density for the stochastic process x_i

$S_{x_i x_j}$ Two-sided cross-spectral density for the stochastic process x_i and x_j

μ_n n-th order two-sided spectral moment

$\dot{x}_i(t)$ Time derivative of the stochastic process $x_i(t)$

$\ddot{x}_i(t)$ Double time derivative of the stochastic process $x_i(t)$

$x_i^{(n)}(t)$ n-th order time derivative of the stochastic process $x_i(t)$

G_{x_i} One-sided auto-spectral density for the stochastic process x_i

m_n n-th order one-sided spectral moment

Short-Term Extreme Values

\tilde{T} Short-term period

$X(t)$ Stochastic response process

r Response parameter

$\nu_X(r)$	Upcrossing rate of the stochastic process $X(t)$ for a response level r
\dot{x}	Time derivative of the response realization x of the stochastic process $X(t)$
$f_{X\dot{X}}(r, \dot{x})$	Joint probability density function of the stochastic response process X and its time derivative \dot{X}
$\nu_X(0)$	Zero-crossing rate of the stochastic process $X(t)$
N_X	Average number of upcrossings
T	Time period
$X_p(t)$	Stochastic process describing the peaks of the stochastic process $X(t)$
F_{X_p}	Cumulative distribution function for stochastic peak process
f_{X_p}	Probability density function for stochastic peak process
m_X	Mean value of stochastic process $X(t)$
σ_X	Standard deviation of the stochastic process $X(t)$
$m_{\dot{X}}$	Mean value of the stochastic process $\dot{X}(t)$
$\sigma_{\dot{X}}$	Standard deviation of the stochastic process $\dot{X}(t)$
$M(\tilde{T})$	Maximum value of $X(t)$ during the short-term period \tilde{T}
$F_{\tilde{R}}(r)$	Cumulative distribution function of the random number of upcrossings of level r
\mathbf{W}	Stochastic environmental parameters
\mathbf{w}	Realization of stochastic environmental parameters
$F_{\tilde{R} \mathbf{W}}(r \mathbf{w})$	Cumulative distribution function for the short-term extreme response \tilde{R} given the environmental parameters \mathbf{W}
$\nu(r \mathbf{w})$	Upcrossing rate of the response process r given the environmental parameters \mathbf{w}
$\sigma_R(\mathbf{w})$	Standard deviation of the response process R
$\sigma_{\dot{R}}(\mathbf{w})$	Standard deviation of the time derivative of the response process R

Long-Term Extreme Values

$F_{\tilde{R}_{LT}}(r)$	Cumulative distribution function for long-term extreme response
$F_{\tilde{R}_p}(r)$	Long-term cumulative distribution function of the response peak \tilde{R}_p
T	Long-term period
$\overline{\nu(0)}$	Long-term mean frequency of zero-upcrossings
$\nu(0 \mathbf{w})$	Zero-upcrossing rate given the environmental parameters \mathbf{w}
$f_{\mathbf{W}}(\mathbf{w})$	Joint probability density function over the environmental parameters \mathbf{w}
$F_{\tilde{R}_p \mathbf{W}}(r \mathbf{w})$	Cumulative distribution of peaks given short-term environmental parameters
$F_{\tilde{R}_p}(r)$	Approximate formulation for the cumulative distribution function over long-term peaks
\tilde{R}	Maximum response value during the short-term period \tilde{T}
\tilde{N}	Number of short-term periods considered for long-term extreme response analysis
$F_{\tilde{R}}(r)$	Exact long-term cumulative distribution function for the short-term extreme values
$\bar{F}_{\tilde{R}}(r)$	Approximate long-term cumulative distribution function for the short-term extreme values
$M(T)$	Maximum value of $X(t)$ during the long-term period T
$\overline{\nu_X(r)}$	Mean value of the upcrossing rate of level r for a long-term period
$\nu_X(r \mathbf{w})$	Mean upcrossing rate for an entire long-term period given the environmental parameters \mathbf{w}
q	Annual exceedance probability
r_q	Characteristic response value for a given exceedance probability q

Environmental Parameters

H_s	Stochastic variable representing the significant wave height
f_{H_s}	Probability density function for the significant wave height
α	Scale parameter of the Weibull distribution
β	Shape parameter of the Weibull distribution
γ	Location parameter of the Weibull distribution
F_{H_s}	Cumulative distribution function for the significant wave height
h	Stochastic realization of the significant wave height
T_z	Stochastic variable representing the zero-crossing period
$f_{T_z H_s}(t h)$	Probability density function for the wave zero-crossing period T_z given the significant wave height H_s
t	Stochastic realization of the zero-crossing period
$\mu(h)$	Lognormal distribution parameter
$\sigma(h)$	Lognormal distribution parameter
a_i	Coefficients for the lognormal distribution parameter μ
b_i	Coefficients for the lognormal distribution parameter σ
$F_{T_z H_s}(t h)$	Cumulative distribution function for the zero-crossing period given the significant wave height
$\text{erf}[\cdot]$	Error function

Stochastic Dynamic Behaviour of Sea Surfaces

ω	Wave angular frequency
$\kappa(\omega)$	Wave number as a function of angular wave frequency ω
d	Water depth
g	Gravitational constant
$\eta(x, y, t)$	Sea elevation process at position (x, y) and at time t

L	Wave length
θ	Wave angle relative to the considered structure
$S_{\eta}(\omega, \theta)$	Cross-spectral density as a function of wave frequency ω and wave angle θ
$D(\omega, \theta)$	Wave directional distribution as a function of the wave frequency ω and the wave angle θ relative to the considered structure
$D(\theta)$	Wave directional distribution as a function of the wave angle θ
s	Spreading parameter
$C(s)$	Normalizing constant as a function of the spreading parameter s
θ_0	Mean wave angle
$\Gamma(\cdot)$	Gamma function
$\Delta x, \Delta y$	Spatial distance in the x - and y -direction between two considered points
$S_{\eta_r \eta_s}$	Coherency between the wave height at point r and s
$S_{\eta}(\omega)$	Wave spectral density
A	Coefficient in the expression for the basic form of the Pierson-Moskowitz spectrum
B	Coefficient in the expression for the basic form of the Pierson-Moskowitz spectrum
α	Phillips constant used in the definition of the Pierson-Moskowitz spectrum
ω_p	Peak frequency at which the Pierson-Moskowitz spectrum attains its maximum value
γ	Peak enhancement factor used in the definition of the JONSWAP spectrum
$a(\omega)$	Exponential factor used in the definition of the JONSWAP spectrum
$\tilde{\sigma}$	Spectral width parameter used in the definition of the JONSWAP spectrum
$\tilde{\alpha}$	Factor used in the definition of the JONSWAP spectrum

Fluid - Structure Interaction

\mathbf{M}_s	Structural mass matrix
\mathbf{C}_s	Structural damping matrix
\mathbf{K}_s	Structural stiffness matrix
$\mathbf{u}(t)$	Displacement vector
$\dot{\mathbf{u}}(t)$	Velocity vector
$\ddot{\mathbf{u}}(t)$	Acceleration vector
\mathbf{p}_h	Total hydrodynamic action vector
\mathbf{m}_h	Hydrodynamic mass matrix
\mathbf{c}_h	Hydrodynamic damping matrix
\mathbf{K}_h	Hydrodynamic stiffness matrix
$\mathbf{p}(t)$	Wave excitation forces vector
$\mathbf{M}_h(\omega)$	Hydrodynamic mass matrix in the frequency domain
$\mathbf{C}_h(\omega)$	Hydrodynamic damping matrix in the frequency domain
$d\mathbf{Z}_u(\omega)$	Spectral process corresponding to the response vector
$d\mathbf{Z}_p(\omega)$	Spectral process corresponding to the wave excitation force vector
$\mathbf{M}(\omega)$	Frequency dependent total mass matrix
$\mathbf{C}(\omega)$	Frequency dependent total damping matrix
\mathbf{K}	Total stiffness matrix
$\mathbf{H}(\omega)$	Frequency response transfer function
$\mathbf{S}_u(\omega)$	Displacement response process spectral density
$\mathbf{S}_p(\omega)$	Wave action process spectral density
H	Hermitian operator (complex conjugate and matrix transpose)

$d\mathbf{Z}_h(\omega)$	Spectral process corresponding to the hydrodynamic forces acting on a submerged body
$d\mathbf{Z}_\eta(\omega, \theta)$	Spectral process corresponding to the sea surface elevation
\mathbf{S}_{prps}	Cross-spectral density matrix corresponding to the wave action process between the two points r and s
$\mathbf{Q}_r(\omega, \theta)$	Hydrodynamic directional wave excitation transfer function for a given element r
$\mathbf{Q}_s(\omega, \theta)$	Hydrodynamic directional wave excitation transfer function for a given element s

IFORM

R	Stochastic variable representing structural resistance
S	Stochastic variable representing external loads acting on a given structure
M	Stochastic variable representing the safety margin for a given structure under certain loading
β	Reliability index
$\text{Var}[\cdot]$	Variance operator
$g(\mathbf{X})$	Limit state function dependent on the random variables \mathbf{X} defining the failure surface
p_f	Probability of structural failure
$\Phi(\cdot)$	Standard normal cumulative distribution function
μ_M	Mean value of the safety margin M
σ_M	Standard deviation of the safety margin M
\mathbf{V}	Vector of stochastic variables in the physical space describing the environmental parameters \mathbf{W} and the response R
$f_{\mathbf{V}}(\mathbf{v})$	Joint probability density function over the environmental parameters and the response in the physical space

$f_{\tilde{R} \mathbf{W}}(\tilde{r} \mathbf{w})$	Probability density function for the response \tilde{R} given the environmental parameters \mathbf{W}
$G_r(\mathbf{v})$	Limit state function dependent on the parameters \mathbf{v} in the physical space
\mathbf{Y}	Stochastic response value
$F_{Y \mathbf{W}}(y \mathbf{w})$	Cumulative distribution function for the stochastic response variable \mathbf{Y} given the environmental parameters \mathbf{W}
$F_{\tilde{R} \mathbf{W}}(y \mathbf{w})$	Cumulative distribution function for the response \tilde{R} given the environmental parameters \mathbf{W}
$F_{Y \mathbf{W}}(r \mathbf{w})$	Cumulative distribution function for the response variable \mathbf{Y} given the environmental parameters \mathbf{W}
\mathbf{U}	Vector in the standard normal space
n	Number of random variables in the vector \mathbf{V}
F_{V_i}	Cumulative distribution function for the i -th random variable in the physical space
$f_U(\mathbf{u})$	Joint probability density function for the environmental parameters and response in U-space
v_{n+1}	Realization of the random variable \mathbf{V} in the physical space
β_r	Reliability index corresponding to the minimum distance between the origin and the limit state function in the IFORM-algorithm
\mathbf{u}^*	Design point in the FORM/IFORM-algorithm
M	Number of years in considered return period
r_M	Response value corresponding to a return period of M years
∇	Gradient operator
$ \cdot $	Vector length operator
α	Normal vector to the failure surface

$\nabla v_{n+1}(\mathbf{u}^*)$	Gradient of v_{n+1} evaluated at the design point \mathbf{u}^* as part of the IFORM-algorithm
c	Proportionality constant in the backtracking approach in the IFORM-algorithm
d	Directional derivative in the backtracking approach in the IFORM-algorithm
α_b	Step length in the backtracking approach in the IFORM-algorithm

Environmental Contour Method

$\hat{\mathbf{w}}$	Design point in the Environmental Contour Method representing the most unfavourable combination of the environmental parameters
p_q	Fractile value for the characteristic response r_q
$F_{\hat{R} \mathbf{W}}(r_q \hat{\mathbf{w}})$	Cumulative distribution function for the short-term extreme response at the design point $\hat{\mathbf{w}}$

Gaussian Process Regression

\mathbf{x}	Set of multivariate normal (Gaussian) distributed random variables
$\boldsymbol{\mu}$	Mean vector for multivariate Gaussian probability distribution
$\boldsymbol{\Sigma}$	Covariance matrix for multivariate Gaussian probability distribution
Λ	Precision matrix for multivariate Gaussian probability distribution
$p(x_i)$	Marginal Gaussian distribution over x_i
$p(x_i x_j)$	Posterior distribution for x_i given x_j
$\mu_{i j}$	Mean value of i given j
$\Sigma_{i j}$	Covariance of i given j
f_i	Known function value corresponding to known value x_i
$\boldsymbol{\mu}$	Mean value vector for function values in training set
\mathbf{K}	Covariance matrix for function values in training set
K_{ij}	Element of the covariance matrix given by relevant kernel function

x_*	Test point
f_*	Test function value corresponding to the test point x_*
N	Number of points in training set
N_*	Number of points in test set
D	Number of data sets
μ_*	Mean value of function values in test set
σ_*	Standard deviation of function values in test set
σ^2	Signal variance as a hyperparameter of the squared exponential kernel
l	Length scale as hyperparameter of the squared exponential kernel

Monte Carlo Simulation and Importance Sampling

N_M	Number of simulated samples
$h_{\mathbf{W}}(\mathbf{w})$	Importance density function

Modelling the Bergsøysund Bridge

A	Cross-sectional area of the Bergsøysund Bridge's superstructure
ρ	Mass density of the Bergsøysund Bridge's superstructure
I_y	Second moment of area about the local y-axis of the Bergsøysund Bridge's superstructure
I_{yz}	Product moment of area about y- and z-axis of the Bergsøysund Bridge's superstructure
I_z	Second moment of area about the local z-axis of the Bergsøysund Bridge's superstructure
I_T	St. Venants torsional constant of the Bergsøysund Bridge's superstructure
E	Elasticity modulus
G	Shear modulus
ν	Poisson's ratio

\mathbf{M}_0	Static mass matrix (inertia of pontoon)
\mathbf{K}_0	Restoring stiffness matrix
\mathbf{M}_h	Hydrodynamic mass matrix
\mathbf{C}_h	Hydrodynamic damping matrix
θ	Wave heading angle
ω	Frequency axis

Response Spectrum Calculation Structure

$\tilde{\mathbf{M}}^I$	Modal mass matrix for substructure I
$\tilde{\mathbf{K}}^I$	Modal stiffness matrix for substructure I
$\tilde{\mathbf{C}}^I$	Modal damping matrix for substructure I
α	Mass proportionality factor
β	Stiffness proportionality factor
$\mathbf{Q}_r(\omega, \theta)$	Hydrodynamic transfer function dependent on the frequency ω and the wave direction θ
$\mathbf{S}_p(\omega)$	Load spectral density matrix
$\mathbf{S}_u(\omega)$	Displacement spectral density matrix
\mathbf{M}^I	Mass matrix for substructure I
\mathbf{M}_s	Structural mass matrix
\mathbf{M}_{h0}	Hydrodynamic mass matrix
\mathbf{K}^I	Stiffness matrix for substructure I
\mathbf{K}_s	Structural stiffness matrix
\mathbf{K}_h	Hydrodynamic stiffness matrix
Φ^I	Mode vector for substructure I
ω_n^I	Natural frequency for substructure I

$\mathbf{M}_i^{II}(\omega)$	Frequency-dependent mass matrix for pontoon i
$\mathbf{M}_{h,i}(\omega)$	Frequency-dependent hydrodynamic mass matrix for pontoon i
\mathbf{C}_i^{II}	Frequency-dependent damping matrix for pontoon i
$\mathbf{C}_{h,i}(\omega)$	Frequency-dependent hydrodynamic damping matrix for pontoon i
\mathbf{K}_i^{II}	Stiffness matrix for pontoon i
$\mathbf{K}_{h,i}$	Hydrodynamic stiffness matrix for pontoon i
$\mathbf{M}^{II}(\omega)$	Global mass matrix for substructure II
$\mathbf{C}^{II}(\omega)$	Global damping matrix for substructure II
\mathbf{T}_i	Transformation matrix for pontoon i
$\tilde{\mathbf{M}}^{II}(\omega)$	Frequency-dependent modal mass matrix for substructure II
$\tilde{\mathbf{C}}^{II}(\omega)$	Frequency-dependent modal damping matrix for substructure II
$\tilde{\mathbf{M}}(\omega)$	Total mass matrix
$\tilde{\mathbf{C}}(\omega)$	Total damping matrix
$\tilde{\mathbf{K}}$	Total stiffness matrix
$S_\eta(\omega)$	Cross-spectral density as function of the wave frequency ω
$\mathbf{S}_{p_i p_j}(\omega)$	Load cross-spectral density matrix between pontoon i and j
$\tilde{\mathbf{S}}_p(\omega)$	Modal load spectral density matrix
$\tilde{\mathbf{H}}(\omega)$	Modal frequency response transfer function
$\tilde{\mathbf{S}}_u(\omega)$	Modal displacement spectral density matrix

Extreme Response Calculations

V_3	Physical response value in the IFORM-algorithm
\mathbf{u}	Point in standard normal space
\mathbf{v}	Vector of environmental parameters and response in the physical space
$h(\mathbf{u})$	Realization of significant wave height in the standard normal space
$t(\mathbf{u})$	Realization of zero-crossing period in the standard normal space
$v_3(\mathbf{u})$	Realization of response in the standard normal space
y	Short-term extreme response corresponding to an exact formulation
\tilde{r}	Short-term extreme response corresponding to an approximate formulation
\mathbf{u}_1	Initial point in the standard normal space for IFORM-algorithm
\mathbf{w}^*	Environmental parameters at the design point obtained using IFORM
\mathbf{w}_i^*	Environmental parameters at the design point obtained using IFORM for sample i in importance sampled Monte Carlo Simulation
μ_i	Mean value of sample i in importance sampled Monte Carlo Simulation
σ_i	Standard deviation of sample i in importance sampled Monte Carlo Simulation
N_s	Number of random states drawn from the environmental model
$d(x_i, x_j)$	The Euclidean distance between the points x_i and x_j
$\kappa_\nu(\cdot)$	Modified Bessel function
ν	Parameter of the Matérn kernel controlling the smoothness of the resulting function

Contents

Preface	I
Summary	II
Sammendrag	III
Abbreviations and Symbols	IV
List of Figures	XXII
List of Tables	XXIV
1 Introduction	1
1.1 Floating Bridges	2
1.2 Background	3
1.3 Previous Work	5
1.4 The Basis for the Thesis	5
1.5 The Scope of the Thesis	7
1.6 The Structure of the Thesis	7
2 Theory	9
2.1 Stochastic Loading and Random Vibrations	10
2.2 Fourier Transform and Frequency Analysis	11
2.3 Modal Analysis	12
2.4 The Frequency Response Method	13
2.5 Spectral Densities and Moments	16
2.6 Short-Term Extreme Values	18
2.6.1 Distribution of Peaks	18
2.6.2 Extreme Values	20
2.7 Long-Term Extreme Values	22
2.7.1 Short-Term Distribution of Peaks Model	22
2.7.2 Short-Term Extreme Values Model	23
2.7.3 Short-Term Upcrossing Rate Model	23

2.7.4	Characteristic Values of the Extreme Response	25
2.8	Environmental Parameters	25
2.8.1	Significant Wave Height	25
2.8.2	Zero-Crossing Period	26
2.9	Stochastic Dynamical Behaviour of Sea Surfaces	27
2.10	Fluid - Structure Interaction	30
2.11	IFORM	33
2.12	The Environmental Contour Method	39
2.13	Gaussian Process Regression	40
2.14	Crude Monte Carlo Simulation and Importance Sampling	44
3	Methodology	46
3.1	Modelling the Bergsøysund Bridge	47
3.1.1	The Bridge Superstructure	47
3.1.2	Pontoons	48
3.1.3	Full Bridge Model	52
3.2	Response Spectrum Calculation Structure	55
3.3	Software	58
3.3.1	The WAWI-Toolbox	58
3.3.2	Analytical third-party programs	59
3.4	Modal Analysis in Abaqus	60
3.4.1	Natural Frequencies and Modes	60
3.5	Extreme Response Calculations	63
3.5.1	Environmental Model Parameters	63
3.5.2	Full Integration	64
3.5.3	IFORM	65
3.5.4	Environmental Contour Method	66
3.5.5	IFORM and ISMCS	68
3.5.6	Gaussian Process Regression	69

4	Results	70
4.1	Long-Term Response Predictions	71
4.1.1	Full Integration	71
4.1.2	IFORM	76
4.1.3	Environmental Contour Method (ECM)	78
4.1.4	IFORM and ISMCS	81
4.1.5	Gaussian Process Regression (GPR)	84
5	Discussion	89
5.1	Bridge Model	90
5.2	Natural Frequencies and Modes	91
5.3	Discretization of Wave Angle and Frequency	91
5.4	Full Integration	92
5.5	IFORM	93
5.6	Comparing Full Integration, IFORM and ECM	93
5.7	IFORM and ISMCS	98
5.8	Gaussian Process Regression (GPR)	99
5.9	Modelling the Environmental Parameters	100
5.10	Magnitude of the Extreme Response	101
6	Conclusions	103
6.1	Conclusion	104
6.2	Proposal for Further Work	104
	Bibliography	106
	Appendices	110
	Appendix A	A1
	A.1 Dimensions of Mid-Span Pontoon	A1
	Appendix B	B1
	B.1 Iteration Points in U-space for Exact IFORM-Formulation	B1
	B.2 Iteration Points in U-space for Approximate IFORM-Formulation	B3
	Appendix C	C1
	C.1 CDF for the Long-Term Extreme Response from ECM	C1

List of Figures

1.1.1	Existing floating bridges in Norway	3
2.4.1	Argand diagrams for illustration of the frequency response function . . .	15
2.5.1	Relationship between area and spectral density curves	16
2.6.1	Illustration of the upcrossing rate $\nu_X(r)$	19
2.9.1	Pierson-Moskowitz, modified Pierson-Moskowitz and JONSWAP spectra	29
2.11.1	Definition of the reliability index β	34
2.11.2	FORM-algorithm illustrated	37
2.13.1	Data points for Gaussian Process Regression	41
2.13.2	Estimated function using Gaussian Process Regression	43
3.1.1	Wave angle definition	49
3.1.2	Pontoon model	50
3.1.3	Illustration of pontoon movements	51
3.1.4	Water depth profile and bridge overview	52
3.1.5	Top and side view of the bridge model	53
3.1.6	Side view of the bridge model at the mid-span	54
3.2.1	Flowchart for the calculation setup	57
3.4.1	Base state and mode shapes for the Abaqus model	62
3.5.1	Zeroth and second order moments for DOF 2 at pontoon 4	65
3.5.2	Iteration pattern for the M -year equivalent environmental parameters .	67
3.5.3	Joint PDF over the environmental parameters	68
4.1.1	CDF of exact long-term response for a return period of 10 years	71
4.1.2	CDF of exact long-term response for a return period of 100 years . . .	72
4.1.3	CDF of exact long-term response for a return period of 1000 years . . .	73
4.1.4	CDF of approximate long-term response for a return period of 10 years	74
4.1.5	CDF of approximate long-term response for a return period of 100 years	74
4.1.6	CDF of approximate long-term response for a return period of 1000 years	75
4.1.7	Response spectrum obtained with design points from exact IFORM . . .	77
4.1.8	Response spectrum obtained with design points from approximate IFORM	78
4.1.9	Response spectrum obtained with design points from ECM	79

4.1.10	CDF of long-term response from ECM for a return period of 10 years	80
4.1.11	CDF of long-term response from ECM for a return period of 100 years	80
4.1.12	CDF of long-term response from ECM for a return period of 1000 years	81
4.1.13	CDF from CMCS and ISMCS for a return period of 10 years	82
4.1.14	CDF from CMCS and ISMCS for a return period of 100 years	83
4.1.15	CDF from CMCS and ISMCS for a return period of 1000 years	83
4.1.16	Characteristic responses corresponding to training and test points in GPR	85
4.1.17	Variance of the predicted characteristic response values from GPR	87
4.1.18	Generated environmental parameters for training and test points in GPR	88
5.6.1	Location of design points in joint PDF for 10 year return period	95
5.6.2	Location of design points in joint PDF for 100 year return period	95
5.6.3	Location of design points in joint PDF for 1000 year return period	96
5.8.1	Effects of poor correlation between the environmental parameters	100
A.1.1	Geometrical dimensions for pontoon 4 from the Bergøysund Bridge	A1
B.1.1	Iteration points in U-space for 10-year exact IFORM	B1
B.1.2	Iteration points in U-space for 100-year exact IFORM	B1
B.1.3	Iteration points in U-space for 1000-year exact IFORM	B2
B.2.1	Iteration points in U-space for 10-year approximate IFORM	B3
B.2.2	Iteration points in U-space for 100-year approximate IFORM	B3
B.2.3	Iteration points in U-space for 1000-year approximate IFORM	B4
C.1.1	CDF from ECM for $p = 0.85$ and $M = 10$ years	C1
C.1.2	CDF from ECM for $p = 0.85$ and $M = 100$ years	C2
C.1.3	CDF from ECM for $p = 0.85$ and $M = 1000$ years	C2
C.1.4	CDF from ECM for $p = 0.90$ and $M = 10$ years	C3
C.1.5	CDF from ECM for $p = 0.90$ and $M = 100$ years	C3
C.1.6	CDF from ECM for $p = 0.90$ and $M = 1000$ years	C4
C.1.7	CDF from ECM for $p = 0.95$ and $M = 10$ years	C4
C.1.8	CDF from ECM for $p = 0.95$ and $M = 100$ years	C5
C.1.9	CDF from ECM for $p = 0.95$ and $M = 1000$ years	C5

List of Tables

3.1.1	Cross-sectional properties used for the bridge model	48
3.1.2	Material properties used in the bridge model	48
3.1.3	Discretization of the wave frequencies and angles	49
3.1.4	Output from the WADAM-analysis	50
3.4.1	Natural frequencies and periods from Abaqus	60
3.5.1	Distribution parameters used for the Weibull and lognormal distributions	64
3.5.2	Data used for the environmental parameters	64
3.5.3	Reliability indexes β_M corresponding to the different return periods M	66
3.5.4	M -year equivalent iterated environmental parameters	67
4.1.1	Response values from Full Integration based on the exact upcrossing model	73
4.1.2	Full Integration response values from short-term peaks and extreme values	75
4.1.3	Elapsed time for the Full Integration method	76
4.1.4	Results from IFORM for the exact formulation	76
4.1.5	Results from IFORM for the approximate formulation	76
4.1.6	Environmental parameters at the design points obtained from ECM . .	79
4.1.7	Characteristic long-term responses from ECM	81
4.1.8	Response values from CMCS and ISMCS	84
4.1.9	Characteristic response from the training points in GPR	85
4.1.10	Characteristic response from the predicted test points in GPR	86
4.1.11	Characteristic response from the evaluated test points in GPR	86
4.1.12	Generated environmental parameters for test and training points in GPR	88
5.4.1	Deviation in the results obtained from Full Integration	93
5.6.1	Deviation in response from IFORM and ECM compared to Full Integration	94
5.6.2	Design points from IFORM and ECM with probabilities of occurrence .	97
5.6.3	Run time for all the considered methods	97
5.6.4	Deviations between approximate IFORM and Full Integration	98
5.7.1	Deviations between exact IFORM-based MCS and Full Integration . .	99
5.10.1	Marginalized mean values of the environmental parameters	101
5.10.2	Extreme responses obtained for marginalized environmental parameters	101

CHAPTER 1

Introduction

1.1 Floating Bridges

Floating bridges are used all over the world for crossing fjords and other bodies of water. Although traditionally used for military and temporally emergency use, permanent civilian applications has become more prevalent throughout the recent decades. The purpose is then most often for highway traffic. While floating bridges are not the most common type among bridges, they can provide a feasible solution in situations where sailing heights are not a strict requirement and where land anchorage is not sufficient to support long-span suspension bridges. As of today, only two floating bridges exist in Norway. These are the Nordhordland Bridge and the Bergsøysund Bridge, depicted in Figure 1.1.1 (a) and (b), respectively.

The Nordhordland Bridge is a 1614 meter long combined floating- and cable-stayed bridge and is the second longest bridge in Norway (Monsrud, 2009). The floating part of the bridge make up 1246 meters of the total length. The bridge connects the island of Flatøy in the north with Hordvik in the south and is located north of the city of Bergen in the western part of Norway. Traffic runs on a continuous concrete slab supported by a total of 11 pontoons. The raised part of the bridge deck towards the cable-stayed segment is supported by steel and concrete columns. The Nordhordland Bridge has no horizontal mooring and is thereby the world's longest floating bridge without this kind of anchoring (Aas-Jacobsen, 2021).

The Bergsøysund Bridge is a 931 meter long floating bridge between Aspøya and Bergsøya in the north-western part of Norway. Following an arched curve with a radius of 1300 meters, the main structural system consists of a steel pipe truss with welded connections. Seven lightweight concrete pontoons in addition to the two end anchorages are used to support this structure. Each of these end anchorages consists of a bolted-in-place steel rod. Similar to the Nordhordland Bridge the Bergsøysund Bridge has no mooring making them the only two bridges of this kind in the world (Kvåle and Petersen, 2018).

The ability of floating bridges to achieve long spans is likely to be utilized in Norway in the near future. The ferry-free E39 project is to be conducted by the Norwegian Public Roads Administration along the western coast of Norway to ensure ferry-free transportation between the cities of Kristiansand and Trondheim. This project includes

several fjord-crossings where ferry transportation is to be replaced by bridges. The fjords in these areas are both deep and wide and several bridge solutions have therefore been proposed. Among these solutions are pontoon bridges and submerged tunnels. Some combinations of these are also considered. Common for all these alternatives is that structural dynamics will play a crucial role in their design.



(a) The Nordhordland Bridge (European Roads, 2014).



(b) The Bergsøysund Bridge (Kvåle, 2017).

Figure 1.1.1: Existing floating bridges in Norway.

1.2 Background

As the span of floating bridges increases, which will be the case in the ferry-free E39 project, efficient and accurate methods for computation of the long-term extreme response of such bridges will become ever more important. Traditional methods for this kind of long-term analyses such as numerical integration and Crude Monte Carlo Simulations can be very time-consuming and computationally expensive. For such long-term extreme

response calculations, a large number of short-term sea states are usually required. In order to make these analyses less computationally demanding, the necessary number of calculations will have to be reduced or these calculations should be performed more efficiently.

As of today, one of the most common methods used for estimation of the long-term extreme response of marine structures is the Environmental Contour Method (ECM). For a prescribed probability of exceedance, corresponding to a given return period, this method makes it possible to obtain reasonable long-term response estimates based on only a few short-term sea states (Naess and Moan, 2013). Assuming that the sea state can be completely described by the zero-crossing period and the significant wave height, the Environmental Contour Method will be based on the joint probability density function (PDF) of these two stochastic variables. This joint PDF is transformed into an independent standard normal space. In this space the contour lines will be circles with radiuses corresponding to given exceedance probabilities. Transforming the circles back into the physical space gives the isoprobability contour lines. The most unfavourable sea state along such a contour line is then identified. Finally, the long-term extreme response estimate is taken as a predetermined fractile value of the short-term response value corresponding to this identified sea state (Naess and Moan, 2013).

Another method which has gained some attention over the recent years is the Inverse First-Order Reliability Method (IFORM). This is a reliability-based iterative method which can be used to find the long-term extreme response of a structure given an annual exceedance probability. Depending on the number $n - 1$ of environmental conditions considered, this algorithm searches along a n -dimensional hypersphere to find a point giving the maximum response as well as the corresponding environmental conditions. The method is considered more effective than traditional methods for long-term extreme response calculations and its implementation and accuracy are described and investigated in more detail throughout this thesis.

1.3 Previous Work

Even though floating bridges similar to modern ones were in traffic as early as in the 1940s, the dynamical simulation and modelling of such bridges is first explored in detail in the late 1970s and early 1980s. These initial studies are conducted by research groups at the University of Washington in the United States led by Billy Hartz (Hartz and Mukherjee, 1977) and in Norway at NTNU and SINTEF led by Ivar Holand and Ivar Langen (Holand and Langen, 1972). Leon Emry Borgman systematized the methodology of time simulation of waves (Borgman, 1967), whereas Ivar Langen and Ragnar Sigbjörnsson exemplified the methodology for dynamical analysis of floating bridges with case studies of the Nordhordland Bridge, see Langen and Sigbjörnsson (1979) and Langen and Sigbjörnsson (1980).

In the context of long-term extreme response analysis of floating bridges, Arvid Naess and Torgeir Moan presented the methodology for the full long-term approach and the Crude Monte Carlo Simulation method in their book with the title *Stochastic Dynamics of Marine Structures* (Naess and Moan, 2013). In recent years, several algorithms for more efficient long-term extreme response calculations have been developed based on the observation that various environmental parameters contribute little or nothing to the overall response. Such algorithms include the already mentioned IFORM-approach presented by Sagrilo et al. (2011) where an Importance Sampled Monte Carlo Simulation approach based on this IFORM-method is also proposed. Introduced by Steven R. Winterstein and Sverre Haver in 1993 (Winterstein and Haver, 1993), the ECM-method is also considered a highly efficient method for response analysis of marine structures.

1.4 The Basis for the Thesis

Estimation of Long-Term Extreme Response of Floating Bridges is a broad topic with contributions from a wide range of fields. This thesis merges and further exemplifies the work of Finn-Idar Grøtta Giske (Giske, 2017) and Knut Andreas Kvåle (Kvåle et al., 2016) in an effort to compare various methods for performing long-term extreme response analysis on floating bridges.

Finn-Idar Grøtta Giske's doctoral thesis, *Long-Term Extreme Response Analysis of Marine Structures Using Inverse Reliability Methods*, presented a new method for efficient calculation of auto- and cross-spectral densities in the stochastic modelling of ocean waves and wave loads. A new method was also proposed for the numerical solution of the long-term extreme response of marine structures based on the IFORM-algorithm. The developments were demonstrated for a theoretical long-span pontoon bridge subjected to wave loads. The thesis concluded that the proposed new methods indeed were able to estimate the long-term extreme response accurately and in an efficient manner. The response appeared to only be slightly underestimated compared to the traditional full long-term calculations. However, the required number of short-term response calculations were greatly reduced.

Through his doctoral thesis with the title *Dynamic Behaviour of Floating Bridges Exposed to Wave Excitation*, Knut Andreas Kvåle presented accurate methods for the dynamical modelling of floating bridges. Measurements from the Bergsøysund Bridge were compared with numerical finite element model predictions. This work provided great insights into the dynamical characteristics of the Bergsøysund Bridge, as well as into the numerical modelling of floating bridges in general. Due to the low correlation between the wave excitation of each of the discrete pontoons, the wave spectral density matrix could be approximated as block-diagonal. It was concluded that this approximation had an insignificant effect on the resulting response spectral density matrix but provided higher efficiency in the use of such matrices for dynamical modelling.

The paper *Sequential Sampling Method Using Gaussian Process Regression for Estimating Extreme Structural Response* by Gramstad et al. (2019) presented a method for utilization of the machine learning technique known as Gaussian Process Regression (GPR) for estimation of the extreme response of marine structures. The method proposed in this paper used the GPR-approach to estimate the parameters of a short-term response probability distribution. The proposed method was demonstrated on the problem of estimating the long-term extreme bending moment on a theoretical ship structure. It was concluded that a relatively small number of iterations were needed to converge towards the "exact" results provided by more traditional full

long-term analyses. The method of Gaussian Process Regression provides an alternative to the already mentioned methods such as IFORM, MCS and ECM.

1.5 The Scope of the Thesis

This thesis aims to further investigate the efficiency and accuracy of a selection of numerical methods for estimation of the long-term extreme response of floating bridges. A simplified finite element model based on the geometry and structural properties of the Bergsøysund Bridge is generated. Based on this model a full long-term analysis is conducted as an estimate for the "exact" extreme response. The Environmental Contour Method, Inverse First-Order Reliability Method, Monte Carlo Simulation with Importance Sampling and Gaussian Process Regression are implemented based on the short-term outputs of the bridge model. The goal is to evaluate the accuracy and efficiency of each of these methods compared to the full long-term estimate obtained using the more traditional method of Full Integration.

A natural extension of the Inverse *First-Order* Reliability Method is the Inverse *Second-Order* Reliability Method. However, this method is not considered in this thesis due to the similarity between the two methods and the relatively low gain in considering a second order reliability problem over a first-order reliability problem. Furthermore, the emphasis in this thesis is laid on the more theoretical considerations regarding the employed methods rather than a very precise finite element model of the bridge. The strengths and limitations of each of these methods are considered to be of more scientific value than more comprehensive finite element modelling.

1.6 The Structure of the Thesis

The rest of this thesis is structured in the following way:

Chapter 2: Relevant theory for the thesis is presented. This includes an introduction to stochastic loading and random vibrations. The Fourier transform is presented as it is closely related to frequency domain analysis and spectral densities. Short- and long-term analyses are described before the theory is narrowed down to consider the environmental models used in the thesis as well as a description of the dynamical behaviour of sea

surfaces and fluid-structure interaction. Lastly, the numerical methods to be investigated are presented in detail.

Chapter 3: The methodology for the finite element modelling of the bridge is described in detail. Details regarding the bridge deck, pontoons and the global model is discussed. The procedure for the modelling and the relationship between the static and hydrodynamic model is presented followed by a description of the software used in the modelling. The implementation of each of the methods for the long-term extreme response analysis to be conducted is also described.

Chapter 4: The results of the investigation are presented. Important limitations and assumptions for the methods and their implementations are highlighted and justified.

Chapter 5: The results presented in Chapter 4 are evaluated and discussed. Possible deviations from the expected results are discussed and the methods used are reviewed.

Chapter 6: Conclusions are drawn based on the discussions in Chapter 5. Proposals for further work on the topic are given.

CHAPTER 2

Theory

This chapter is devoted to the theoretical background for the phenomena and methods used throughout the project. The sections serve as a foundation for the choices and assumptions made in the implementation of these methods. First, a basic introduction to stochastic loading and random vibrations is given. Next, the Fourier transform is introduced in the context of the frequency response method and spectral densities. These general concepts are then employed in the description of short- and long-term extreme response analysis. The stochastic dynamic behaviour of sea surfaces, fluid-structure interaction, numerical methods, and Gaussian Process Regression are also described.

2.1 Stochastic Loading and Random Vibrations

In general, environmental loads acting on structures are rather unpredictable. It is in general not possible to measure two identical time series of the same load effect. For this reason, the loading on a structure will have to be described in terms of its statistical properties rather than by actual realizations of the load itself. Furthermore, in order to describe the response of a structure subjected to random loading the relationship between the statistical properties of this loading and the response of the structure has to be established.

As a measure of similarity between stochastic processes the auto- and cross-correlation functions are often used. For a given load or response realization x_1 measured over two separate time series t_1 and t_2 the auto-correlation function is defined as (Newland, 2012):

$$R_{x_1}(t_1, t_2) = \mathbb{E}[x_1(t_1) \cdot x_1(t_2)] \quad (2.1.1)$$

Here $\mathbb{E}[\cdot]$ denotes the expected value operator. It is important to note that the definition given in Equation (2.1.1) is valid only for stationary processes. A stationary process is a random process in which its statistical properties do not change over time. Furthermore, a homogeneous process is a stochastic process which is stationary in space (Newland, 2012). An important property of the auto-correlation function for a homogeneous stationary process is that it is only dependent on the time lag τ between the two considered time series t_1 and t_2 and not directly on these time series themselves. Using this information Equation (2.1.1) can be written as:

$$R_{x_1}(\tau) = \mathbb{E}[x_1(t) \cdot x_1(t + \tau)] \quad (2.1.2)$$

A concept related to the auto-correlation function is the cross-correlation function. The cross-correlation between two different stochastic realizations x_1 and x_2 with mutual time lag τ considered over a time period t is defined as:

$$R_{x_1x_2}(\tau) = \mathbb{E}[x_1(t) \cdot x_2(t + \tau)] \quad (2.1.3)$$

As can be seen when comparing Equation (2.1.2) and (2.1.3) the difference is that the

auto-correlation quantifies the self-correlation of a single stochastic process, whereas the cross-correlation gives information about the correlation between two separate stochastic processes.

2.2 Fourier Transform and Frequency Analysis

In addition to the pure statistical properties of the loading and the response, the frequency content is also of much importance for dynamical systems. In the transition from stochastic loading to stochastic response several frequency-dependent quantities are present. These quantities can complicate the differential equations governing the dynamical system when considered in the time domain. For this reason, it can be useful to transform the considered process from the time domain over to the frequency domain where the problem can be solved using algebraic equations. The transformation of a stochastic process $x(t)$ in the time domain to a process in the frequency domain $x(\omega)$ can be achieved through the use of the complex Fourier transform which is defined as:

$$x(\omega) = \frac{1}{2\pi} \int_{-\infty}^{\infty} x(t) e^{-i\omega t} dt \quad (2.2.1)$$

In Equation (2.2.1) the letter i denotes the imaginary unit. In the frequency domain the frequency-dependent algebraic equations are solved. The resulting stochastic process is then transformed back into the time domain by use of the inverse complex Fourier transform defined as:

$$x(t) = \int_{-\infty}^{\infty} x(\omega) e^{i\omega t} d\omega \quad (2.2.2)$$

The use of the factor $1/2\pi$ for the Fourier transform in Equation (2.2.1) represents the most common formulation for the Fourier transform used in the theory of random vibrations (Newland, 2012). However, the position of this factor tends to vary between different fields of study. The factor may for example be incorporated in the expression for the inverse Fourier transform. The fact that these formulations often vary may also be reflected in this thesis.

Lastly, it should be noted that the Fourier transform only exists for stochastic processes $x(t)$ which decay to zero when the length of the considered time period approaches infinity.

This condition can be expressed as (Newland, 2012):

$$\int_{-\infty}^{\infty} |x(t)| dt < \infty \quad (2.2.3)$$

2.3 Modal Analysis

The equation of motion for a linear undamped dynamical system with mass matrix \mathbf{M} and stiffness matrix \mathbf{K} can be written as (Williams, 2016):

$$\mathbf{M}\ddot{\mathbf{u}} + \mathbf{K}\mathbf{u} = \mathbf{0} \quad (2.3.1)$$

Here $\ddot{\mathbf{u}}$ and \mathbf{u} denotes the acceleration and displacement vector, respectively. The displacement \mathbf{u} , which is a function of both time and position, can be expressed as the product of the space dependent amplitude \mathbf{u}_0 and a sine factor dependent on both the time t and the frequency ω (Williams, 2016), yielding:

$$\mathbf{u} = \mathbf{u}_0 \sin(\omega t) \quad (2.3.2)$$

Differentiating this expression for \mathbf{u} and introducing it into Equation (2.3.1) results in the following characteristic equation for the dynamical system:

$$(\mathbf{K} - \omega^2 \mathbf{M}) \mathbf{u}_0 \sin(\omega t) = \mathbf{0} \quad (2.3.3)$$

From Equation (2.3.3) it can be observed that for the equation to be satisfied it is sufficient that either \mathbf{u}_0 or $\sin(\omega t)$ is equal to zero, resulting in no vibration. Another option is multiplying the equation by the inverse of $(\mathbf{K} - \omega^2 \mathbf{M})$. However, this part of the equation has no inverse, requiring its determinant to be zero to satisfy the equation. From this the following eigenvalue problem can be established:

$$\det(\mathbf{K} - \omega^2 \mathbf{M}) = 0 \quad (2.3.4)$$

The eigenvalue problem in Equation (2.3.4) can be solved for the natural frequencies ω . For a given system with n DOFs this will result in n natural frequencies. Each such

natural frequency ω_i , where $i = 1, 2, \dots, n$, can then be introduced into Equation (2.3.5) in order to find its corresponding eigenvector $\mathbf{u}_{0,i}$. These eigenvectors $\mathbf{u}_{0,i}$ also represent the mode shapes of the system.

$$(\mathbf{K} - \omega^2 \mathbf{M}) \mathbf{u}_0 = \mathbf{0} \quad (2.3.5)$$

The mode shape vector \mathbf{u}_0 represents the amplitude of the displacement along the considered structure given a particular natural vibration frequency. This amplitude varies with time, but the ratio between the magnitudes of the displacement at the various DOFs stays the same. It should be noted that the overall amplitude of the vibration is dependent on both the boundary conditions of the system as well as on the external loading (Williams, 2016).

For convenience, a mode shape vector can be mass normalized:

$$\phi_i^T \mathbf{M} \phi_i = 1 \quad (2.3.6)$$

Here ϕ_i denotes the mass normalized mode shape vector which can be expressed as:

$$\phi_i = \alpha \mathbf{u}_{0,i} \quad (2.3.7)$$

α is referred to as the mass normalization scaling factor and can be calculated by inserting Equation (2.3.6) into (2.3.7), yielding:

$$\alpha = \frac{1}{\sqrt{\mathbf{u}_{0,i}^T \mathbf{M} \mathbf{u}_{0,i}}} \quad (2.3.8)$$

2.4 The Frequency Response Method

For a more general structure subjected to a load $\mathbf{p}(t)$ the equation of motion is written as:

$$\mathbf{M}\ddot{\mathbf{u}}(t) + \mathbf{C}\dot{\mathbf{u}}(t) + \mathbf{K}\mathbf{u}(t) = \mathbf{p}(t) \quad (2.4.1)$$

As before \mathbf{M} , \mathbf{C} and \mathbf{K} represent the mass, damping and stiffness matrices, while $\ddot{\mathbf{u}}(t)$, $\dot{\mathbf{u}}(t)$ and $\mathbf{u}(t)$ represent the acceleration, velocity and displacement of the structure,

respectively.

The harmonic load of unit amplitude can be assumed to be on the form:

$$\mathbf{p}(t) = e^{i\omega t} \quad (2.4.2)$$

Here i , ω and t denote the imaginary unit, the load frequency, and the time variable, respectively. The equation of motion now takes the form:

$$\mathbf{M}\ddot{\mathbf{u}}(t) + \mathbf{C}\dot{\mathbf{u}}(t) + \mathbf{K}\mathbf{u}(t) = e^{i\omega t} \quad (2.4.3)$$

Furthermore, a new assumption is made. This time regarding the dynamical response of the structure. The particular solution of Equation (2.4.3), or the steady-state response of the structure, is expected to take the following form:

$$\mathbf{u} = \mathbf{H}(\omega)e^{i\omega t} \quad (2.4.4)$$

Inserting this assumed solution into the equation of motion from Equation (2.4.3) and solving for $\mathbf{H}(\omega)$ results in the following expression:

$$\mathbf{H}(\omega) = \frac{1}{\mathbf{K} - \omega^2\mathbf{M} + i\omega\mathbf{C}} \quad (2.4.5)$$

Here it may be useful to introduce the relations of the squared natural frequency ω_n^2 , the damping ratio ξ and the frequency ratio β (Newland, 2012):

$$\omega_n^2 = \frac{\mathbf{K}}{\mathbf{M}} \quad (2.4.6a)$$

$$\xi = \frac{\mathbf{C}}{2\mathbf{M}\omega_n} \quad (2.4.6b)$$

$$\beta = \frac{\omega}{\omega_n} \quad (2.4.6c)$$

Introducing these relations into the expression for $\mathbf{H}(\omega)$ results in the following expression:

$$\mathbf{H}(\omega) = \frac{1}{\mathbf{K}(1 - \beta^2 + 2\xi\beta i)} \quad (2.4.7)$$

In order to cancel out the imaginary part in the denominator in this expression, both the

denominator and the numerator are multiplied by its complex conjugate. Now introducing the resulting expression for $\mathbf{H}(\omega)$ into the assumed steady-state response solution gives:

$$\mathbf{u} = \underbrace{\frac{1}{\mathbf{K} ((1 - \beta^2)^2 + (2\xi\beta))}}_{\mathbf{H}(\omega)} ((1 - \beta^2) - 2\xi\beta i) e^{i\omega t} \quad (2.4.8)$$

Here the expression for $\mathbf{H}(\omega)$ is highlighted. This function is referred to as the (complex) frequency response function. This is a single complex function used to represent both the amplitude ratio y_0/x_0 and the phase angle θ . The former is defined as the ratio between the amplitude of the response (y_0) and the loading (x_0), whereas the latter represents the relative motion of the loading and the response (Newland, 2012). The frequency response function is defined such that its magnitude is equal to the amplitude ratio and the ratio between its imaginary and real part corresponds to the tangent of the phase angle (Newland, 2012). This can be illustrated using an Argand diagram. In Figure 2.4.1 such a diagram is showed for both $t = 0$ and $t \neq 0$:

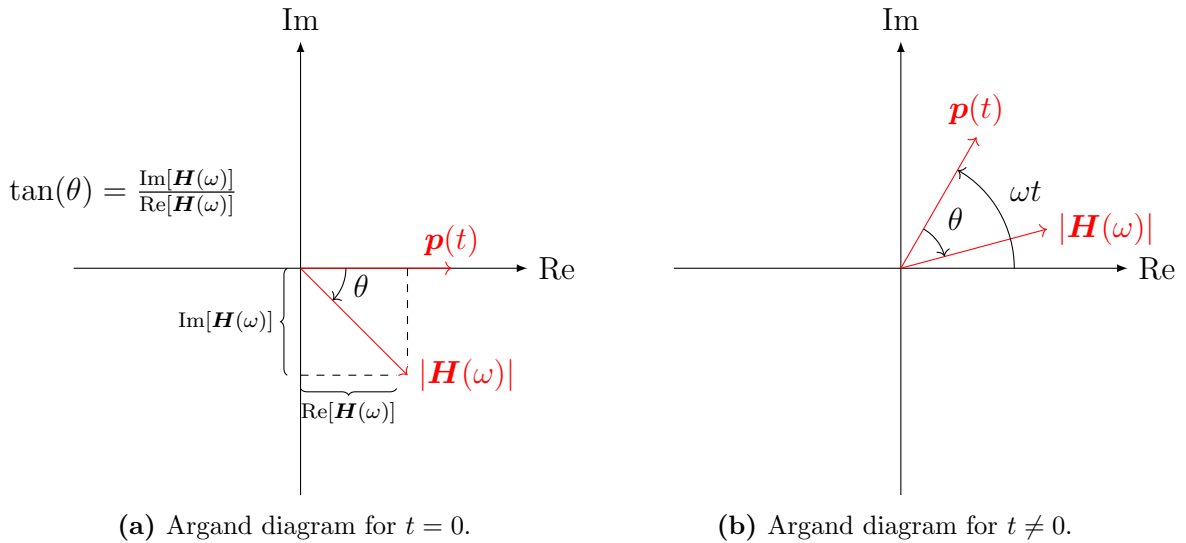


Figure 2.4.1: Argand diagrams for illustration of the frequency response function $\mathbf{H}(\omega)$.

2.5 Spectral Densities and Moments

As mentioned in Section 2.2 the auto- and cross-correlation functions give information about the frequency content of the stochastic loading and response when considered in the frequency domain. However, a given realization $x(t)$ of a stochastic process is in general not periodic and does not satisfy the condition in Equation (2.2.3). Thus, the Fourier transform will not exist for such a realization. This problem can be overcome by analysing the Fourier transform of the auto- and cross-correlation functions of the process $x(t)$, rather than of the actual process itself.

Assuming that the stochastic process has zero mean and no periodic components, the auto- and cross-spectral densities are defined as the Fourier transform of the auto- and cross-correlation functions, respectively:

$$S_{x_1}(\omega) = \frac{1}{2\pi} \int_{-\infty}^{\infty} R_{x_1}(\tau) e^{-i\omega\tau} d\tau \quad (2.5.1a)$$

$$S_{x_1x_2}(\omega) = \frac{1}{2\pi} \int_{-\infty}^{\infty} R_{x_1x_2}(\tau) e^{-i\omega\tau} d\tau \quad (2.5.1b)$$

The area under the auto-spectral density curve corresponds to the mean square value of the stationary random process x_1 . Likewise, the area under the real part of the complex cross-spectral density curve corresponds to the covariance of two separate stationary random processes x_1 and x_2 (Newland, 2012). This is illustrated in Figure 2.5.1 (a) and (b).

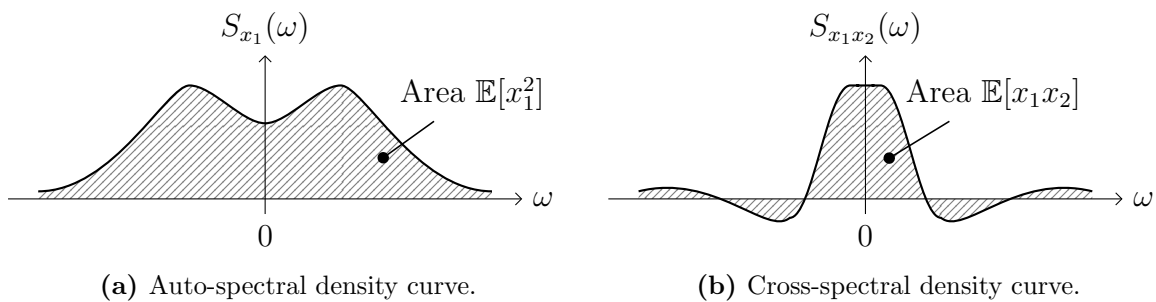


Figure 2.5.1: Relationship between area and spectral density curves (Newland, 2012).

The auto- and cross-spectral densities make up what is called a Fourier transform pair with the auto- and cross-correlation functions. Thus, the inverse Fourier transform of the auto- and cross-spectral densities corresponds to the auto- and cross-correlation functions,

respectively:

$$R_{x_1}(\tau) = \int_{-\infty}^{\infty} S_{x_1}(\omega) e^{i\omega\tau} d\omega \quad (2.5.2a)$$

$$R_{x_1x_2}(\tau) = \int_{-\infty}^{\infty} S_{x_1x_2}(\omega) e^{i\omega\tau} d\omega \quad (2.5.2b)$$

Since the term $e^{i\omega\tau}$ in Equation (2.5.2a) is real and even-valued, the expression for $R_{x_1}(\tau)$ can be rewritten as:

$$R_{x_1}(\tau) = \int_{-\infty}^{\infty} S_{x_1}(\omega) \cos(\omega\tau) d\omega \quad (2.5.3)$$

The expression in Equation (2.5.3) can be considered a moment generating function (Sweitzer et al., 2004). By differentiating the expression for $R_{x_1}(\tau)$ several times with respect to τ the following is obtained:

$$\frac{d}{d\tau} R_{x_1}(\tau) = \frac{d}{dt} R_{x_1}(\tau) = - \int_{-\infty}^{\infty} \omega S_{x_1}(\omega) \sin(\omega\tau) d\omega \quad (2.5.4a)$$

$$\frac{d^2}{d\tau^2} R_{x_1}(\tau) = - \frac{d^2}{dt^2} R_{x_1}(\tau) = - \int_{-\infty}^{\infty} \omega^2 S_{x_1}(\omega) \cos(\omega\tau) d\omega \quad (2.5.4b)$$

$$\frac{d^3}{d\tau^3} R_{x_1}(\tau) = - \frac{d^3}{dt^3} R_{x_1}(\tau) = \int_{-\infty}^{\infty} \omega^3 S_{x_1}(\omega) \sin(\omega\tau) d\omega \quad (2.5.4c)$$

$$\frac{d^4}{d\tau^4} R_{x_1}(\tau) = \frac{d^4}{dt^4} R_{x_1}(\tau) = \int_{-\infty}^{\infty} \omega^4 S_{x_1}(\omega) \cos(\omega\tau) d\omega \quad (2.5.4d)$$

$$\vdots \quad \quad \quad \vdots$$

Following the pattern in Equation (2.5.4a) through (2.5.4d) the following general definition for the moments μ_n can be established when setting $\tau = 0$:

$$\mu_n = \frac{d^n}{d\tau^n} R_{x_1}(0) = \frac{d^n}{dt^n} R_{x_1}(0) = \int_{-\infty}^{\infty} \omega^n S_{x_1}(\omega) d\omega \quad (2.5.5)$$

The moments μ_n define how each of the processes $x_1(t), \dot{x}_1(t), \ddot{x}_1(t), \dots, x_1^{(n)}(t)$ are related to each other. μ_n denotes the moments for the two-sided spectra, i.e. the spectra integrated from $-\infty$ to ∞ . The one-sided moments m_n , i.e. for the spectra integrated from 0 to ∞ , can be found as:

$$\mu_n = \int_0^{\infty} \omega^n 2 S_{x_1}(\omega) d\omega = \int_0^{\infty} \omega^n G_{x_1}(\omega) d\omega = m_n \quad (2.5.6)$$

where:

$$G_{x_1} = 2 S_{x_1} \quad (2.5.7)$$

This implies that:

$$m_n = \int_0^\infty \omega^n G_{x_1}(\omega) d\omega \quad (2.5.8)$$

Here m_n denotes the one-sided n-th order moment of the stochastic variable x_1 . Setting $n = 0$ yields the variance of a zero mean spectral density. Typically, the moments m_1 , m_2 and m_4 are also calculated (Sweitzer et al., 2004).

2.6 Short-Term Extreme Values

The theory on stationary stochastic processes is essential in the design of marine structures. For floating bridges, the environmental loads can be modelled as stationary stochastic processes over a limited time period, referred to as a short-term period. The duration of such a short-term period, denoted \tilde{T} , is often chosen as three hours for offshore structures subjected to wave loading (Naess and Moan, 2013). Assuming such short-term conditions the short-term response of the structure can be calculated using various statistical and dynamical methods. Such methods are outlined in the following sections.

2.6.1 Distribution of Peaks

In the design of structures the stochastic distribution of peak values for an arbitrary realization of the response process $X(t)$ is of much interest (Naess and Moan, 2013). A related measure in this regard is the upcrossing rate $\nu_X(r)$. This is a probabilistic measure of the number of times the response value exceeds a given amplitude value r per unit time and is given by Rice's formula (Øiseth, 2020):

$$\nu_X(r) = \int_0^\infty \dot{x} f_{X\dot{X}}(r, \dot{x}) d\dot{x} \quad (2.6.1)$$

Here \dot{x} and $f_{X\dot{X}}(r, \dot{x})$ denote the time derivative of the response realization x and the joint probability density function of this response process and its time derivative, respectively. The integrand in Equation (2.6.1) can be interpreted as the probability that the response

reaches the level r with a positive time derivative during a given time period. A special case of the upcrossing rate is the zero-upcrossing rate $\nu_X(0)$, which is found for $r = 0$. An illustration of the upcrossing rate $\nu_X(r)$ for a given level r is found in Figure 2.6.1:

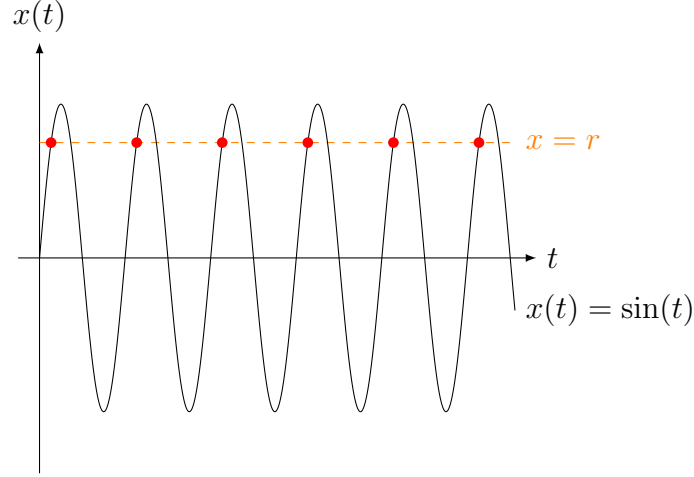


Figure 2.6.1: Illustration of the upcrossing rate $\nu_X(r)$. Each red dot represents an upcrossing of level r .

Assuming that the process is stationary, the average number of upcrossings N_X is proportional to the considered time period T :

$$N_X(T) = \nu_X(r)T \quad (2.6.2)$$

The idealized stochastic response process in Figure 2.6.1 is narrow-banded. This means that only a very limited range of frequencies are dominating. For such processes, the number of zero-crossings will be approximately equal to the number of peaks. Defining the random variable X_p as the peaks of the stochastic process $X(t)$, the probability of exceeding the level r is given by (Øiseth, 2020):

$$Prob\{X_p > r\} = \frac{\nu_X(r)}{\nu_X(0)} \quad (2.6.3)$$

Following the argumentation above, this is the same as dividing the number of upcrossings of level r by the total number of peaks. The cumulative distribution function and the probability density function of the peaks can now be expressed as:

$$Prob\{X_p < r\} = F_{X_p}(r) = 1 - \frac{\nu_X(r)}{\nu_X(0)} \quad (2.6.4a)$$

$$f_{X_p}(r) = -\frac{1}{\nu_X(0)} \frac{d\nu_X(r)}{dr} \quad (2.6.4b)$$

A stochastic variable and its time derivative are assumed independent for Gaussian probability distributions. Thus, assuming that the stochastic process $X(t)$ is Gaussian gives the following expression for the joint probability distribution of these two stochastic variables:

$$f_{X\dot{X}}(x, \dot{x}) = f_X(x)f_{\dot{X}}(\dot{x}) = \frac{1}{2\pi\sigma_X\sigma_{\dot{X}}} \exp \left\{ -\frac{1}{2} \left[\left(\frac{x - m_X}{\sigma_X} \right)^2 + \left(\frac{\dot{x}}{\sigma_{\dot{X}}} \right)^2 \right] \right\} \quad (2.6.5)$$

Here m_X and σ_X denote the mean value and standard deviation of the stochastic process $X(t)$, respectively. Likewise, $m_{\dot{X}}$ and $\sigma_{\dot{X}}$ denote the mean value and standard deviation of the stochastic process $\dot{X}(t)$. Introducing the expression for $f_{X\dot{X}}(x, \dot{x})$ into the integral in Equation (2.6.1) yields the following expression for the upcrossing rate:

$$\nu_X(r) = \frac{1}{2\pi} \frac{\sigma_{\dot{X}}}{\sigma_X} \exp \left\{ -\frac{1}{2} \left(\frac{r - m_X}{\sigma_X} \right)^2 \right\} \quad (2.6.6)$$

Assuming zero mean, $m_X = 0$, gives:

$$\nu_X(r) = \frac{1}{2\pi} \frac{\sigma_{\dot{X}}}{\sigma_X} \exp \left\{ -\frac{1}{2} \left(\frac{r}{\sigma_X} \right)^2 \right\} \quad (2.6.7)$$

Introducing this expression into Equation (2.6.4b) gives the following probability density function for the distribution of the peaks:

$$f_{X_p}(r) = \frac{r}{\sigma_X^2} \exp \left\{ \frac{1}{2} \left(\frac{r}{\sigma_X} \right)^2 \right\} \quad (2.6.8)$$

The expression in Equation (2.6.8) is known as the Rayleigh distribution of peaks (Øiseth, 2020).

2.6.2 Extreme Values

The largest value that the stochastic process $X(t)$ assumes during a short-term period \tilde{T} can be denoted $M(\tilde{T})$. If peaks exceeding the level r are assumed to be independent events, the random number of upcrossings during such a short-term period can be described by a Poisson distribution with the following cumulative distribution function

(Øiseth, 2020):

$$Prob \left\{ M(\tilde{T}) \leq r \right\} = F_{\tilde{R}}(r) = \exp \left\{ -\nu_X(r)\tilde{T} \right\} \quad (2.6.9)$$

The loading on a given structure is generally caused by a wide range of environmental conditions. Such conditions, or parameters, typically include the mean wind velocity for suspension bridges or wave height and wave direction for floating bridges. Other environmental parameters are also often relevant, as well as certain combinations of these. Various environmental models and parameters are described in more detail in Section 2.8. Nevertheless, assuming that the upcrossing rate is dependent on such environmental parameters, denoted \mathbf{W} , Equation (2.6.9) can be rewritten as the following conditional cumulative distribution function of the short-term extreme response, $F_{\tilde{R}|\mathbf{W}}$ (Giske, 2017):

$$F_{\tilde{R}|\mathbf{W}}(r|\mathbf{w}) = \exp \left\{ -\nu(r|\mathbf{w})\tilde{T} \right\} \quad (2.6.10)$$

Here $\nu(r|\mathbf{w})$ denotes the upcrossing rate at the response level r given the environmental parameters \mathbf{w} . The expression for this conditional upcrossing rate can be written as:

$$\nu(r|\mathbf{w}) = \frac{1}{2\pi} \frac{\sigma_{\dot{R}}(\mathbf{w})}{\sigma_R(\mathbf{w})} \exp \left\{ -\frac{1}{2} \left(\frac{r}{\sigma_R(\mathbf{w})} \right)^2 \right\} \quad (2.6.11)$$

Here σ_R and $\sigma_{\dot{R}}$ denote the standard deviation of the response process R and its time derivative, respectively. Introducing the expression in Equation (2.6.11) into Equation (2.6.10) yields the following expression for the cumulative distribution function for the short-term extreme response given the environmental parameters \mathbf{w} :

$$F_{\tilde{R}|\mathbf{W}}(r|\mathbf{w}) = \exp \left\{ -\frac{\tilde{T}}{2\pi} \frac{\sigma_{\dot{R}}(\mathbf{w})}{\sigma_R(\mathbf{w})} \exp \left\{ -\frac{1}{2} \left(\frac{r}{\sigma_R(\mathbf{w})} \right)^2 \right\} \right\} \quad (2.6.12)$$

Here, the relations between $\sigma_R(\mathbf{w})$ and $\sigma_{\dot{R}}(\mathbf{w})$ and the spectral moments defined in Equation (2.5.8) are as follows:

- $\sigma_R(\mathbf{w}) = \sqrt{m_0}$
- $\sigma_{\dot{R}}(\mathbf{w}) = \sqrt{m_2}$

2.7 Long-Term Extreme Values

In this section the short-term formulations in the previous section are slightly adjusted to account for long-term conditions. Additionally, a long-term formulation based on the short-term upcrossing rate is introduced.

2.7.1 Short-Term Distribution of Peaks Model

Under the assumption that all short-term response peaks are independent events, the cumulative distribution function for the long-term extreme response is given by (Giske, 2017):

$$F_{\tilde{R}_{LT}}(r) = F_{\tilde{R}_p}(r)^{\overline{\nu(0)}T} \quad (2.7.1)$$

Here $F_{\tilde{R}_p}(r)$ denotes the long-term cumulative distribution function of a response peak \tilde{R}_p , T is the long-term period while $\overline{\nu(0)}$ represents the long-term mean frequency of zero-upcrossings. The latter is defined as the integral of the zero-upcrossing rate given the environmental parameters \mathbf{w} weighted by the joint probability density function over these same parameters:

$$\overline{\nu(0)} = \int_{\mathbf{w}} \nu(0|\mathbf{w})f_{\mathbf{W}}(\mathbf{w}) d\mathbf{w} \quad (2.7.2)$$

Based on $\overline{\nu(0)}$, the expected number of response peaks during the long-term period T is found as the product $\overline{\nu(0)}T$. Furthermore, an approximate formulation for the cumulative distribution function over the long-term peaks can be obtained. This formulation is based on the distribution of peaks given short-term environmental conditions, $F_{\tilde{R}_p|\mathbf{W}}(r|\mathbf{w})$, and is expressed as (Giske, 2017):

$$F_{\tilde{R}_p}(r) \approx \int_{\mathbf{w}} F_{\tilde{R}_p|\mathbf{W}}(r|\mathbf{w})f_{\mathbf{W}}(\mathbf{w}) d\mathbf{w} \quad (2.7.3)$$

In Equation (2.7.3) it is assumed that the number of response peaks is the same for all environmental parameters, which is generally not the case. To overcome this limitation the integrand in Equation (2.7.3) is scaled by a factor representing the average zero-upcrossing rate (Battjes, 1972):

$$F_{\tilde{R}_p}(r) = \int_{\mathbf{w}} \frac{\nu(0|\mathbf{w})}{\overline{\nu(0)}} F_{\tilde{R}_p|\mathbf{W}}(r|\mathbf{w})f_{\mathbf{W}}(\mathbf{w}) d\mathbf{w} \quad (2.7.4)$$

2.7.2 Short-Term Extreme Values Model

The maximum response value during the short-term period \tilde{T} is denoted \tilde{R} . Assuming that the extreme values of these short-term periods are independent events, the cumulative distribution function for the long-term extreme values, $F_{\tilde{R}_{LT}}(r)$, is obtained as the product of \tilde{N} long-term cumulative distributions of short-term extreme values, $F_{\tilde{R}}(r)$ (Sagrilo et al., 2011):

$$F_{\tilde{R}_{LT}}(r) = F_{\tilde{R}}(r)^{\tilde{N}} \quad (2.7.5)$$

If the cumulative distribution function for the largest response peak given the environmental parameters \mathbf{w} is denoted $F_{\tilde{R}|\mathbf{W}}(r|\mathbf{w})$, then the exact long-term cumulative distribution function for the short-term extreme values is found as (Sagrilo et al., 2011):

$$F_{\tilde{R}}(r) = \exp \left\{ \int_{\mathbf{w}} \ln \left(F_{\tilde{R}|\mathbf{W}}(r|\mathbf{w}) \right) f_{\mathbf{W}}(\mathbf{w}) d\mathbf{w} \right\} \quad (2.7.6)$$

The formulation in Equation (2.7.6) is obtained using ergodic averaging. This means that the mean value of a specific sample in the ensemble (a collection of samples from the same stochastic process) coincides with the mean value for the whole ensemble. However, using the population mean instead of the ergodic average yields the following approximate formulation $\bar{F}_{\tilde{R}}(r)$ (Naess and Moan, 2013):

$$\bar{F}_{\tilde{R}}(r) = \int_{\mathbf{w}} F_{\tilde{R}|\mathbf{W}}(r|\mathbf{w}) f_{\mathbf{W}}(\mathbf{w}) d\mathbf{w} \quad (2.7.7)$$

Compared to the formulation in Equation (2.7.6), the formulation in Equation (2.7.7) can be solved more efficiently as part of a reliability formulation. This is described in greater detail in Section 2.11.

2.7.3 Short-Term Upcrossing Rate Model

When considering the long-term extreme values of the stochastic process $X(t)$ the process can no longer be considered stationary. This is because the mean value and standard deviation of the process will vary as the various environmental parameters vary (Øiseth, 2020). For this reason, Equation (2.6.9) will have to be generalized in order to be valid

for the long-term conditions. This is achieved through the following reformulation:

$$Prob\{M(T) \leq r\} = F_{\tilde{R}_{LT}}(r) = \exp\left\{-\overline{\nu_X(r)}T\right\} \quad (2.7.8)$$

In Equation (2.7.8) the short-term upcrossing rate $\nu_X(r)$ is replaced by its mean value for the entire long-term period, $\overline{\nu_X(r)}$. This mean value is given as:

$$\overline{\nu_X(r)} = \frac{1}{T} \int_0^T \nu_X(r, t) dt \quad (2.7.9)$$

The long-term cumulative distribution function in Equation (2.7.8) can now be rewritten as (Giske, 2017):

$$F_{\tilde{R}_{LT}}(r) = \exp\left\{-T \int_{\mathbf{w}} \nu_X(r|\mathbf{w}) f_{\mathbf{w}}(\mathbf{w}) d\mathbf{w}\right\} \quad (2.7.10)$$

Here $\nu_X(r|\mathbf{w})$ denotes the mean upcrossing rate for the entire long-term period given the environmental parameters \mathbf{w} . Furthermore, $f_{\mathbf{w}}(\mathbf{w})$ denotes the joint probability density function over these environmental parameters.

Like in Equation (2.6.9), in the formulation in Equation (2.7.10) it is assumed that upcrossings of high levels r are statistically independent. In other words, these high-level upcrossings belong to a Poisson-distribution. Solving Equation (2.6.10) for the mean upcrossing rate gives the following:

$$\nu(r|\mathbf{w}) = -\frac{1}{T} \ln\left(F_{\tilde{R}|\mathbf{w}}(r|\mathbf{w})\right) \quad (2.7.11)$$

Introducing this expression into Equation (2.7.10) yields (Sagrilo et al., 2011):

$$F_{\tilde{R}_{LT}}(r) = \exp\left\{\int_{\mathbf{w}} \ln\left(F_{\tilde{R}|\mathbf{w}}(r|\mathbf{w})\right) f_{\mathbf{w}}(\mathbf{w}) d\mathbf{w}\right\}^{T/\tilde{T}} = F_{\tilde{R}}(r)^{\tilde{N}} \quad (2.7.12)$$

Here the fact that $T = \tilde{N}\tilde{T}$ is utilized. $F_{\tilde{R}}(r)$ is the long-term cumulative distribution function over the short-term extreme values as given in Equation (2.7.6). This means that the formulations in Equation (2.7.6) and (2.7.10) are equivalent to the assumption of independent upcrossings of high levels being the only one required.

2.7.4 Characteristic Values of the Extreme Response

The long-term extreme response can be connected to an annual exceedance probability q . This specified failure probability corresponds to a specific characteristic response r_q used for design purposes. This response value r_q can be found using the following requirement for the long-term cumulative distribution function $F_{\tilde{R}_{LT}}$ (Giske, 2017):

$$F_{\tilde{R}_{LT}}(r_q) = 1 - q \quad (2.7.13)$$

The response value r_q can also be approximated from the long-term cumulative distribution function over the short-term extreme values by requiring the following:

$$F_{\tilde{R}}(r_q) = (1 - q)^{1/\tilde{N}} \approx 1 - \frac{q}{\tilde{N}} \quad (2.7.14)$$

In Equation (2.7.14) the variable \tilde{N} denotes the number of short-term periods in one year.

2.8 Environmental Parameters

In order to describe environmental loading on structures certain assumptions regarding the probabilistic nature of the loads are necessary. Among such environmental loads are the wind loading, the water current, the significant wave height and the zero-crossing period. The two latter load types are here assumed to be the most relevant for floating bridges, meaning that the wind loading and water current are not considered in this thesis.

2.8.1 Significant Wave Height

The significant wave height is a statistical measure of wave height defined as the average height of the highest third of all wave heights. When measurements are used to determine the significant wave height, the waves are usually measured over a time period of twenty minutes. The recommended probability density function to describe the significant wave height H_s is the 3-parameter Weibull probability density function (Det Norske Veritas,

2010):

$$f_{H_s}(h) = \frac{\beta}{\alpha} \left(\frac{h - \gamma}{\alpha} \right)^{\beta-1} \exp \left\{ - \left(\frac{h - \gamma}{\alpha} \right)^\beta \right\} \quad (2.8.1)$$

In Equation (2.8.1) the parameters α , β and γ represent the scale, shape and location parameters of the distribution, respectively. These parameters are usually fitted to actual on-site measurements. However, due to the lack of such measurements in this project more general numbers are assumed for the scale and shape parameters, whereas the location parameter is assumed to be zero throughout this project.

The corresponding cumulative distribution function for the significant wave height is:

$$F_{H_s}(h) = 1 - \exp \left\{ - \left(\frac{h - \gamma}{\alpha} \right)^\beta \right\} \quad (2.8.2)$$

In Equation (2.8.1) and (2.8.2) h represents the stochastic realizations of the significant wave height.

2.8.2 Zero-Crossing Period

The wave zero-crossing period is defined as the average time interval between two consecutive upcrossings of the the mean sea level (Det Norske Veritas, 2010). The wave zero-crossing period T_z dependent on the significant wave height H_s can be accurately described using a lognormal distribution with the following probability density function (Det Norske Veritas, 2010):

$$f_{T_z|H_s}(t|h) = \frac{1}{\sigma t \sqrt{2\pi}} \exp \left\{ - \frac{(\ln(t) - \mu)^2}{2\sigma^2} \right\} \quad (2.8.3)$$

Here t denotes the variable describing all stochastic realizations of the zero-crossing period T_z . Furthermore, the distribution parameters μ and σ are functions of the significant wave height and are defined as:

$$\mu(h) = \mathbb{E}[\ln(T_z)] = a_0 + a_1 h^{a_2} \quad (2.8.4a)$$

$$\sigma(h) = \text{std}[\ln(T_z)] = b_0 + b_1 e^{b_2 h} \quad (2.8.4b)$$

The coefficients a_i and b_i need to be estimated from actual measured data. The corresponding cumulative distribution function for the zero-crossing period, $F_{T_z|H_s}$ is:

$$F_{T_z|H_s}(t|h) = \frac{1}{2} + \frac{1}{2} \operatorname{erf} \left[\frac{\ln(t) - \mu}{\sqrt{2}\sigma} \right] \quad (2.8.5)$$

In Equation (2.8.5) $\operatorname{erf}[\cdot]$ denotes the error function.

2.9 Stochastic Dynamical Behaviour of Sea Surfaces

Under the assumption of linear wave theory, the wave number $\kappa(\omega)$ is a function of the angular wave frequency ω defined implicitly through the following equation:

$$\omega^2 = \kappa g \tanh(\kappa d) \quad (2.9.1)$$

Here d denotes the water depth and g is the gravitational constant. For a given short-term period \tilde{T} the sea elevation can be modelled as a stationary homogeneous stochastic process with zero mean. This process is denoted $\eta(x, y, t)$, where x and y represent the spatial variables and t the time variable. For deep water conditions, i.e. when the ratio between the water depth d and the wave length L is greater than 0.5, the cross-spectral density for the sea elevation process can be expressed as a function of the wave frequency and -direction (Kvåle et al., 2016):

$$S_\eta(\omega, \theta) = S_\eta(\omega) D(\omega, \theta) \quad (2.9.2)$$

$D(\omega, \theta)$ represents the directional distribution as a function of the wave frequency ω and the wave angle θ relative to the considered structure. In an effort to make the directional distribution more suitable for practical applications the approximation $D(\omega, \theta) = D(\theta)$ is often adopted. That is, the frequency dependence is neglected (Naess and Moan, 2013). Under this assumption the following directional-dependent function is often used for $D(\theta)$:

$$D(\theta) = C(s) \left(\cos \left(\frac{\theta - \theta_0}{2} \right) \right)^{2s} \quad (2.9.3)$$

The factor $C(s)$ is a normalizing constant dependent on the spreading parameter s ensuring that $\int D(\theta) d\theta = 1$ and θ_0 is the mean wave angle. The normalizing constant

can be found from:

$$C(s) = \frac{1}{2\sqrt{\pi}} \frac{\Gamma(s+1)}{\Gamma(s+0.5)} \quad (2.9.4)$$

where Γ denotes the Gamma function. The spreading parameter s controls the crest length of the waves. In this thesis s is set constant equal to 13. However, this parameter is in reality frequency dependent and may also be considered as such.

Assuming deep water conditions and that the wave directional distribution is independent of the angular wave frequency for two given points r and s with mutual distances Δx and Δy the integral in Equation (2.9.5) gives the coherency between the wave heights at these points (Kvåle et al., 2016):

$$S_{\eta_r \eta_s} = S_{\eta}(\omega) \int_{-\pi}^{\pi} D(\theta) \exp \left\{ -i \frac{|\omega| \omega}{g} (\Delta x \cos(\theta) + \Delta y \sin(\theta)) \right\} d\theta \quad (2.9.5)$$

Numerous methods are used to idealize and describe oceanography. One such method is the use of wave spectral densities. An example is the *Pierson-Moskowitz* spectrum. This spectrum constitutes the basic form of the class of spectral densities that describe fully developed sea states. That is, sea states that are in equilibrium with the wind producing the waves. The basic form of the Pierson-Moskowitz spectrum is written as:

$$S_{\eta}(\omega) = \frac{A}{\omega^5} \exp \left\{ -\frac{B}{\omega^4} \right\} \quad (2.9.6)$$

where A and B are constants given as $A = \alpha g^2$ and $B = 1.25 \omega_p^4$. Here $\alpha = 0.0081$ is the Phillips constant, g is the gravitational constant and ω_p is the peak frequency at which $S_{\eta}(\omega)$ attains its maximum value.

The basic Pierson-Moskowitz spectrum can be modified to form several adjusted variants. One such variant is simply referred to as the *modified* Pierson-Moskowitz spectrum. In this case the coefficient A in Equation (2.9.6) is taken as $A = \frac{5}{16} H_s^2 \omega_p^4$. Compared to the original formulation, this formulation now introduces the significant wave height H_s as an additional parameter.

Another widely used modification of the basic Pierson-Moskowitz spectrum is the Joint North Sea Wave Project, or JONSWAP, spectrum. This spectrum is given by (Naess and

Moan, 2013):

$$S_{\eta}(\omega) = \frac{\tilde{\alpha}g^2}{\omega^5} \exp \left\{ -1.25 \frac{\omega_p^4}{\omega^4} \right\} \cdot \gamma^{a(\omega)} \quad (2.9.7)$$

In this model the basic Pierson-Moskowitz spectrum from Equation (2.9.6) is multiplied by a peak enhancement factor γ raised to a factor $a(\omega)$ which is expressed as:

$$a(\omega) = \exp \left\{ -\frac{(\omega - \omega_p)^2}{2\tilde{\sigma}^2\omega_p^2} \right\} \quad (2.9.8)$$

where the spectral width parameter $\tilde{\sigma}$ is given by:

$$\tilde{\sigma} = \begin{cases} \tilde{\sigma}_a = 0.07, & \text{for } \omega \leq \omega_p \\ \tilde{\sigma}_b = 0.09, & \text{for } \omega > \omega_p \end{cases} \quad (2.9.9)$$

Additionally, the Phillips constant α in Equation (2.9.6) is replaced with the constant $\tilde{\alpha}$ given by the following expression which is valid for offshore structures:

$$\tilde{\alpha} = 3.25 \cdot 10^{-3} H_s^2 \omega_p^4 (1 - 0.287 \ln(\gamma)) \quad (2.9.10)$$

In Figure 2.9.1 the Pierson-Moskowitz, modified Pierson-Moskowitz and the JONSWAP spectra are all plotted as functions of the frequency ratio ω/ω_p for a peak enhancement factor of $\gamma = 3$:

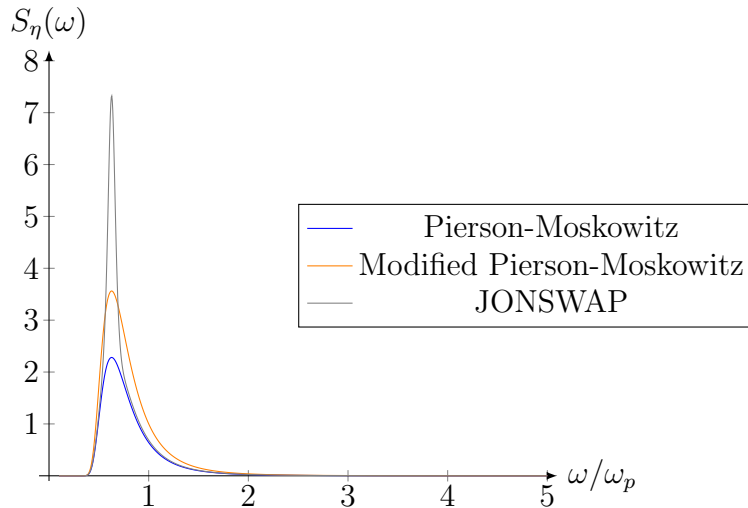


Figure 2.9.1: Pierson-Moskowitz, modified Pierson-Moskowitz and JONSWAP spectra plotted against frequency ratio for a peak enhancement factor of $\gamma = 3$. Significant wave height is taken as 5 meters and zero-crossing period as 10 seconds. Peak frequency is 0.6283 rad/s.

2.10 Fluid - Structure Interaction

The equation of motion for a floating structure can be expressed as (Kvåle et al., 2016):

$$\mathbf{M}_s \ddot{\mathbf{u}}(t) + \mathbf{C}_s \dot{\mathbf{u}}(t) + \mathbf{K}_s \mathbf{u}(t) = \mathbf{p}_h(t) \quad (2.10.1)$$

Here t is the time variable and \mathbf{M}_s , \mathbf{C}_s and \mathbf{K}_s are the structural or rigid-body mass, damping and stiffness matrices, respectively. $\mathbf{u}(t)$, $\dot{\mathbf{u}}(t)$ and $\ddot{\mathbf{u}}(t)$ are the displacement, velocity and acceleration vectors, respectively. $\mathbf{p}_h(t)$ denotes the total hydrodynamic action containing both the fluid-structure interaction and the wave action as expressed by the convolution integral in Equation (2.10.2):

$$\mathbf{p}_h(t) = - \int_{-\infty}^{\infty} \mathbf{m}_h(t - \tau) \ddot{\mathbf{u}}(t) d\tau - \int_{-\infty}^{\infty} \mathbf{c}_h(t - \tau) \dot{\mathbf{u}}(t) d\tau - \mathbf{K}_h \mathbf{u}(t) + \mathbf{p}(t) \quad (2.10.2)$$

Here the subscript h indicates hydrodynamic properties and τ represents the time lag in the convolution integral. $\mathbf{m}_h(t)$ and $\mathbf{c}_h(t)$ are the added hydrodynamic mass and damping, respectively. \mathbf{K}_h denotes the hydrodynamic stiffness, or buoyancy, of the structure while $\mathbf{p}(t)$ denotes the wave excitation forces. In the time domain, these mass and damping matrices can be described as the inverse Fourier transform of the hydrodynamic mass and damping matrices from the frequency domain:

$$\mathbf{m}_h(t) = \frac{1}{2\pi} \int_{-\infty}^{\infty} \mathbf{M}_h(\omega) e^{i\omega t} d\omega \quad (2.10.3a)$$

$$\mathbf{c}_h(t) = \frac{1}{2\pi} \int_{-\infty}^{\infty} \mathbf{C}_h(\omega) e^{i\omega t} d\omega \quad (2.10.3b)$$

Assuming deep water conditions and moderate wave height, the response process exhibits properties of both Gaussianity and homogeneity and can be expressed by a generalized harmonic decomposition (Kvåle et al., 2016):

$$\mathbf{u}(t) = \int_{-\infty}^{\infty} e^{i\omega t} d\mathbf{Z}_u(\omega) d\omega \quad (2.10.4a)$$

$$\mathbf{p}(t) = \int_{-\infty}^{\infty} e^{i\omega t} d\mathbf{Z}_p(\omega) d\omega \quad (2.10.4b)$$

Here $d\mathbf{Z}_u(\omega)$ and $d\mathbf{Z}_p(\omega)$ denote the spectral processes corresponding to the response vector and the wave excitation force vector, respectively. The wave loading forces are integrated pressure forces obtained from the solution of the diffraction potential (pressure effects related to the spreading of waves around a structure) over the average submerged surface of the structure. The equation of motion in Equation (2.10.1) can now be expressed as (Naess and Moan, 2013):

$$(-\omega^2 \mathbf{M}(\omega) + i\omega \mathbf{C}(\omega) + \mathbf{K}) d\mathbf{Z}_u(\omega) = d\mathbf{Z}_p(\omega) \quad (2.10.5)$$

For a rigid floating structure, the inertia, damping and restoring forces as a result of the fluid-structure interaction yield the following total system mass, stiffness and damping matrices:

$$\mathbf{M}(\omega) = \mathbf{M}_s + \mathbf{M}_h(\omega) \quad (2.10.6a)$$

$$\mathbf{C}(\omega) = \mathbf{C}_s + \mathbf{C}_h(\omega) \quad (2.10.6b)$$

$$\mathbf{K} = \mathbf{K}_s + \mathbf{K}_h \quad (2.10.6c)$$

Proceeding with the assumption of linear wave theory made in Section 2.9, it can be stated that the response \mathbf{u} belongs to a zero mean ergodic Gaussian process since Equation (2.10.5) describes a linear system. The frequency response method described in Section 2.4 is a direct approach to solve Equation (2.10.5). The method expresses the spectral process of the response in terms of the wave loading process (Langen and Sigbjörnsson, 1979):

$$d\mathbf{Z}_u(\omega) = \mathbf{H}(\omega) d\mathbf{Z}_p(\omega) \quad (2.10.7)$$

where $\mathbf{H}(\omega)$ denotes the frequency response transfer function:

$$\mathbf{H}(\omega) = (\mathbf{K} - \omega^2 \mathbf{M}(\omega) + i\omega \mathbf{C}(\omega))^{-1} \quad (2.10.8)$$

The spectral densities of the displacement response and wave action can be expressed as follows (Langen and Sigbjörnsson, 1979):

$$\mathbf{S}_u(\omega) d\omega = \mathbb{E} [d\mathbf{Z}_u(\omega) \cdot d\mathbf{Z}_u(\omega)^H] \quad (2.10.9a)$$

$$\mathbf{S}_p(\omega) d\omega = \mathbb{E} [d\mathbf{Z}_p(\omega) \cdot d\mathbf{Z}_p(\omega)^H] \quad (2.10.9b)$$

H denotes the Hermittian operator indicating a complex conjugate and matrix transpose while $\mathbb{E}[\cdot]$ denotes the expected value operator. Furthermore, the hydrodynamic forces acting on a submerged body due to a stochastic wave elevation process can be described as (Kvåle et al., 2016):

$$d\mathbf{Z}_h(\omega) = d\mathbf{Z}_p(\omega) - (-\omega^2 \mathbf{M}_h(\omega) + i\omega \mathbf{C}_h(\omega) + \mathbf{K}_h) d\mathbf{Z}_u(\omega) \quad (2.10.10)$$

Equation (2.10.10) describes the fluid-structure interaction and the wave action induced by the defined sea state. The wave induced load process $d\mathbf{Z}_p(\omega, \theta)$ can be written as the product of the hydrodynamic transfer function $\mathbf{Q}_r(\omega, \theta)$ and the spectral process for the sea surface elevation $d\mathbf{Z}_\eta(\omega, \theta)$:

$$d\mathbf{Z}_p(\omega, \theta) = \mathbf{Q}_r(\omega, \theta) d\mathbf{Z}_\eta(\omega, \theta) \quad (2.10.11)$$

$\mathbf{Q}_r(\omega, \theta)$ connects the forces caused by the waves with the wave amplitude process. The index r refers to the spatial location of a point or a pontoon. The reader is referred to the report with the title *Frequency Domain Analysis of a Floating Bridge Exposed to Irregular Short-Crested Waves* by Ivar Langen and Ragnar Sigbjörnsson (Langen and Sigbjörnsson, 1979) for a more detailed description of the this hydrodynamic transfer function in the context of hydrodynamic action on floating bridges.

The cross-spectral density matrix corresponding to the wave action process between two points r and s can be expressed as:

$$\mathbf{S}_{p_r p_s}(\omega) = \int_{\theta} \mathbf{Q}_r(\omega, \theta) \mathbf{S}_{\eta_r \eta_s} \mathbf{Q}_s(\omega, \theta)^H d\theta \quad (2.10.12)$$

$\mathbf{Q}_r(\omega, \theta)$ and $\mathbf{Q}_s(\omega, \theta)$ are the directional wave excitation transfer functions for element r and s , respectively (Kvåle et al., 2016). $\mathbf{S}_{\eta_r \eta_s}$ is the cross-spectral density matrix between the wave elevation process at the points r and s as defined in Equation (2.9.5). By combining Equation (2.10.10) with Equation (2.10.9a) and (2.10.9b), the expression relating the load spectrum to the response spectrum can be written as:

$$\mathbf{S}_u(\omega) = \mathbf{H}(\omega) \mathbf{S}_p(\omega) \mathbf{H}(\omega)^H \quad (2.10.13)$$

2.11 IFORM

The First-Order Reliability Method (FORM) is a widely known method in the field of structural reliability. Given the resistance R of a structure and the external loads S acting on this structure, the safety margin M is given as $M = R - S$. From this, the corresponding reliability index β is given as:

$$\beta = \frac{\mathbb{E}[M]}{\text{std}[M]} = \frac{\mathbb{E}[R] - \mathbb{E}[S]}{\sqrt{\text{Var}[R] + \text{Var}[S]}} = \frac{\mu_R - \mu_S}{\sqrt{\sigma_R^2 + \sigma_S^2}} \quad (2.11.1)$$

Here $\mathbb{E}[\cdot]$, $\text{std}[\cdot]$ and $\text{Var}[\cdot]$ denote the expected value, standard deviation and variance operators, respectively. Furthermore, μ_R and μ_S denote the mean value of the structural resistance and of the loading while σ_R and σ_S represent the standard deviations of these same quantities, respectively.

Structural failure occurs when the loading on the structure exceeds the structural resistance, i.e. when $R - S < 0$. A limit state function $g(\mathbf{X})$ dependent on the random variables \mathbf{X} describing the failure surface of the structural system can be defined as:

$$g(\mathbf{X}) = R - S < 0 \quad (2.11.2)$$

The probability of failure p_f can then be expressed using the following cumulative distribution formulation:

$$p_f = P(g(\mathbf{X}) \leq 0) = P(M \leq 0) = \Phi(-\beta) \quad (2.11.3)$$

Here Φ denotes the standard normal cumulative distribution function. Figure 2.11.1 shows a geometrical interpretation of the reliability index β when the loading on the structure S and the structural resistance R are considered as two independent normal distributed random variables:

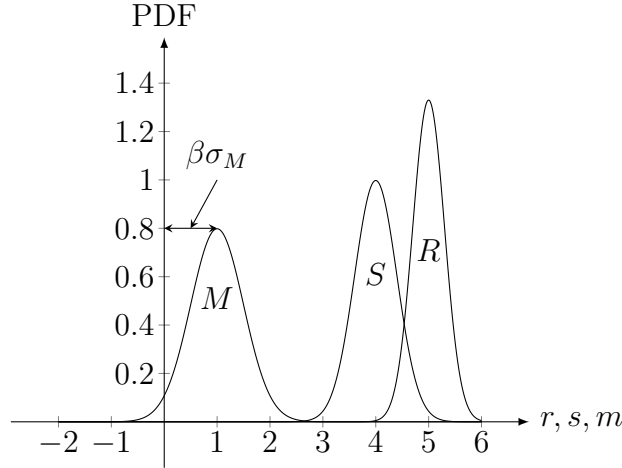


Figure 2.11.1: Definition of the reliability index β . The index defines the mean value of the safety margin M as a function of its standard deviation σ_M : $\mu_M = \beta\sigma_M$ (Köhler, 2018).

A vector of random variables $\mathbf{V} = [\mathbf{W}, R]$ is introduced together with the joint probability density function $f_{\mathbf{V}}(\mathbf{v}) = f_{\tilde{R}|\mathbf{W}}(\tilde{r}|\mathbf{w})f_{\mathbf{W}}(\mathbf{w})$ over these variables. The vector \mathbf{V} here includes both the environmental parameters \mathbf{W} and the response R of the structure. The factor $f_{\tilde{R}|\mathbf{W}}(\tilde{r}|\mathbf{w})$ represents the probability density function of the response given the environmental parameters \mathbf{W} while $f_{\mathbf{W}}(\mathbf{w})$ represents the probability density function for these variables themselves. From this the following reliability problem can be formulated:

$$\bar{F}_{\tilde{R}}(r) = 1 - \int_{G_r(\mathbf{v}) \leq 0} f_{\mathbf{V}}(\mathbf{v}) d\mathbf{v} = 1 - p_f(r) \quad (2.11.4)$$

$G_r(\mathbf{v}) = r - \tilde{r}$ represents the limit state function whereas $p_f(r)$ denotes the failure probability for a given response value r . Equation (2.7.6) can be used to establish the exact formulation for the cumulative distribution function for the long-term extreme response as a reliability problem (Giske et al., 2017):

$$F_{\tilde{R}}(r) = \exp \left\{ \int_{\mathbf{w}} \left(1 + \ln \left(F_{\tilde{R}|\mathbf{W}}(r|\mathbf{w}) \right) \right) f_{\mathbf{W}}(\mathbf{w}) d\mathbf{w} - 1 \right\} \quad (2.11.5)$$

By introducing the stochastic response variable Y , the cumulative distribution function can be written as:

$$F_{Y|\mathbf{W}}(y|\mathbf{w}) = \max \left\{ 1 + \ln \left(F_{\tilde{R}|\mathbf{W}}(y|\mathbf{w}) \right), 0 \right\} \quad (2.11.6)$$

Equation (2.11.6) can then be used to express the short-term extreme response as:

$$F_{\bar{R}}(r) \approx \exp \left\{ \int_{\mathbf{w}} F_{Y|\mathbf{W}}(r|\mathbf{w}) f_{\mathbf{W}}(\mathbf{w}) d\mathbf{w} - 1 \right\} \quad (2.11.7)$$

Finally, Equation (2.11.7) can be written as a reliability problem as follows:

$$F_{\bar{R}}(r) \approx \exp \left\{ - \int_{G_r(\mathbf{v}) \leq 0} f_{\mathbf{V}}(\mathbf{v}) d\mathbf{v} \right\} = \exp\{-p_f(r)\} \quad (2.11.8)$$

The approximate formulation for the cumulative distribution function for the long-term extreme response in Equation (2.7.7) can also be rewritten as a reliability problem (Giske et al., 2017):

$$\bar{F}_{\bar{R}}(r) = \int_{\mathbf{w}} F_{\bar{R}|\mathbf{W}}(r|\mathbf{w}) f_{\mathbf{W}}(\mathbf{w}) d\mathbf{w} = \int_{\mathbf{w}} \int_{\tilde{r} \leq r} f_{\bar{R}|\mathbf{W}}(\tilde{r}|\mathbf{w}) d\tilde{r} f_{\mathbf{W}}(\mathbf{w}) d\mathbf{w} \quad (2.11.9)$$

Using FORM the probability of failure $p_f(r)$ for a given response level r can be obtained. The joint probability density function $f_{\mathbf{V}}(\mathbf{v})$, which is a function of the random variable $\mathbf{V} = [\mathbf{W}, R]$ or $\mathbf{V} = [\mathbf{W}, Y]$ depending on if it is the exact or approximate expression that is being used, should be transferred to a standard normal space. In this thesis, this space is referred to as the U-space. This space has the three components described by the vector $\mathbf{U} = [U_1, U_2, U_3]$. The transformation from V- to U-space is performed using the *Rosenblatt* transformation (Köhler, 2018):

$$\begin{aligned} \Phi(U_1) &= F_{V_1}(V_1) \\ \Phi(U_2) &= F_{V_2|V_1}(V_2|V_1) \\ &\vdots \\ \Phi(U_i) &= F_{V_i|V_1, V_2, \dots, V_{i-1}}(V_i|V_1, V_2, \dots, V_{i-1}), \quad i = 1, 2, \dots, n \\ \Phi(U_{n+1}) &= F_{V_{n+1}|V_1, V_2, \dots, V_n}(V_{n+1}|V_1, V_2, \dots, V_n) \end{aligned} \quad (2.11.10)$$

Here n is the number of random variables in the vector \mathbf{V} . F_{V_i} is the cumulative distribution function for the i -th random variable in the physical space. $\Phi(\cdot)$ denotes the cumulative standard normal distribution function. Furthermore, the expression for the realization of the random variables \mathbf{V} can be written in terms of standard normal

distributed random variables in U-space as:

$$\begin{aligned}
v_1(\mathbf{u}) &= F_{V_1}^{-1}(\Phi(u_1)) \\
v_2(\mathbf{u}) &= F_{V_2|V_1}^{-1}(\Phi(u_2|v_1(\mathbf{u}))) \\
v_i(\mathbf{u}) &= F_{V_i|V_1, \dots, V_{i-1}}^{-1}(\Phi(u_i|v_1(\mathbf{u}), v_2(\mathbf{u}), \dots, v_{i-1}(\mathbf{u}))), \quad i = 1, 2, \dots, n \\
&\vdots \\
v_{n+1}(\mathbf{u}) &= F_{V_{n+1}|V_1, \dots, V_n}^{-1}(\Phi(u_{n+1}|v_1(\mathbf{u}), v_2(\mathbf{u}), \dots, v_n(\mathbf{u})))
\end{aligned} \tag{2.11.11}$$

The failure probability can now be written using the joint probability density function in U-space:

$$p_f(r) = \int_{g_r(\mathbf{u}) \leq 0} f_U(\mathbf{u}) d\mathbf{u} = \Phi(-\beta) \tag{2.11.12}$$

where the limit state function is expressed as $g_r(\mathbf{u}) = r - v_{n+1}(\mathbf{u})$ with β being the distance from the origin to the $(n+1)$ -dimensional hyperplane defined by $g_r(\mathbf{u}) = 0$, also known as the failure surface. $v_{n+1}(\mathbf{u})$ denotes the realization of the stochastic variable \mathbf{V} in the physical space. The reliability index β is calculated by solving the following optimization problem (Giske et al., 2017):

$$\beta = \min|\mathbf{u}|; \quad \text{subject to } g_r(\mathbf{u}) = 0 \tag{2.11.13}$$

Equation (2.11.4) and (2.11.5) which express the approximate and exact formulation of the reliability problem, respectively, can now be written as:

$$\bar{F}_{\bar{R}}(r) \approx 1 - \Phi(-\bar{\beta}_r) \tag{2.11.14a}$$

$$F_{\bar{R}}(r) \approx \exp\{-\Phi(-\beta_r)\} \tag{2.11.14b}$$

where β_r is the reliability index that corresponds to the minimum distance between the origin and the limit state function, mathematically expressed as:

$$\beta_r = |\mathbf{u}^*| \tag{2.11.15}$$

Here \mathbf{u}^* is known as the design point. This point gives information about both the environmental parameters giving the largest response value, as well as this response value

itself. The limit state function is in general non-linear and is linearized at the design point \mathbf{u}^* as seen in Figure 2.11.2. This linearization is the defining property of the first-order reliability methods, FORM and IFORM (Haver et al., 2013).

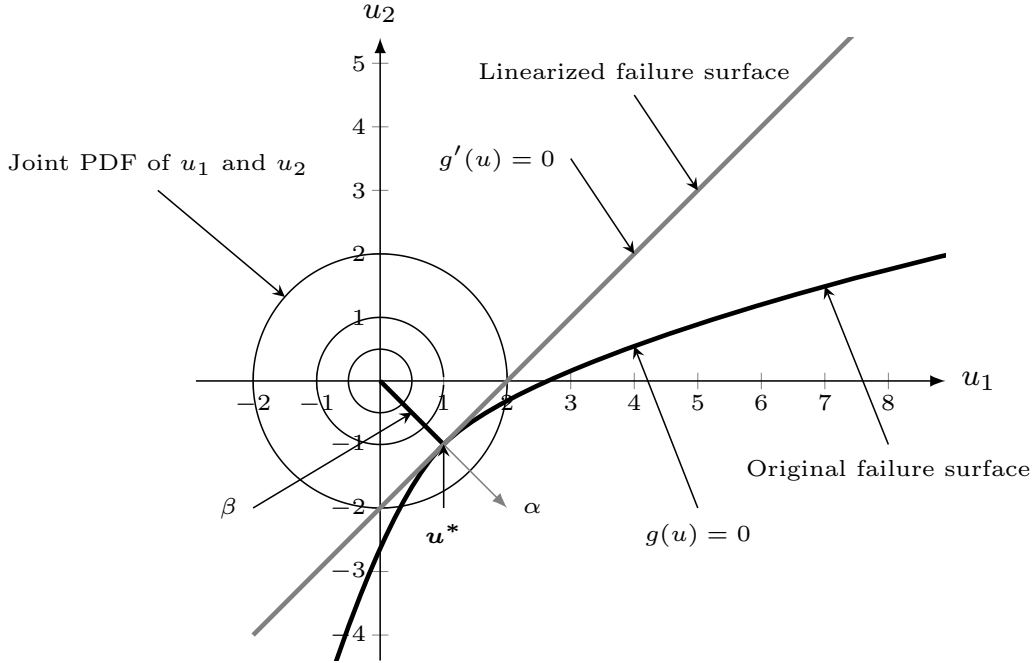


Figure 2.11.2: FORM-algorithm illustrated.

In the context of FORM the cumulative distribution functions $\bar{F}_{\bar{R}}(r)$ and $F_{\bar{R}}(r)$ for the short-term extreme response are evaluated for a given response value r . Nonetheless, in structural design it is more common to go the other way around. The response r is instead calculated from a predefined annual exceedance probability. When considering the M -year extreme response r_M , this probability of exceedance can be calculated by requiring the following of the cumulative distribution function for the extreme response:

$$F_{\bar{R}}(r_M) = \left(1 - \frac{1}{M}\right)^{\frac{1}{\tilde{N}}} \approx 1 - \frac{1}{M\tilde{N}} \quad (2.11.16)$$

Here \tilde{N} denotes the number of short-term periods in a year and is given by $\tilde{N} = 365 \cdot (24/\tilde{T})$, where \tilde{T} is the duration of each short-term period given in hours. The fraction $24/\tilde{T}$ then gives the number short-term periods in a day. Using Equation (2.11.14b) the reliability index can now be calculated as:

$$\beta = -\Phi^{-1}(-\ln(F_{\bar{R}}(r_M))) \quad (2.11.17)$$

Given a probability of exceedance, the corresponding reliability index is calculated and the design point \mathbf{u}^* is located in an iterative manner in order to satisfy the optimization problem from Equation (2.11.13). The M -year response value r_M should also satisfy the limit state function $g_{r_M}(\mathbf{u}) = r_M - v_{n+1}(\mathbf{u}) = 0$ where v_{n+1} is given in Equation (2.11.11). This is summarized in the following expression:

$$r_M = \max \{v_{n+1}(\mathbf{u})\}; \text{ subject to } |\mathbf{u}| = \beta \quad (2.11.18)$$

When applying the method of Lagrange multipliers (a technique for locating the local maxima or minima of a function) the design point must satisfy the following recursive expression (Xu et al., 2018):

$$\frac{\mathbf{u}^*}{|\mathbf{u}^*|} = \frac{\nabla v_{n+1}(\mathbf{u}^*)}{|\nabla v_{n+1}(\mathbf{u}^*)|} = \alpha \quad (2.11.19)$$

Here ∇ and $|\cdot|$ are the gradient and vector length operators, respectively. Thus, $\nabla v_{n+1}(\mathbf{u}^*)$ and $|\nabla v_{n+1}(\mathbf{u}^*)|$ denote the gradient of $v_{n+1}(\mathbf{u}^*)$ and the length of this gradient, respectively. α is a normal vector to the failure surface as can be seen in Figure 2.11.2. A solution which satisfies Equation (2.11.19) based on the *steepest decent method for minimization* (Giske et al., 2017) is given by:

$$\mathbf{u}^{k+1} = \beta \frac{\nabla v_{n+1}(\mathbf{u}^k)}{|\nabla v_{n+1}(\mathbf{u}^k)|} \quad (2.11.20)$$

Equation (2.11.20) may encounter convergence issues due to the fact that the gradient $\nabla v_{n+1}(\mathbf{u})$ is assumed constant in the search direction. A backtracking approach proposed by Giske (2017) aims to solve these convergence issues by requiring that the increase of $v_{n+1}(\mathbf{u})$ is proportional to the step length and the directional derivative at the point \mathbf{u}^k along the search direction (Giske, 2017). In applications this requirement is fulfilled by ensuring that:

$$v_{n+1}(\mathbf{u}^{k+1}) - v_{n+1}(\mathbf{u}^k) \geq cd\alpha_b \quad (2.11.21)$$

Here $c \in (0, 1)$ is a proportionality constant while d and α_b denote the directional derivative and the step length, respectively:

$$d = \frac{1}{\beta} \sqrt{\beta^2 |\nabla v_{n+1}(\mathbf{u}^k)|^2 - (\mathbf{u}^k \cdot \nabla v_{n+1}(\mathbf{u}^k))^2} \quad (2.11.22a)$$

$$\alpha_b = \beta \arccos \left(\frac{\mathbf{u}^k \cdot \nabla v_{n+1}(\mathbf{u}^k)}{\beta |\nabla v_{n+1}(\mathbf{u}^k)|} \right) \quad (2.11.22b)$$

This iterative IFORM-procedure is initiated with an assumed initial value $\mathbf{u}^k = \mathbf{u}^1$ and is repeated until the alleged design point is found and a pre-defined tolerance is met:

$$\frac{|\mathbf{u}^{k+1} - \mathbf{u}^k|}{|\mathbf{u}^{k+1}|} < \text{Tolerance} \quad (2.11.23)$$

2.12 The Environmental Contour Method

When structural problems are complex, it can be convenient to use methods which can provide an approximate solution of the problem at hand in a computationally inexpensive manner. The Environmental Contour Method (ECM) aims to decouple the uncertainties related to the environmental loads and to the extreme response given these loads (Winterstein and Haver, 1993). Given the joint probability density function for the environmental parameters, $f_{\mathbf{w}}(\mathbf{w})$, the environmental contour corresponding to a pre-defined annual exceedance probability q is calculated without the structural response taken into account. The most unfavourable combination of the environmental parameters along this isoprobability contour is used as the design point and is denoted $\hat{\mathbf{w}}$. The median, or 0.5-fractile value, of the short-term distribution $F_{\hat{r}|\mathbf{w}}(r|\mathbf{w})$ attains its maximum value at $\hat{\mathbf{w}}$ (Giske, 2017).

The assumption of independence between the environmental loads and the structural response opens the possibility for regarding the structural response as deterministic. The IFORM-algorithm can be utilized to solve for the design point $\hat{\mathbf{w}}$ through the optimization problem defined in Equation (2.11.18). With the response regarded as deterministic, the optimization problem would contain one less dimension leaving the reliability index β expressed as (Winterstein and Haver, 1993):

$$\beta = |\mathbf{U}| = \sqrt{U_1^2 + U_2^2 + \dots + U_n^2} \quad (2.12.1)$$

where $\mathbf{U} = [U_1, U_2, \dots, U_n]$ are the the environmental parameters in the standard normal U-space. The β -value corresponding to the M -year extreme response can be calculated from Equation (2.11.17).

In order to take the stochastic behaviour of the short-term extreme response into account the characteristic response value r_q is found from a p_q -fractile value of the short-term extreme value distribution $F_{\tilde{R}|\mathbf{W}}(r_q|\hat{\mathbf{w}})$ at the design point $\hat{\mathbf{w}}$ (Haver et al., 2013). This value is often chosen as $p_q > 0.5$ and is used as a requirement in the following way:

$$p_q = F_{\tilde{R}|\mathbf{W}}(r_q|\hat{\mathbf{w}}) \quad (2.12.2)$$

2.13 Gaussian Process Regression

Gaussian Process Regression (GPR) is a machine learning technique with applications in several different fields. These include, but are not limited to, algorithm configuration and computer animations as well as weather forecasting (de Freitas, 2013). Based on a few training points the method is able to predict estimates in areas with insufficient prior data, while simultaneously estimating the error in these predictions. In this thesis Gaussian Process Regression is used for prediction of long-term extreme response values based on pre-simulated environmental parameters. More specifically, on realizations of the significant wave height and zero-crossing period randomly drawn from their respective probability distributions.

Consider a joint set of two multivariate normal (Gaussian) distributed random variables $\mathbf{x} = (x_1, x_2)$. The parameters of this multivariate Gaussian can be expressed in terms of the mean vector ($\boldsymbol{\mu}$), in addition to the covariance ($\boldsymbol{\Sigma}$) and precision matrix ($\boldsymbol{\Lambda}$):

$$\boldsymbol{\mu} = \begin{bmatrix} \mu_1 \\ \mu_2 \end{bmatrix}, \quad \boldsymbol{\Sigma} = \begin{bmatrix} \Sigma_{11} & \Sigma_{12} \\ \Sigma_{21} & \Sigma_{22} \end{bmatrix}, \quad \boldsymbol{\Lambda} = \boldsymbol{\Sigma}^{-1} = \begin{bmatrix} \Lambda_{11} & \Lambda_{12} \\ \Lambda_{21} & \Lambda_{22} \end{bmatrix} \quad (2.13.1)$$

From these parameters the marginal distribution over x_1 and x_2 can be expressed as:

$$p(x_1) = \mathcal{N}(x_1|\mu_1, \Sigma_{11}) \quad (2.13.2a)$$

$$p(x_2) = \mathcal{N}(x_2|\mu_2, \Sigma_{22}) \quad (2.13.2b)$$

The posterior conditional, i.e. the probability of observing x_1 given x_2 , is expressed as:

$$p(x_1|x_2) = \mathcal{N}(x_1|\mu_{1|2}, \Sigma_{1|2}) \quad (2.13.3)$$

where the conditional mean and covariance are given as (Murphy, 2007):

$$\mu_{1|2} = \mu_1 + \Sigma_{12}\Sigma_{22}^{-1}(x_2 - \mu_2) \quad (2.13.4a)$$

$$\Sigma_{1|2} = \Sigma_{11} - \Sigma_{12}\Sigma_{22}^{-1}\Sigma_{21} = \Lambda_{11}^{-1} \quad (2.13.4b)$$

Here it is assumed that the matrix Σ is positive definite. Particularly, this means that the matrix should be symmetric and have positive eigenvalues (Weisstein, 2021). These expressions for the conditional mean and covariance will be revisited later in this section.

Gaussian Process Regression can be used to fit highly nonlinear functions to some set of known data points. As an example, consider the three known values x_1 , x_2 and x_3 . To each of these three values, there exist three corresponding function values f_1 , f_2 and f_3 . This is illustrated in Figure 2.13.1 (a):

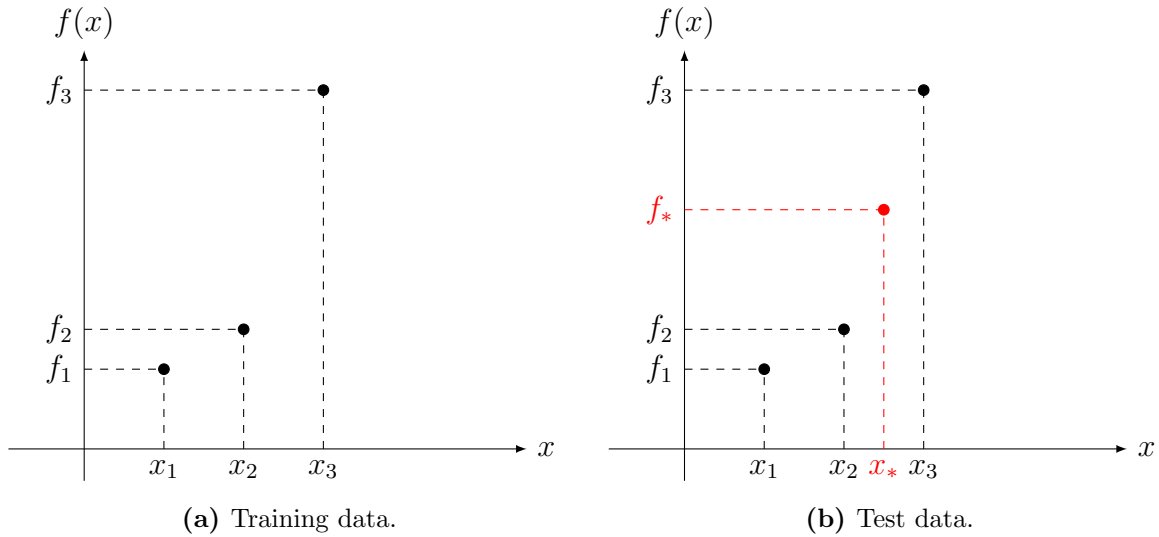


Figure 2.13.1: Data points for Gaussian Process Regression.

In order to model the function values f_1 , f_2 and f_3 , one can start by assuming that these function values come from a multivariate Gaussian distribution. This gives the following:

$$\begin{bmatrix} f_1 \\ f_2 \\ f_3 \end{bmatrix} \sim \mathcal{N}(\boldsymbol{\mu}, \mathbf{K}) = \mathcal{N}\left(\begin{bmatrix} \mu_1 \\ \mu_2 \\ \mu_3 \end{bmatrix}, \begin{bmatrix} K_{11} & K_{12} & K_{13} \\ K_{21} & K_{22} & K_{23} \\ K_{31} & K_{32} & K_{33} \end{bmatrix}\right) \quad (2.13.5)$$

In Equation (2.13.5) the term $\boldsymbol{\mu}$ represents a vector containing the mean value of each of the functions and \mathbf{K} denotes the covariance matrix for this same set of functions.

The elements in the covariance matrix, K_{ij} , each acts as a measure of similarity between the values x_1 , x_2 and x_3 . The diagonal terms give the variance while the off-diagonal terms give the covariance between the points. In order to construct each of these matrix elements one will have to use a function that returns the number 1 where $i = j$ and a number between 0 and 1 where $i \neq j$. A very common function used to achieve this is the squared exponential kernel:

$$K_{ij} = \exp \left\{ -\frac{1}{2} \|x_i - x_j\|^2 \right\} = \begin{cases} 0 & \text{when } \|x_i - x_j\| \rightarrow \infty \\ 1 & \text{when } x_i = x_j \end{cases} \quad (2.13.6)$$

As can be seen from Equation (2.13.6), as the distance between the considered points x_i and x_j grows large the correlation between the points decreases accordingly. Likewise, as the distance between the points decreases the correlation between the points increases. For intermediate distances, the squared exponential kernel will return a value between 0 and 1, as desired.

Until now, only the three points x_1 , x_2 and x_3 have been considered. If another point x_* is added, the corresponding function value f_* can be estimated using Gaussian Process Regression. This new point and its corresponding function value are depicted in Figure 2.13.1 (b). As for f_1 , f_2 and f_3 the function value f_* is also assumed to belong to a Gaussian distribution:

$$f_* \sim \mathcal{N}(\mu_*, K_{**}) \quad (2.13.7)$$

Here μ_* represents the mean value of this new function value f_* , while K_{**} represents the covariance of this function. The known values x_1 , x_2 and x_3 and the corresponding function values f_1 , f_2 and f_3 are referred to as training data. This comes from the fact that this data set represents known points and is used to *train* or adjust the algorithm to fit these values. For noiseless data, the training set of N points can be written in a more compact way as (de Freitas, 2013):

$$\mathcal{D} = \{(\mathbf{x}_i, f_i), i = 1 : N\}, \text{ where } f_i = f(\mathbf{x}_i) \quad (2.13.8)$$

The set of unknown values \mathbf{x}_* and the corresponding function values \mathbf{f}_* are on the other hand referred to as test data. This data set are used to *test* the algorithm and contains

estimated values. Given a test set \mathbf{x}_* of size $N_* \times D$ the function outputs \mathbf{f}_* are to be calculated. Since both the training data and the test data are assumed to belong to the same probability distribution and also to be correlated, the total data set can be written as:

$$\begin{bmatrix} \mathbf{f} \\ \mathbf{f}_* \end{bmatrix} \sim \mathcal{N} \left(\begin{bmatrix} \boldsymbol{\mu} \\ \boldsymbol{\mu}_* \end{bmatrix}, \begin{bmatrix} \mathbf{K} & \mathbf{K}_* \\ \mathbf{K}_*^T & \mathbf{K}_{**} \end{bmatrix} \right) \quad (2.13.9)$$

Following the multivariate Gaussian theorem described in Equation (2.13.1) through (2.13.4), the mean and variance for the test data \mathbf{f}_* can be found from:

$$\boldsymbol{\mu}_* = \mathbb{E} [f_*] = \mathbf{K}_*^T \mathbf{K}^{-1} \mathbf{f} \quad (2.13.10a)$$

$$\boldsymbol{\sigma}_* = -\mathbf{K}_*^T \mathbf{K}^{-1} \mathbf{K}_* + \mathbf{K}_{**} \quad (2.13.10b)$$

Having derived the expressions for the mean and variance of the test points, it is now possible to predict these quantities for any x_* . By predicting these quantities for a large number of test points it is possible to approximate continuous curves, one curve representing the mean value and another representing the variance. Each point on these curves corresponds to a predicted mean value or a variance value. This is the main idea in Gaussian Process Regression. The procedure is similar to a mathematical function where test data x_* are used as input and the mean and variance of this data are returned. In other words, Gaussian Process Regression represents a distribution over functions.

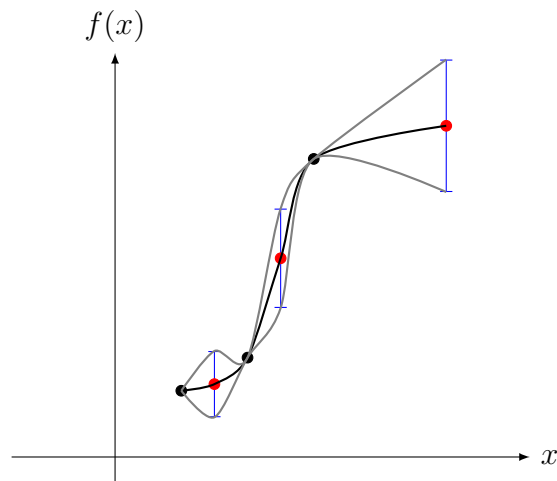


Figure 2.13.2: Estimated function using Gaussian Process Regression. The black points represent the training points while the red points represent the test points. The resulting confidence intervals are indicated by the blue bars.

Figure 2.13.2 shows a mean curve fitted to the training and test data, along with confidence intervals representing the variance of the test data. The confidence intervals act as a measure of uncertainty. As seen from the figure this uncertainty will disappear at the training data points. At these points the function value is known and therefore no uncertainty is observed here. However, at the test data points there exist uncertainty. An important observation to be made from Figure 2.13.2 is that where there is data the uncertainty is low, while where there is no data the uncertainty will be higher. Especially the rightmost point in the figure exhibits large uncertainty. Here the mean curve will be extrapolated based on the training points. Figure 2.13.2 shows an example of noiseless data. It is important to note that for data with noise the uncertainty will not disappear completely, not even at points where there is data.

The kernel in Equation (2.13.6) can be modified through the use of hyperparameters. Common hyperparameters are the signal variance σ^2 and the length scale l . The signal variance acts as a scaling factor defining the variation of the function values relative to the mean value. In other words, it defines the width of the confidence intervals. On the other hand, the length scale determines how rapidly the uncertainty will increase or decrease when leaving or approaching a training point (de Freitas, 2013). In other words, the length scale defines the smoothness of the function. Adding the signal variance and the length scale to the expression in Equation (2.13.6) yields:

$$K_{ij} = \sigma^2 \exp \left\{ -\frac{1}{2l^2} \|x_i - x_j\|^2 \right\} \quad (2.13.11)$$

2.14 Crude Monte Carlo Simulation and Importance Sampling

Crude Monte Carlo Simulation (CMCS) relies on repeated random sampling to obtain numerical results. In this thesis CMCS is used to generate samples from given probability distributions in an effort to simulate the real-world characteristics of extreme responses and the randomness it exhibits. The short-term extreme response distribution in CMCS

can be formulated as (Sagrilo et al., 2011):

$$F_R(r) = \exp \left\{ -\frac{T}{N_M} \sum_{i=1}^{N_M} \nu_R(r|\mathbf{w}_i) \right\} \quad (2.14.1)$$

Here T denotes the long-term period whereas $\nu_R(r|\mathbf{w}_i)$ represents the upcrossing rate given the environmental parameters \mathbf{w}_i which are sampled from their joint PDF given by Equation (2.6.5). N_M is the number of simulated samples. N_M should be chosen as a sufficiently high number for the simulation to converge and for facilitating unbiased results. However, a high number of simulated samples contributes to making CMCS rather computationally expensive (Sagrilo et al., 2011). One remedy for improving the efficiency of the method is through the technique of Importance Sampling (Melchers and Beck, 2008). This technique centers the generated environmental parameters around the region in the joint PDF which contributes the most to the response. This is achieved by assigning a weight to the conditional upcrossing rate as shown in Equation (2.14.2):

$$F_R(r) = \exp \left\{ -T \int_{\mathbf{w}} \nu_R(r|\mathbf{w}_i) \underbrace{\frac{f_{\mathbf{w}}(\mathbf{w})}{h_{\mathbf{w}}(\mathbf{w})}}_{weight} h_{\mathbf{w}}(\mathbf{w}) d\mathbf{w} \right\} \quad (2.14.2)$$

In discrete form this can be written as:

$$F_R(r) = \exp \left\{ -\frac{T}{N_M} \sum_{i=1}^{N_M} \nu_R(r|\mathbf{w}_i) \underbrace{\frac{f_{\mathbf{w}}(\mathbf{w})}{h_{\mathbf{w}}(\mathbf{w})}}_{weight} \right\} \quad (2.14.3)$$

Here $h_{\mathbf{w}}(\mathbf{w})$ denotes the importance density function.

CHAPTER 3

Methodology

The long-term extreme response analysis is carried out using the different methods presented. Their implementations along with the assumptions made are presented in this chapter. As an illustration, the methods are applied to a simplified finite element model based on the Bergsøysund Bridge.

3.1 Modelling the Bergsøysund Bridge

A simplified model based on the Bergsøysund Bridge is created using Abaqus, which is a software solution for finite element analysis. The main purpose of this simplified model is to exemplify the different approaches to long-term extreme response calculations and not necessarily to simulate the exact extreme response of the bridge.

Python is used to develop an input file containing the bridge geometry and material properties as well as the loading and boundary conditions for further analysis in Abaqus. Hydrostatic mass and stiffness of the pontoons are introduced to the finite element model from the hydrodynamic software solution named WADAM.

3.1.1 The Bridge Superstructure

The bridge deck is supported by an intricate truss structure which is quite complicated to model and the need for several types of finite elements is inevitable. However, a highly sophisticated finite element model is not considered feasible for the purpose of this project. Therefore, the main load carrying system of the bridge is simplified. The bridge deck is modelled using B31 Timoshenko beam elements. These three-dimensional elements are defined from two nodes each with six degrees-of-freedom (DOFs), three translational and three rotational (Abaqus, 2014). All elements are straight lines with a length of 105 meters each, namely one element between each pontoon. The geometrical properties assigned to these beams are based on the work of Hermstad (2013) and Heuberger (2018). In the former, the beam data are extracted from the actual cross-section of the bridge deck including the mass of the asphalt layer. In the software *Cross-X* these properties are merged into a single beam element. Lastly, the properties originating from the bridge deck are added to the corresponding properties for the truss structure provided by Heuberger (2018) to form the total values given in Table 3.1.1:

Table 3.1.1: Cross-sectional properties used for the bridge model. The properties originate from both the bridge deck and main load-carrying system.

Area	A [m ²]	0.557
Mass	ρ [kg/m]	6723
Second moment of area	I_y [m ⁴]	5.85
	I_{yz} [m ⁴]	0
	I_z [m ⁴]	11.7
St. Venants torsional constant	I_T [m ⁴]	15.1

The material properties used for the steel components in the model are given in Table 3.1.2:

Table 3.1.2: Material properties used in the bridge model.

Elasticity modulus	E [N/m ²]	$200 \cdot 10^9$
Shear modulus	G [N/m ²]	$76.9 \cdot 10^9$
Poisson's ratio	ν [-]	0.3

3.1.2 pontoons

Assuming that all the seven waterborne pontoons for the Bergsøysund Bridge are identical, each pontoon is modelled as a rigid structure using Det Norske Veritas' (DNV's) GeniE software. Geometrical dimensions for pontoon 4 can be found in Appendix A.1. The FEM-file containing the meshed finite element model of a representative pontoon is exported to a WADAM-engine in the software HydroD for further hydrodynamic simulations. WADAM is another product from DNV which in this thesis is mainly used to obtain the hydrodynamic transfer functions as well as the necessary hydrodynamic mass, stiffness and damping used to represent the properties and behaviour of the pontoons. The discretization of the frequencies and wave angles used in this project are presented in Table 3.1.3, where the angle is defined as the angle between the positive local x-axis of the pontoon and the wave direction, see Figure 3.1.1.

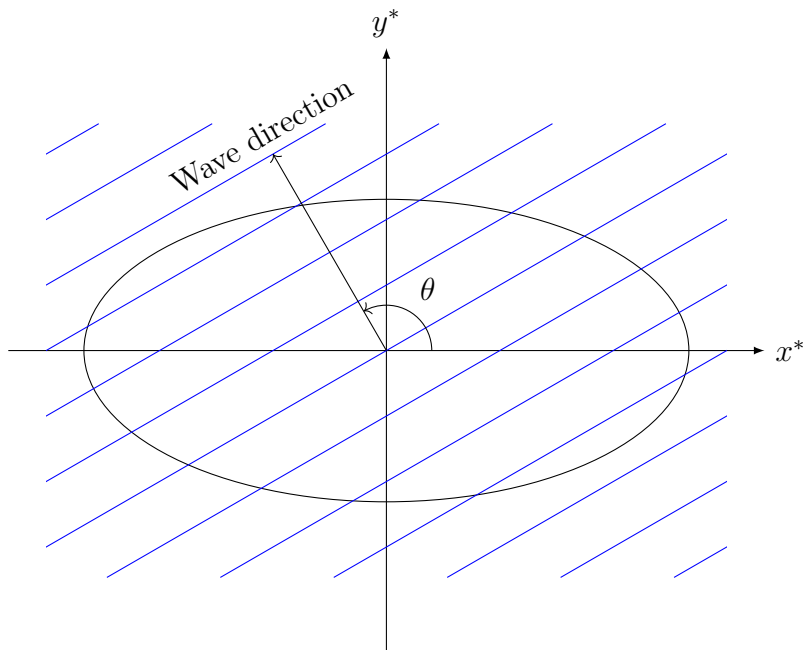
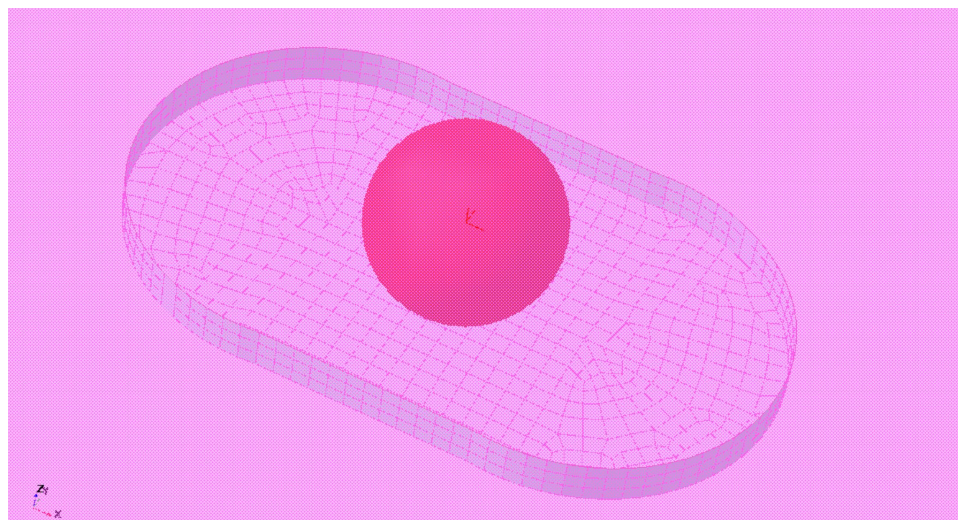


Figure 3.1.1: Wave angle definition. The parallel blue lines represent the wave crests. The wave angle θ is defined as the angle between the positive local x-axis of the pontoon and the wave direction.

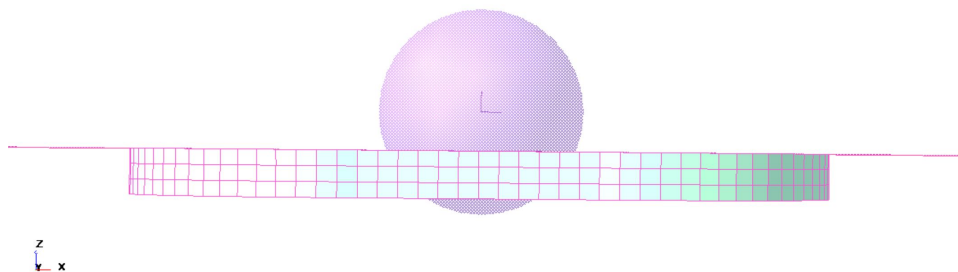
Table 3.1.3: Discretization of the wave frequencies ω and the wave angles θ used in the hydrodynamic analysis.

Variable	Range	Increment	Affected quantities
ω [rad/s]	$[7.5 \cdot 10^{-2}, 4]$	$7.5 \cdot 10^{-2}$	$\mathbf{Q}_r(\omega, \theta), \mathbf{M}_h(\omega), \mathbf{C}_h(\omega)$
θ [°]	$[0, 350]$	10	$\mathbf{Q}_r(\omega, \theta)$

Only the submerged part of the pontoon is modelled and analysed. This is the preferred practice of hydrodynamic modelling as the part above the waterline will only complicate the modelling and not have any impact on the requested outputs. Figure 3.1.2 shows the submerged part of the pontoon where the pink plane represents the water surface and the red sphere is the augmented mass of the pontoon placed at the centre of gravity.



(a) Top view.



(b) Side view.

Figure 3.1.2: Pontoon model. Only the submerged part of the pontoon is modelled. The augmented mass is placed at the centre of gravity.

The hydrodynamic properties extracted from the WADAM-analysis are presented in Table 3.1.4.

Table 3.1.4: Output from the WADAM-analysis.

Properties	Description	Dimension
M_0	Static mass matrix (inertia of pontoon)	6×6
K_0	Restoring stiffness matrix	6×6
M_h	Hydrodynamic mass matrix	6×6
C_h	Hydrodynamic damping matrix	6×6
θ	Wave heading angle	1×35
ω	Frequency axis	1×54
Q_r	Hydrodynamic transfer function	$6 \times 35 \times 54$

The dimensions of the mass, stiffness and damping matrices reflect the number of DOFs

used to describe the displacement of a pontoon. These six DOFs included three translational and three rotational movements as illustrated in Figure 3.1.3.

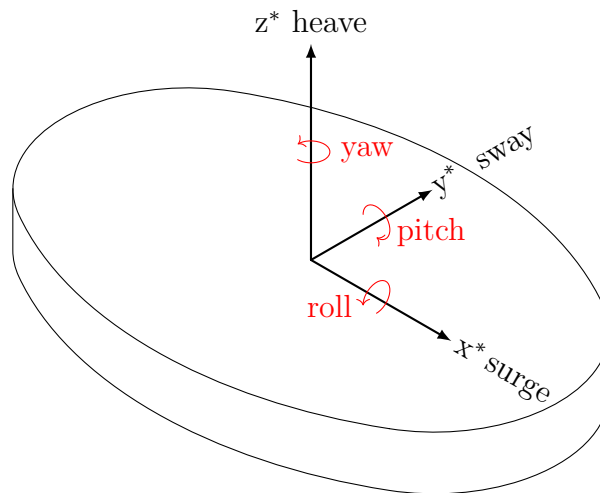
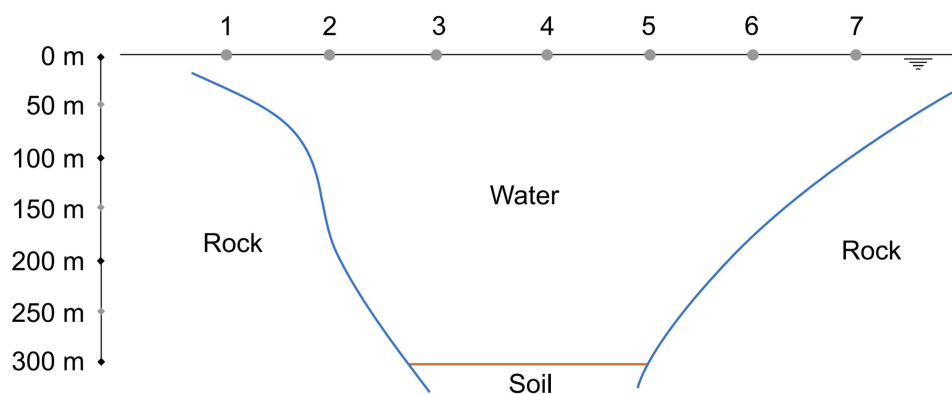
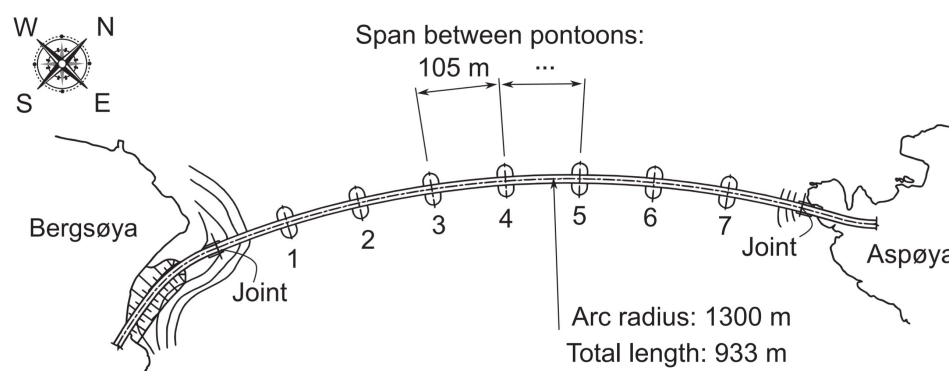


Figure 3.1.3: Illustration of pontoon movements. The axes represent the local coordinate system for the pontoon. The translational DOFs are indicated in black while red represents the rotational DOFs.

In the model the water depth is set to 300 meters to simulate deep-water conditions. Figure 3.1.4(a) shows the water depth profile across the strait, while Figure 3.1.4(b) shows the pontoon arrangement for the bridge. The pontoon numbering is shown in both figures.



(a) Water depth profile across the strait.



(b) Overhead view of the Bergsøysund Bridge.

Figure 3.1.4: Water depth profile and bridge overview (Kvåle et al., 2016).

3.1.3 Full Bridge Model

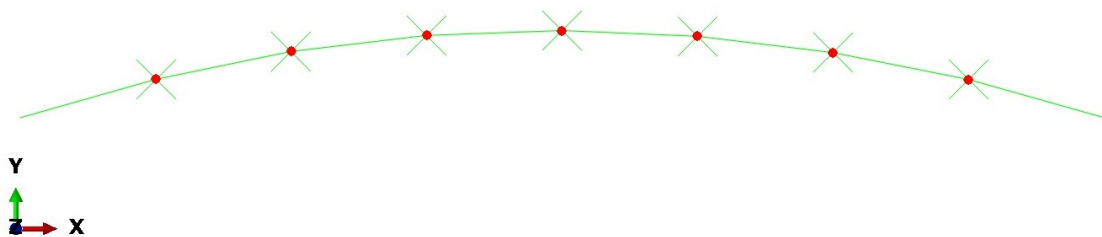
The geometry of the pontoons is not included in the final finite element model in Abaqus but is rather evaluated as nodes. In order to construct a full model of the bridge the hydrostatic properties of the pontoons from the WADAM-analysis, which include pontoon inertia and restoring stiffness, are introduced at these nodes. These properties are first transformed to the global coordinate system such that the local x-axis of the pontoon is perpendicular to the tangent of the bridge arch at each node. This angle transformation had to take place prior to the actual finite element analysis as the local coordinate system is not generated beforehand. The following Abaqus command is used to introduce the pontoon properties to the rest of the finite element model:

```
*USER ELEMENT, LINEAR, NODES = 'NODE NUMBER', UNSYM, TYPE='NAME',
1,2,3,4,5,6
```

The keyword `*USER ELEMENT` is used to introduce a linear element using the additional

command `LINEAR`. The keyword `UNSYM` indicates that the element matrix is not symmetric so that Abaqus can initiate its asymmetric equation solving capability. `*MATRIX, TYPE=STIFFNESS` or `*MATRIX, TYPE=MASS` is used to specify which element matrix the property is to be assigned to. The numbers 1 to 6 represent the six considered DOFs.

From this Abaqus analysis the global mass and stiffness matrices as well as the natural frequencies and the modal vectors for the bridge are obtained. Figure 3.1.5(a) and 3.1.5(b) show the top and side view of the bridge model, respectively. In Figure 3.1.5(a) the nodes at which the pontoon properties are included are indicated in red. The orange dots at both ends of the bridge model in Figure 3.1.5(b) represent the pinned boundary connections to the shore.



(a) Top view of the bridge model.



(b) Side view of the bridge model.

Figure 3.1.5: Top and side view of the bridge model.

Short and stiff beam elements are used to connect the main bridge beam elements to the pontoon nodes. These connectors extend vertically between each pontoon node and the nodes of each main bridge element. The connectors have a height of 4.72 meters. The cross-sectional parameters used for these connectors are idealized. The values from Table 3.1.1 are multiplied by a factor of 1000 in order to simulate rigid elements. Figure 3.1.6 shows these connectors relative to the main bridge elements and the

pontoon nodes.



Figure 3.1.6: Side view of the bridge model at the mid-span.

3.2 Response Spectrum Calculation Structure

As already indicated the computational model can be divided into two submodels. One of these submodels is a finite element model which takes the structural and inertial contributions into account. The second submodel is a hydrodynamic model which handles the hydrodynamic aspects. This approach is based on the work of Kvåle et al. (2016) and more or less follows the same modelling procedure. The structural model is referred to as substructure I, while the hydrodynamic model is referred to as substructure II.

The mass and stiffness matrices defining the structural system are extracted from the structural submodel. Here the inertia contributions from the pontoons are also included, in addition to the frequency-independent buoyancy. The latter is adding stiffness to the model. This stiffness is added discretely for each pontoon and therefore needs to be transformed to a global coordinate system and added. By doing this the different orientation of each pontoon is taken care of. A modal analysis is now performed on the model yielding the natural frequencies and modes. These modal quantities are used to establish the modal system matrices. The modal mass and stiffness matrices are denoted $\tilde{\mathbf{M}}^I$ and $\tilde{\mathbf{K}}^I$, respectively. The corresponding modal damping matrix $\tilde{\mathbf{C}}^I$ can now be established by assuming Rayleigh damping:

$$\tilde{\mathbf{C}}^I = \alpha \tilde{\mathbf{M}}^I + \beta \tilde{\mathbf{K}}^I \quad (3.2.1)$$

The mass and stiffness proportionality factors α and β are both assumed to be equal to $5 \cdot 10^{-3}$ throughout this thesis.

For the simplified model considered in this thesis all seven pontoons are assumed to be equal. The only thing that separates them is their orientations relative to the global coordinate system, as mentioned earlier. In order to form the total contributions to the mass and damping of the model the matrices for each pontoon is transformed into global coordinates and summed. The resulting total matrices are now made modal by use of the modal transformation matrix resulting from the modal analysis described above. The two substructures can now be joined to form the complete bridge model. These global modal matrices are used to form the modal frequency response function given in Equation (2.10.8).

Based on chosen models for the one-dimensional wave spectral density and the spreading function the load model can now be established. In this thesis the one-parameter Pierson-Moskowitz spectrum are chosen for the one-dimensional wave spectral density while the spreading function are modelled using the cos-2s distribution, both described in Section 2.9. From these, the hydrodynamic transfer function $\mathbf{Q}_r(\omega, \theta)$ is established. In order to find the cross-spectral density matrix corresponding to the wave excitation between two selected points along the bridge the integral in Equation (2.10.12) is calculated for all combinations of the pontoons.

Each of the matrices produced from Equation (2.10.12) are stacked to form a total load spectral density matrix. This matrix $\mathbf{S}_p(\omega)$ is then transformed into the modal space defined by the mode vectors established for substructure I. This load spectral density matrix can now be used to establish the displacement spectral densities $\mathbf{S}_u(\omega)$ by use of the power spectral density method defined by Equation (2.10.13). As a final step, the response spectral density matrix is transformed from modal to physical coordinates.

The complete calculation setup for the bridge modelling are summarized in the flowchart in Figure 3.2.1:

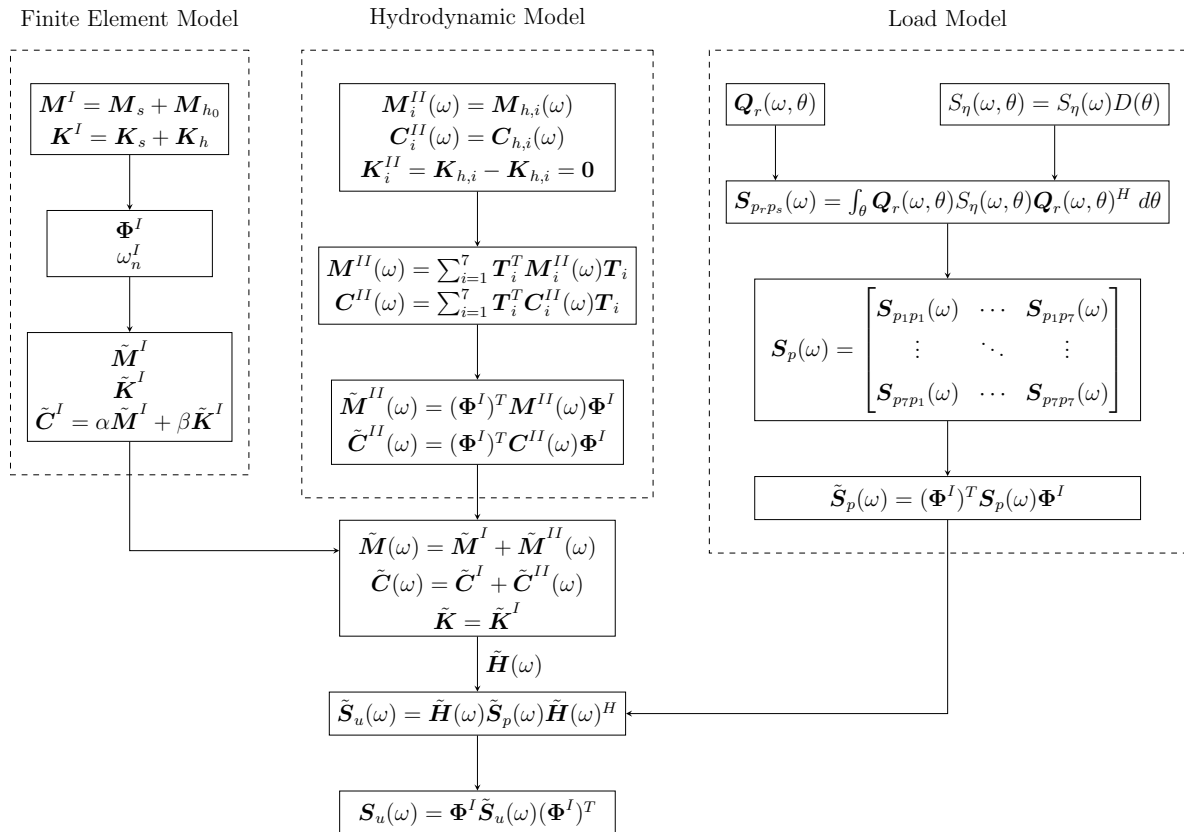


Figure 3.2.1: Flowchart for the calculation setup. Based on the work of Kvåle et al. (2016).

3.3 Software

In this section the software used in this project are presented and discussed. This include both single scripts written in MATLAB and Python, as well as analytical third-party programs.

3.3.1 The WAWI-Toolbox

The WAWI-toolbox is provided by the Structural Dynamics Group at the Department of Structural Engineering at NTNU with Knut Andreas Kvåle being the main contributor. The toolbox contains several MATLAB scripts needed to establish the dynamical load model presented in the flowchart in Figure 3.2.1. The main scripts included in the toolbox are:

- **importwadam.m**: Fetches the hydrostatic and hydrodynamic system matrices, the frequency and angle vectors as well as the transfer function matrix from the report file generated in the WADAM-analysis.
- **generate_abaqus_input.m**: Takes the hydrostatic mass and stiffness matrix of the pontoons as input and generates an input file for Abaqus containing the stiffness and mass system matrices. This script also performs a rigid rotation transformation of the matrices. The rotation angle is given according to the position of the pontoons in relation to the global coordinate system of the bridge superstructure.
- **cos2s_center.m**: Calculates the cos-2s directional distribution of the waves. This function takes the spreading parameter and wave angles as inputs. The angle of the mean wave direction θ_0 is assumed to be zero. The spreading parameter is set to $s = 13$ which is equivalent to $s = 3$ for $\cos 2s(\theta)$ instead of $\cos 2s(\theta/2)$. This short-crested sea condition is claimed to be the most realistic according to on-site observations (Kvåle et al., 2016).
- **pmjons2.m**: Calculates the one-dimensional wave spectral density based on the JONSWAP spectrum. The inputs are the environmental parameters (significant wave height and zero-crossing period), wave frequency and a peakedness factor which is set equal to 2.05.

- **waveaction.m**: Estimates the wave excitation cross-spectral density matrix between two selected points. This corresponds to step 11 in the flowchart in Figure 3.2.1. The main inputs are the hydrodynamic transfer function and the cross-spectral density of the water elevation given by steps 8 and 9 in the flowchart, respectively. Furthermore, the Cartesian coordinates of the pontoons are given along with the angles of the pontoons and the water depth. The latter is here set equal to infinity.

3.3.2 Analytical third-party programs

- **GenieE**: Software in which the pontoon model is generated as a rigid body containing the correct geometries of the outer shell. Here the pontoon model is meshed with a maximum mesh width of 1 meter. Finally, the model is exported as a finite element model. This program is developed by DNV.
- **HydroD**: This program takes in the finite element shell model generated in GenieE and carries out the hydrodynamic analysis using the built-in engine WADAM. WADAM generates a report file containing the results of this analysis. Besides the FEM-file, the user defines the discretization of the wave angle and frequency, the submergence depth and the water properties, among other hydrodynamically relevant properties. This program is also developed by DNV.
- **Abaqus FEA**: Finite element software used for the modal analysis of the bridge. The outputs of interest are the natural frequencies, the modal vectors and the normalized mass of the bridge. This program is developed by Abaqus Inc.
- **Python**: A programming language used to write the scripts needed to calculate the long-term extreme responses. This program is developed by Python Software Foundation.
- **MATLAB**: A programming language used to write the WAWI-toolbox as well as the script which combines the results from the finite element model, the hydrodynamic model and the load model in order to calculate the response spectrum and the corresponding moments for the pontoon and DOF of interest. This program is developed by MathWorks.

3.4 Modal Analysis in Abaqus

The theory behind the modal analysis conducted in Abaqus is presented in Section 2.3. Abaqus establishes the mass and stiffness matrices of the structure and solves the eigenvalue problem given in Equation (2.3.5). The mode shapes obtained from this analysis are mass normalized by default, see Equation (2.3.6). Furthermore, the number of required eigenvalues is provided by the user which in this thesis is set to 42.

3.4.1 Natural Frequencies and Modes

The first ten undamped natural frequencies along with their periods and mode types obtained from the modal analysis of the simplified finite element model are given in Table 3.4.1. The direction in which the bridge would sway in each mode is also identified by visual inspection of the deformation plots generated in Abaqus. For further confirmation of these mode types, the effective modal mass is also studied. This effective modal mass has units of mass and its summation over all modes equals the total mass of the structure. The quantity indicates the amount of mass that responds in a particular mode of vibration (Williams, 2016).

Table 3.4.1: Natural frequencies and periods along with the mode types of the 10 first modes from Abaqus.

Mode number	Mode type	Natural frequency		Natural period
		[Hz]	[rad/s]	
1	Horizontal	0.096	0.605	10.380
2	Torsional	0.185	1.160	5.414
3	Horizontal	0.207	1.299	4.836
4	Vertical	0.269	1.691	3.715
5	Vertical	0.276	1.736	3.619
6	Vertical	0.311	1.955	3.214
7	Horizontal	0.323	2.027	3.100
8	Combined	0.387	2.431	2.584
9	Combined	0.397	2.493	2.521
10	Vertical	0.525	3.297	1.906

Figure 3.4.1 (a) through (v) show the base state of the bridge along with the mode types presented in Table 3.4.1 seen from both above and from the side. The eigenvectors obtained from this modal analysis are used to establish the modal mass, stiffness and damping matrices as well as transforming the load spectral density matrix to the modal space and transforming the response spectral density from modal into physical DOFs as illustrated in Figure 3.2.1.

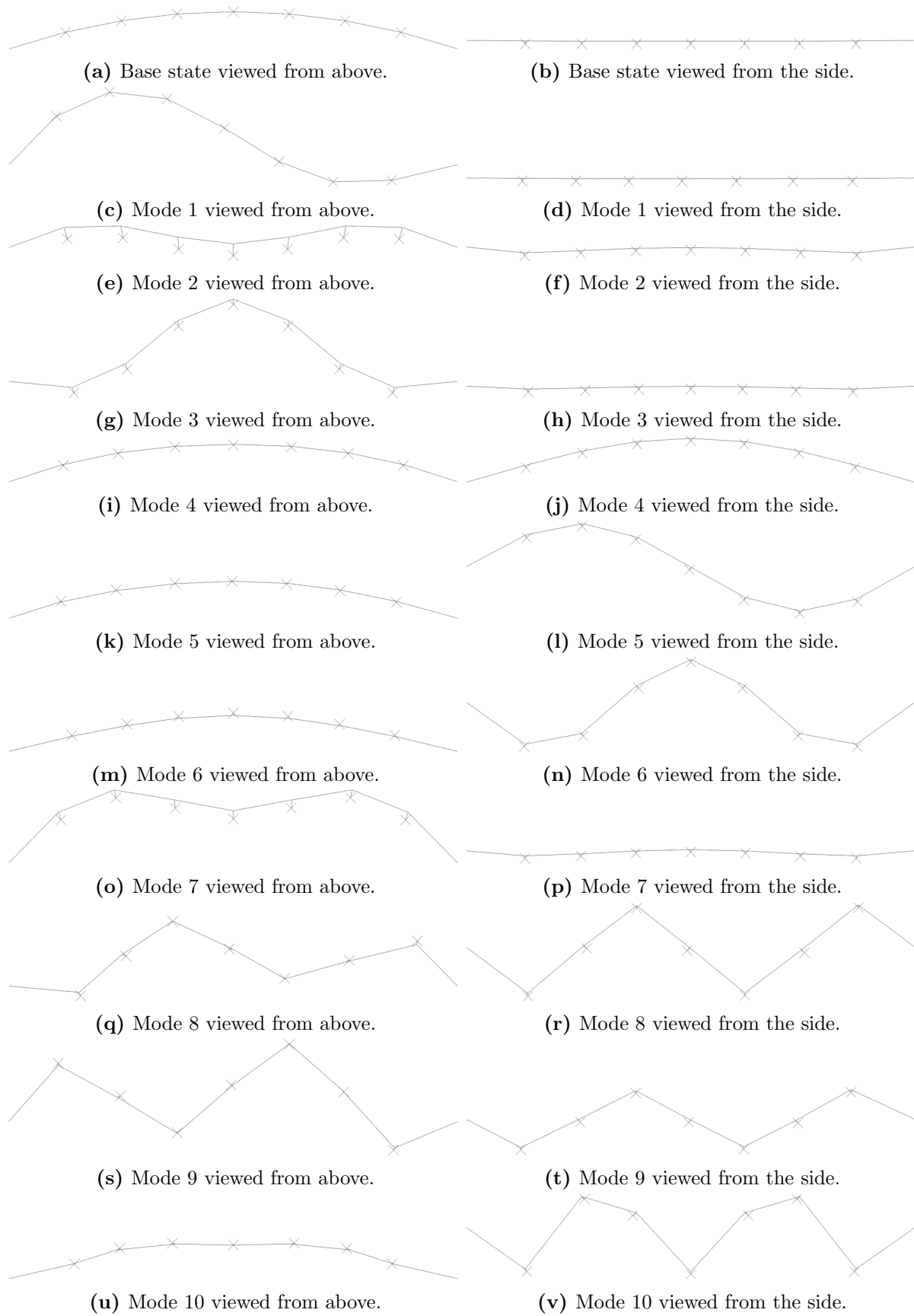


Figure 3.4.1: Base state and mode shapes for the Abaqus model.

3.5 Extreme Response Calculations

The horizontal transverse displacement of pontoon number 4 in Figure 3.1.4 (b) is studied in particular. This specific displacement corresponds to the second degree-of-freedom, which is translation along the local x-axis of the pontoon as illustrated in Figure 3.1.3. In the following this displacement is what will be referred to as the *response*. Furthermore, the characteristic responses are calculated for return periods of $M = 10, 100, 1000$ years. These choices for M are assumed to be sufficient in demonstrating the extreme situations with acceptable spaced intervals. The long-term extreme response calculation methods for which the methodology is presented in this chapter are listed below:

- Full Integration
- Inverse First-Order Reliability Method (IFORM)
- Environmental Contour Method (ECM)
- Importance Sampled Monte Carlo Simulation (ISMCS)
- Gaussian Process Regression (GPR)

3.5.1 Environmental Model Parameters

As stated in Section 2.8 the environmental model is described using two parameters, the significant wave height H_s and the zero-crossing period T_z with their units in meters and seconds, respectively. The distribution functions for these environmental parameters are the Weibull distribution, see Equation (2.8.2), and a conditional lognormal distribution, see Equation (2.8.5). The distribution parameters used are presented in Table 3.5.1. Usually, these parameters are fitted to measured data. However, in this thesis the values correspond to the ones presented in Finn-Idar Grøtta Giske's doctoral thesis (Giske, 2017), which are assumed to be representative for sea states at the northwestern part of Norway.

Table 3.5.1: Distribution parameters used for the Weibull and lognormal distributions.

Weibull		Lognormal					
α	β	a_0	a_1	a_2	b_0	b_1	b_2
1.76	1.59	0.70	0.282	0.167	0.07	0.3449	-0.2073

3.5.2 Full Integration

The expressions for the long-term extreme response based on the short-term extreme response and short-term upcrossing rate in Equation (2.7.6) and (2.7.10), respectively, are solved in an approximate manner. Analytic integration over the environmental parameters can not be conducted and the calculation is rather performed numerically by choosing discrete values for the environmental parameters. To ensure inclusion of environmental parameters with significant contribution to the integrand, the joint probability density function of the environmental parameters is integrated numerically and the limits for the environmental parameters as well as their step sizes are adjusted in order to achieve:

$$\int_{\mathbf{w}} f_{\mathbf{w}}(\mathbf{w}) d\mathbf{w} = 1 \quad (3.5.1)$$

A matrix of moments is calculated using Equation (2.5.8) with the environmental parameters as presented in Table 3.5.2. Furthermore, a contour plot of the zeroth and second order moments can be seen in Figure 3.5.1.

Table 3.5.2: Data used for the environmental parameters. This includes the lower and upper limit for the parameters as well as the corresponding area under their joint probability density function.

Environmental parameter	Lower limit	Upper limit	Number of elements	Area under joint PDF
h	0.001	9	655	0.999905
t	0.001	12.5	150	

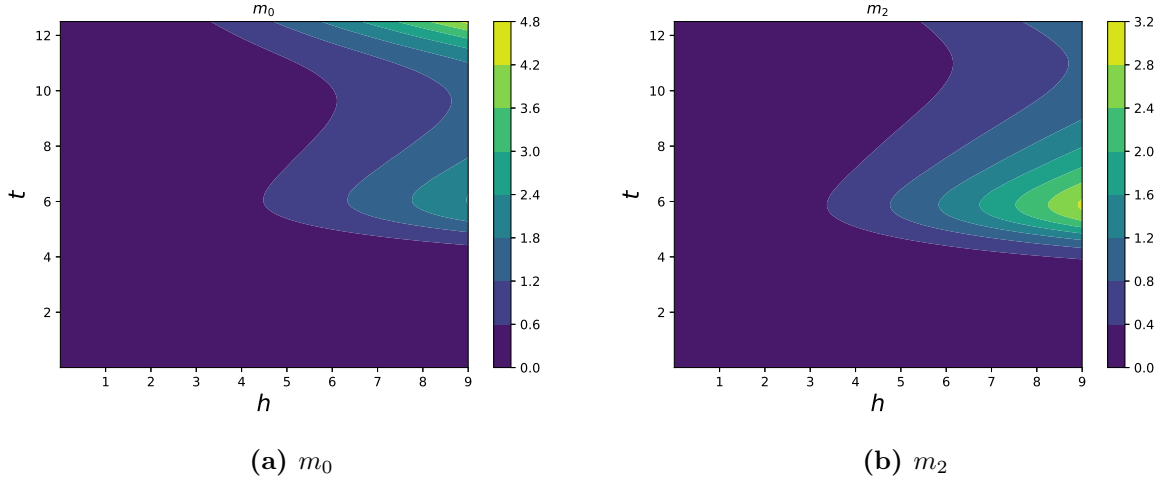


Figure 3.5.1: Zeroth and second order moments for DOF 2 at pontoon 4.

The cumulative distribution function for the long-term extreme response is plotted as the expressions in Equation (2.7.3) (2.7.6), (2.7.7) and (2.7.10) are solved numerically by use of the trapezoidal rule for threshold response values of 0 to 5 meters and with environmental parameters as defined in Table 3.5.2. The characteristic response is then found by utilizing the expression for the exceedance probability in Equation (2.7.13).

3.5.3 IFORM

The first step when performing the long-term extreme response analysis using IFORM is to formulate the vector $\mathbf{V} = [\mathbf{W}, V_3] = [H_s, T_z, V_3]$. This vector contains the environmental parameters and the response value in U-space after transformation using the Rosenblatt transformation as described in Section 2.11. Given a point in this standard normal space, $\mathbf{u} = [u_1, u_2, u_3]$, the corresponding components of the vector $\mathbf{v} = [h(\mathbf{u}), t(\mathbf{u}), v_3(\mathbf{u})]$ in the physical space are calculated as (Giske, 2017):

$$h(\mathbf{u}) = F_{H_s}^{-1}(\Phi(u_1)) = \alpha[-\ln(1 - \Phi(u_1))]^{\frac{1}{\beta}} \quad (3.5.2a)$$

$$t(\mathbf{u}) = F_{T_z|H_s}^{-1}(\Phi(u_2)|h(\mathbf{u})) = \exp\{\mu(h(\mathbf{u})) + \sigma(h(\mathbf{u}))u_2\} \quad (3.5.2b)$$

$$v_3(\mathbf{u}) = F_{V_3|H_s, T_z}^{-1}(\Phi(u_3)|h(\mathbf{u}), t(\mathbf{u})) \quad (3.5.2c)$$

Here $v_3(\mathbf{u})$ is expressed in terms of the exact (y) and the approximate (\tilde{r}) formulations of the short-term extreme response given in Equation (2.7.6) and (2.7.7), respectively. This

yields:

$$v_3(\mathbf{u}) = y(\mathbf{u}) = \sqrt{-2m_0(h(\mathbf{u}), t(\mathbf{u})) \ln \left(-\frac{2\pi}{\tilde{T}} \sqrt{\frac{m_0(h(\mathbf{u}), t(\mathbf{u}))}{m_2(h(\mathbf{u}), t(\mathbf{u}))}} \right) \ln \Phi(u_3)} \quad (3.5.3a)$$

$$v_3(\mathbf{u}) = \tilde{r}(\mathbf{u}) = \sqrt{2m_0(h(\mathbf{u}), t(\mathbf{u})) \ln \left(-\frac{2\pi}{\tilde{T}} \sqrt{\frac{m_0(h(\mathbf{u}), t(\mathbf{u}))}{m_2(h(\mathbf{u}), t(\mathbf{u}))}} \right) (1 - \Phi(u_3))} \quad (3.5.3b)$$

The long-term extreme response is calculated for return periods of 10, 100 and 1000 years. Table 3.5.3 shows the corresponding reliability index β calculated according to Equation (2.11.17).

Table 3.5.3: Reliability indexes β_M corresponding to the different return periods M .

M	10	100	1000
β_M	3.98	4.49	4.97

The implementation of the IFORM-algorithm is carried out using Python. The tolerance for convergence of the design point \mathbf{u}^* according to Equation (2.11.23) is set to 10^{-3} . For more stable iterations the implemented algorithm included the backtracking approach proposed by Giske et al. (2017). Here the proportionality constant is chosen as $c = 10^{-4}$, see Equation (2.11.21). Numerical differentiation is used to calculate the gradient of $v(\mathbf{u})$. The iteration process is initiated using the initial point $\mathbf{u}_1 = [0, 0, \beta]$.

3.5.4 Environmental Contour Method

The environmental parameters H_s and T_z with occurrence probability corresponding to the contour with return period M is obtained using IFORM. This algorithm is implemented in a similar fashion to what is described in Section 3.5.3. This time, however, the response component is replaced by the joint probability density function for the environmental parameters. The iterated environmental parameters in U-space and the convergence pattern for the different return periods M can be seen in Figure 3.5.2. The M -year equivalent iterated environmental parameters are also presented in Table 3.5.4.

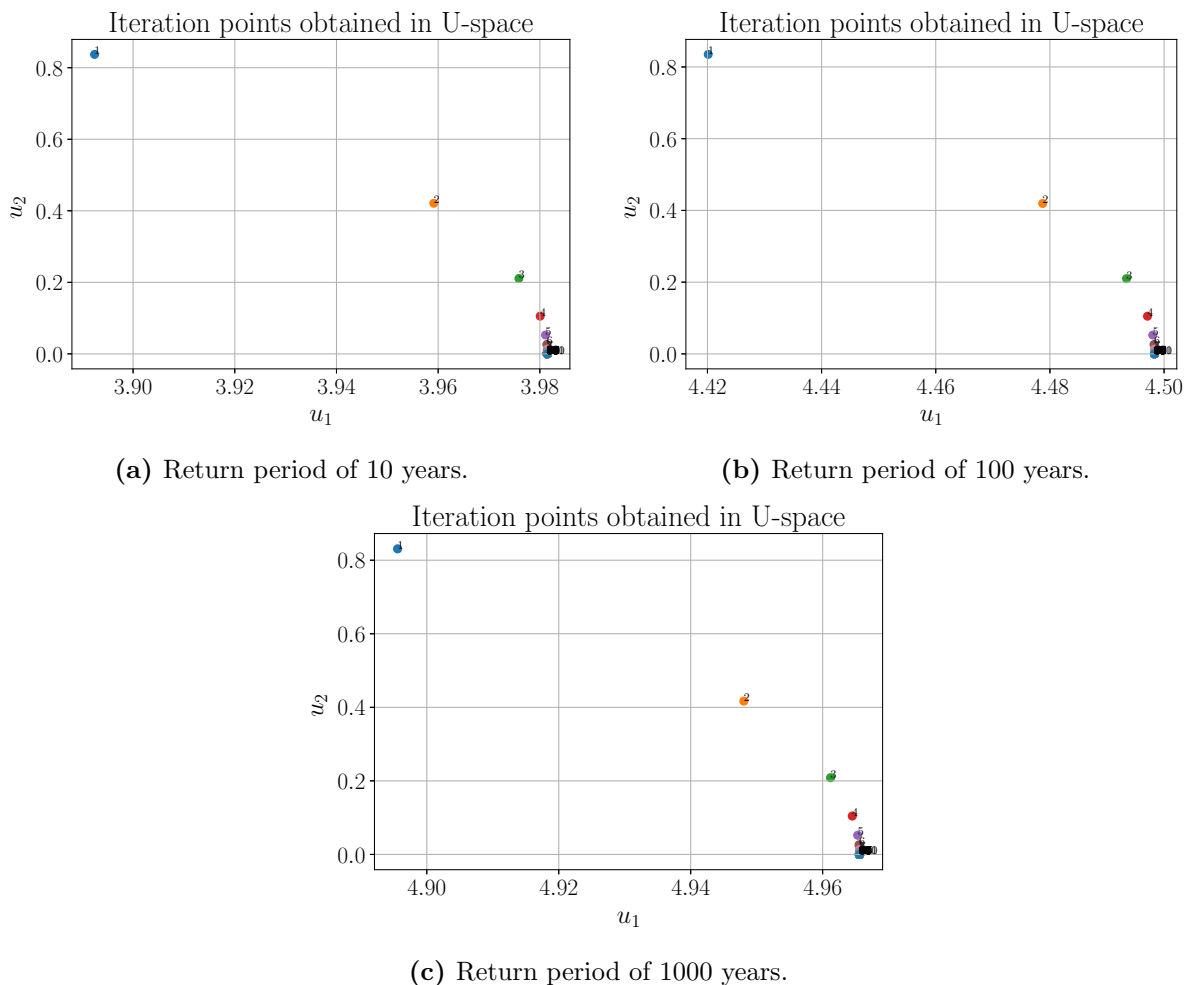


Figure 3.5.2: Iteration pattern for the M -year equivalent environmental parameters.

Table 3.5.4: M -year equivalent iterated environmental parameters.

M -year	U-space [u_1, u_2]	V-space [h, t]	Number of iterated points
10	[3.98, $6.65 \cdot 10^{-31}$]	[7.62, 2.99]	102
100	[4.45, $6.63 \cdot 10^{-31}$]	[8.65, 3.02]	102
1000	[4.97, $6.59 \cdot 10^{-31}$]	[9.62, 3.04]	102

Furthermore, the short-term extreme response is calculated from Equation (2.6.12) for various combinations of h - and t -values along the relevant contour. These contours can be seen in Figure 3.5.3. The combination of h and t which results in the highest response value is recognized as the design point.

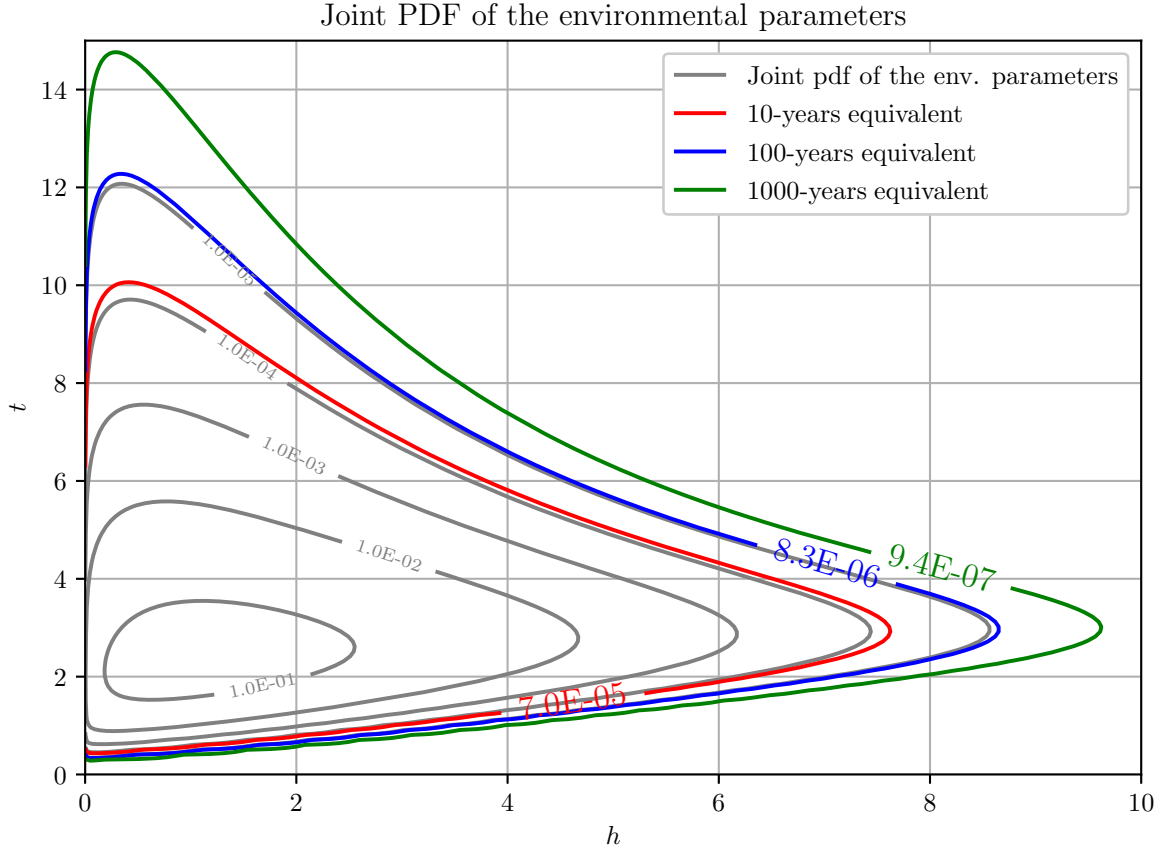


Figure 3.5.3: Joint PDF over the environmental parameters presented by their isoprobability contour lines.

3.5.5 IFORM and ISMCS

The environmental parameters are sampled from their joint PDF given by Equation (2.6.5) and the integrand in Equation (2.14.1) is calculated in a recursive manner using Python. The characteristic M -year response is then identified according to Equation (2.7.14). The number of samples for such a simulation is usually high. However, in order to achieve a sufficiently accurate results within reasonable computational expenses, the integrand is weighted such that it is biased towards known design points. In this thesis the design points from IFORM are used. The following Importance Sampling function was used for the Importance Sampled Monte Carlo Simulation:

$$h_{\mathbf{w}}(\mathbf{w}) = \prod_{i=1}^n \frac{1}{\sigma_i} \Phi\left(\frac{\mathbf{w}_i - \mu_i}{\sigma_i}\right) \quad (3.5.4)$$

Here the importance density function $h_{\mathbf{W}}(\mathbf{w})$ is centered on $\mathbf{W} = \mathbf{w}^*$, where $\mathbf{w}^* = [h^*, t^*]$ represents the design points obtained from IFORM. Furthermore, $\mu_i = \mathbf{w}_i^*$ and $\Phi(\cdot)$ represent the mean value and standard normal cumulative distribution function, respectively. $f_{\mathbf{W}}(\mathbf{w})$ is the joint PDF over the environmental parameters. The standard deviation σ_i is set in the range of 0.15 - 0.3 times the standard deviation of the marginal distributions over the environmental parameters. Given that the environmental parameters are sampled in a biased manner, the number of samples is reduced to $N_m = 50$.

3.5.6 Gaussian Process Regression

For this method the environmental parameters used as training points for establishing the covariance matrix are randomly generated from the joint PDF, see Equation (2.6.5). $N_s = 8$ random states of the environmental model are drawn as training points. For each state of the environmental parameters the conditional short-term extreme response given by Equation (2.6.10) is solved for different threshold response values, whereas the characteristic M -year response is identified according to the fractile value given in Equation (2.7.13). The training points for the extreme M -year response is then found as: $r_q^M = \{r_1, r_2, \dots, r_{N_s}\}$. Furthermore, the Matérn kernel is used to establish the covariance matrix and is given by:

$$k(x_i, x_j) = \frac{1}{\Gamma(\nu)2^{(\nu-1)}} \left(\frac{\sqrt{2\nu}d(x_i, x_j)}{l} \right)^\nu \kappa_\nu \left(\frac{\sqrt{2\nu}d(x_i, x_j)}{l} \right) \quad (3.5.5)$$

Here $d(x_i, x_j)$ is the Euclidean distance between the points x_i and x_j , $\kappa_\nu(\cdot)$ is a modified Bessel function and $\Gamma(\cdot)$ denotes the gamma function. Compared to the squared exponential kernel described in Section 2.13 the Matérn kernel contains an additional parameter ν . Together with the length scale parameter l , the parameter ν controls the smoothness of the estimated function. The length scale parameter l defined here is the same as the one introduced for the squared exponential kernel (Genton, 2001). In this thesis good results are obtained with the parameters l and ν set to 0.15 and 2.5, respectively. Although the Matérn kernel is the one chosen in this project, it is worth mentioning that this kernel reduces to the squared exponential kernel for $\nu = 0.5$.

CHAPTER 4

Results

In this chapter the results and observations from the study conducted in the project are presented. Effort is made into presenting these results in a short and informative manner, leaving the main discussions and general considerations regarding the validity of these results to the next chapter.

4.1 Long-Term Response Predictions

In the following sections the predicted long-term response values from the investigated methods are presented.

4.1.1 Full Integration

The CDFs for the long-term extreme response obtained from the Full Integration method based on the exact formulation of the short-term upcrossing rate described in Section 2.7.3 for return periods of 10, 100 and 1000 years are shown in Figure 4.1.1, 4.1.2 and 4.1.3, respectively. A horizontal line representing the exceedance probability is also present in these figures.

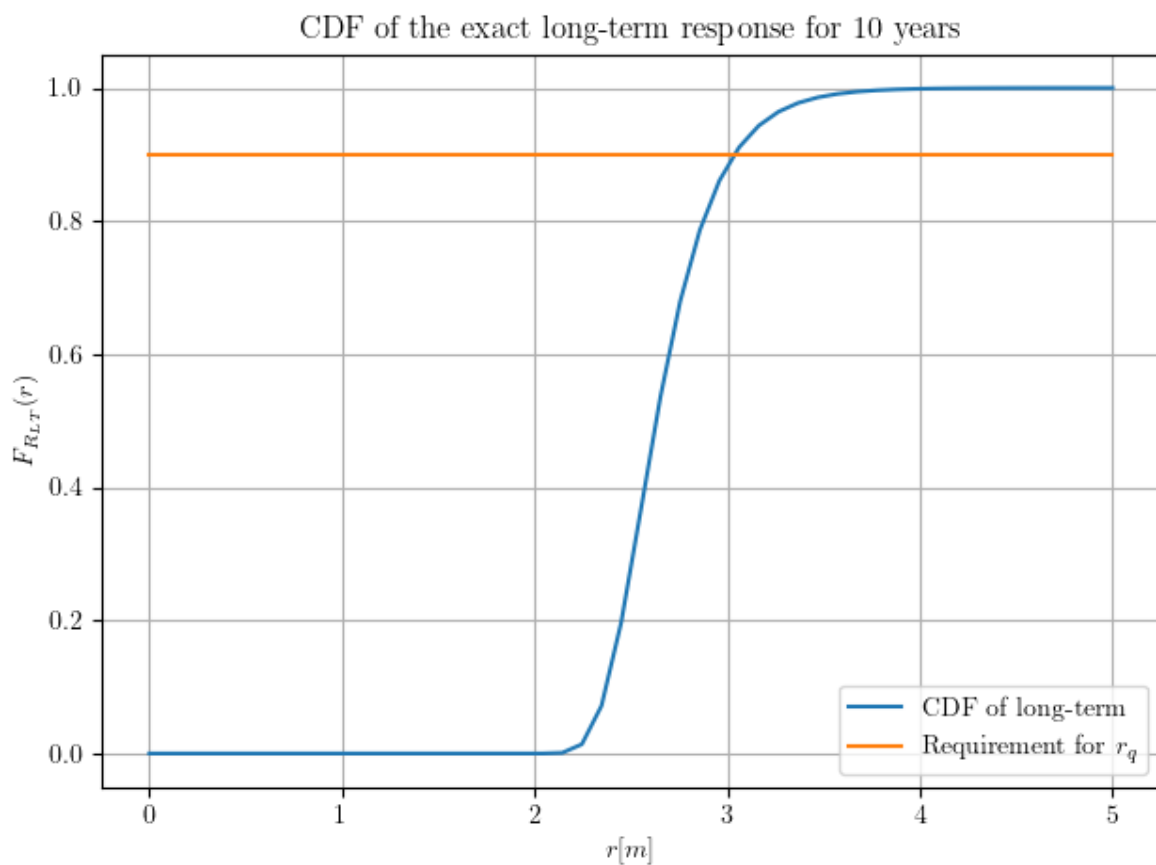


Figure 4.1.1: Exact formulation of the cumulative distribution function based on the short-term upcrossing rate for a return period of 10 years.

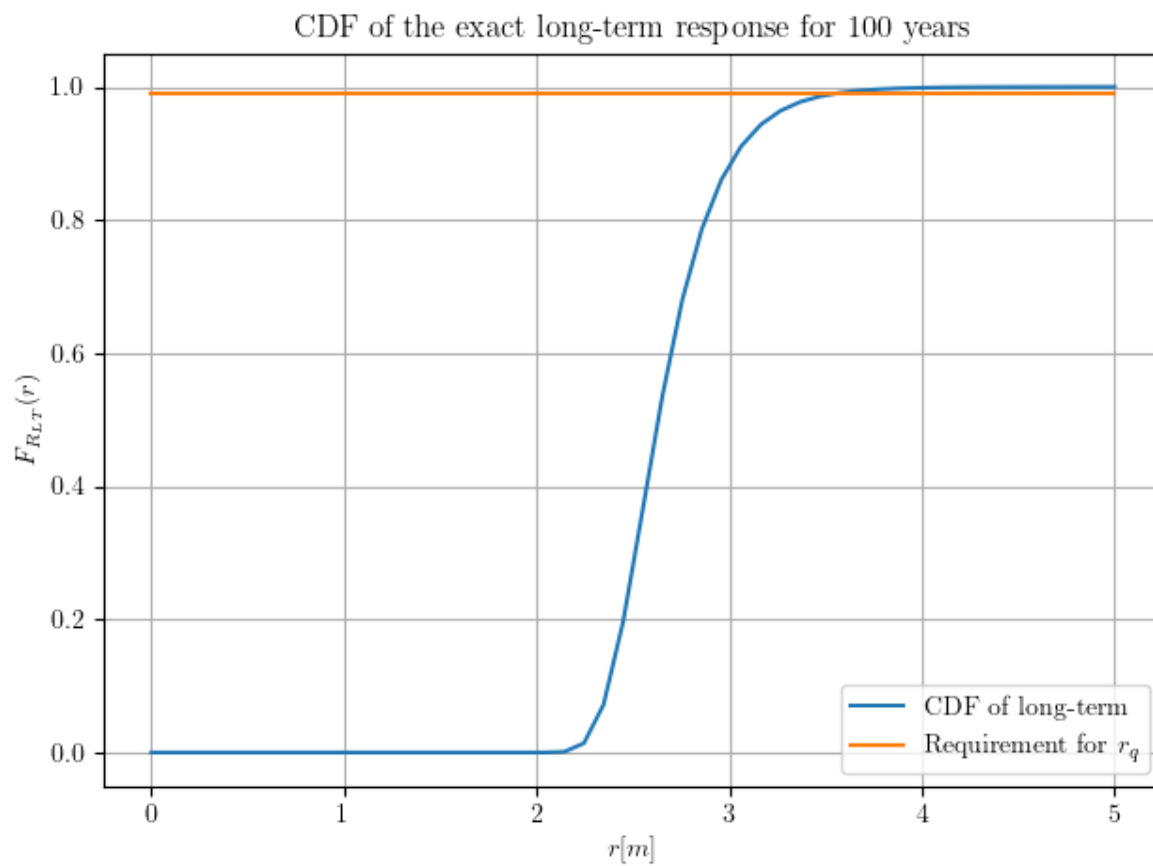


Figure 4.1.2: Exact formulation of the cumulative distribution function based on the short-term upcrossing rate for a return period of 100 years.

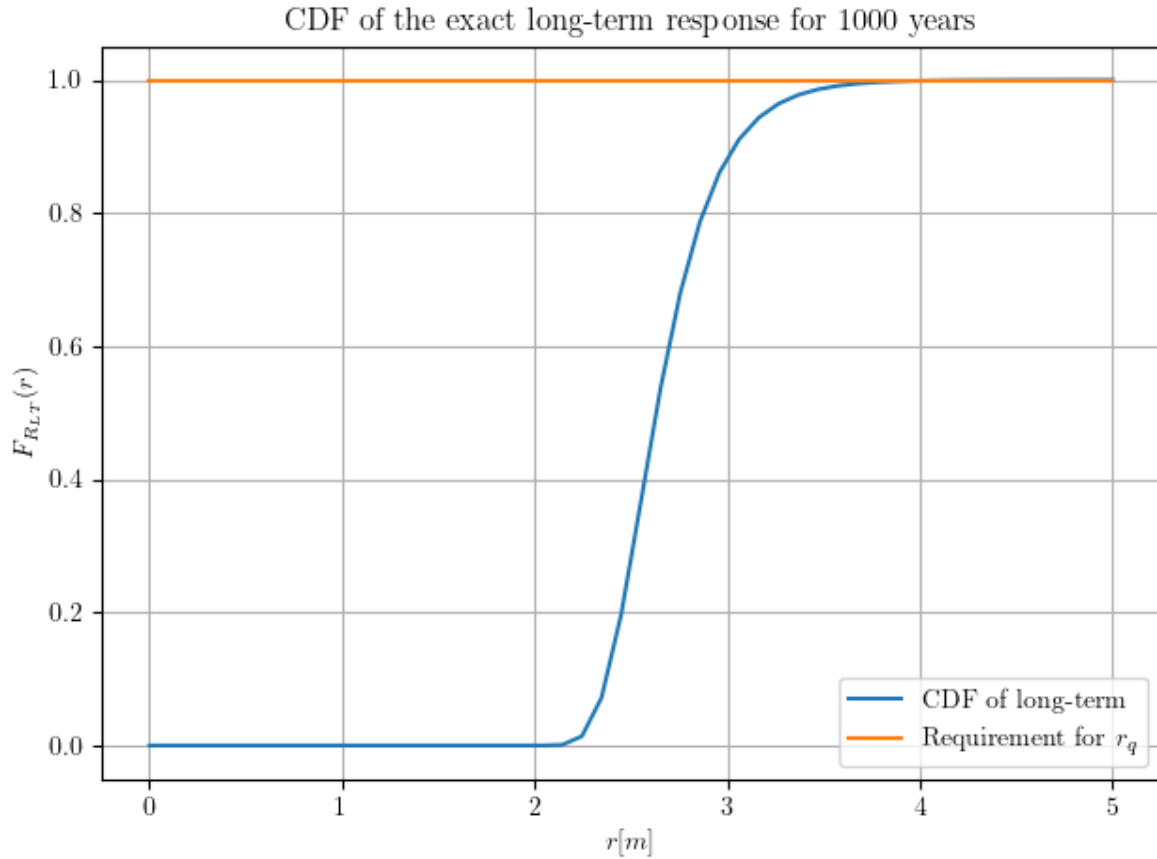


Figure 4.1.3: Exact formulation of the cumulative distribution function based on the short-term upcrossing rate for a return period of 1000 years.

Reading from the plots in Figure 4.1.1, 4.1.2 and 4.1.3 the characteristic response values for the method of Full Integration based on the exact upcrossing rate formulation can be found. These values are summarized in Table 4.1.1:

Table 4.1.1: Response values from the method of Full Integration based on the exact model of the upcrossing rate.

M -year	Characteristic response [m]
10	3.04
100	3.55
1000	4.06

Furthermore, Figure 4.1.4, 4.1.5 and 4.1.6 show plots of the approximate formulation of the cumulative distribution function based on the short-term extreme values:

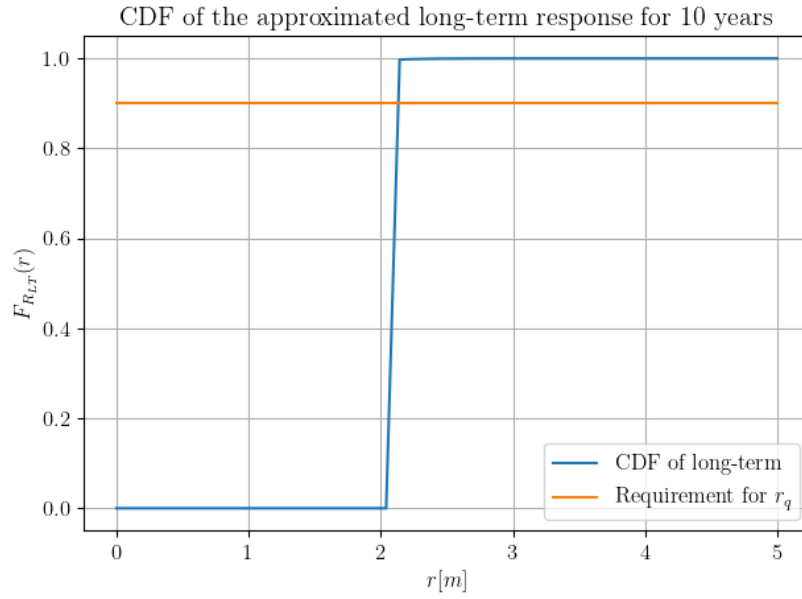


Figure 4.1.4: Approximate formulation of the cumulative distribution function based on the short-term extreme values for a return period of 10 years.

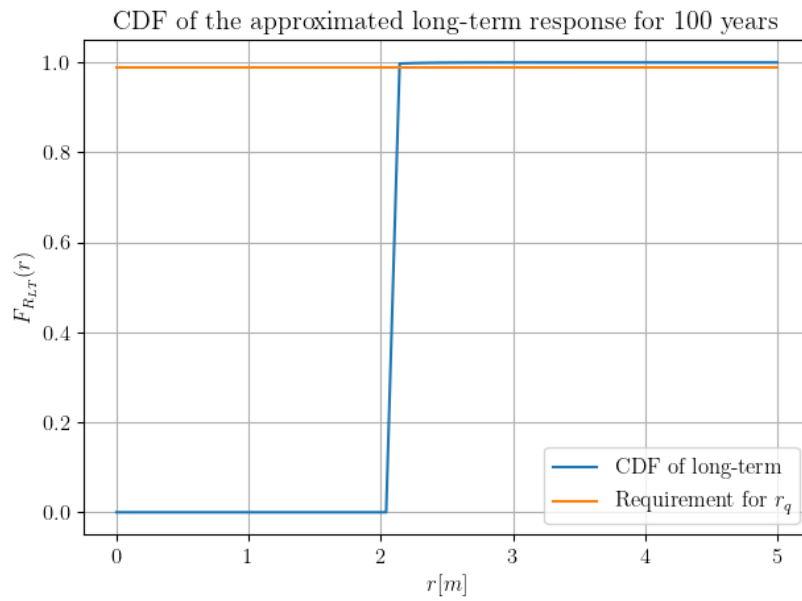


Figure 4.1.5: Approximate formulation of the cumulative distribution function based on the short-term extreme values for a return period of 100 years.

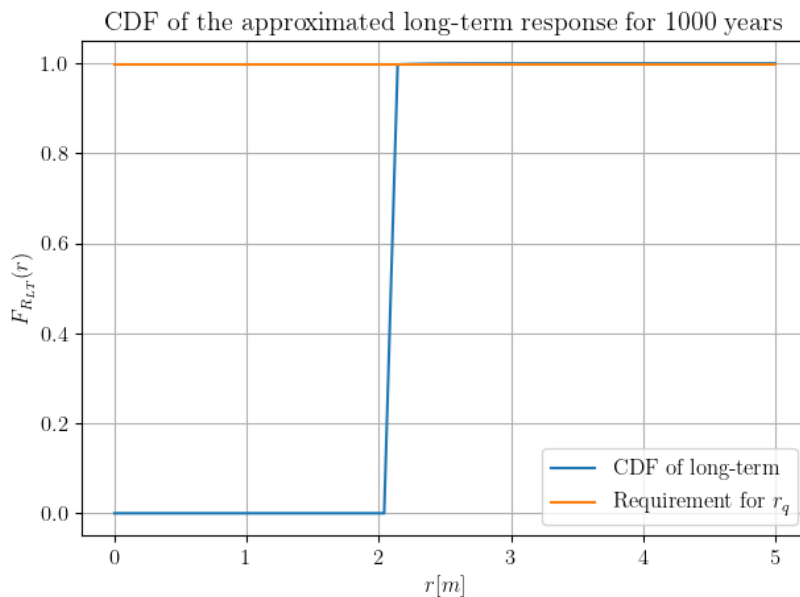


Figure 4.1.6: Approximate formulation of the cumulative distribution function based on the short-term extreme values for a return period of 1000 years.

Table 4.1.2 summarizes the characteristic responses obtained from the formulations of the short-term peaks and the short-term extreme values as described in Section 2.7.1 and 2.7.2:

Table 4.1.2: Response values from the method of Full Integration based on models of the short-term peaks and the short-term extreme values.

<i>M</i> -year	Characteristic response [m]		
	Short-term peaks	Short-term extreme values	
		Exact	Approximate
10	3.04	3.04	2.13
100	3.55	3.55	2.14
1000	4.06	4.06	2.35

For the defined resolutions of h and t (655×150 elements) the elapsed time for calculating the moments m_0 and m_2 for a single DOF as well as for performing the Full Integration are presented in Table 4.1.3. 100 elements of the response threshold r spanning from 0 to 5 meters are used to produce the smooth CDFs in Figure 4.1.1, 4.1.2 and 4.1.3.

Table 4.1.3: Elapsed time for the Full Integration method.

Process	Elapsed time [min]
Moments [m_0, m_2]	2200
Full Integration	275
Total	2475

4.1.2 IFORM

Table 4.1.4 and 4.1.5 contain the long-term extreme responses obtained from IFORM for the exact and approximate formulations, respectively. Parameters that determine the efficiency of the algorithm such as the elapsed time, the number of iterations n_{it} and the number of times the short-term response is calculated n_{st} can be found in these tables. Furthermore, the auto-spectral density of the response, see Equation (2.10.13), which is calculated using the design points obtained from both the exact and approximate formulations are plotted in Figure 4.1.7 and 4.1.8.

Table 4.1.4: Results from IFORM for the exact formulation. r_q , n_{st} and n_{it} denote the characteristic response value, the number of short-term calculations and the number of iterations, respectively.

	Exact				
M -year	Design points [h, t]	r_q	n_{st}	n_{it}	Elapsed time [min]
10	[4.55, 5.52]	3.14	56	10	3.3
100	[5.21, 5.56]	3.73	61	10	3.3
1000	[5.69, 5.58]	4.29	86	15	3.3

Table 4.1.5: Results from IFORM for the approximate formulation. r_q , n_{st} and n_{it} denote the characteristic response value, the number of short-term calculations and the number of iterations, respectively.

	Approximate				
M -year	Design points [h, t]	r_q	n_{st}	n_{it}	Elapsed time [min]
10	[4.56, 5.48]	3.12	35	6	2.7
100	[5.15, 5.54]	3.72	46	8	2.7
1000	[5.72, 5.56]	4.28	58	10	2.7

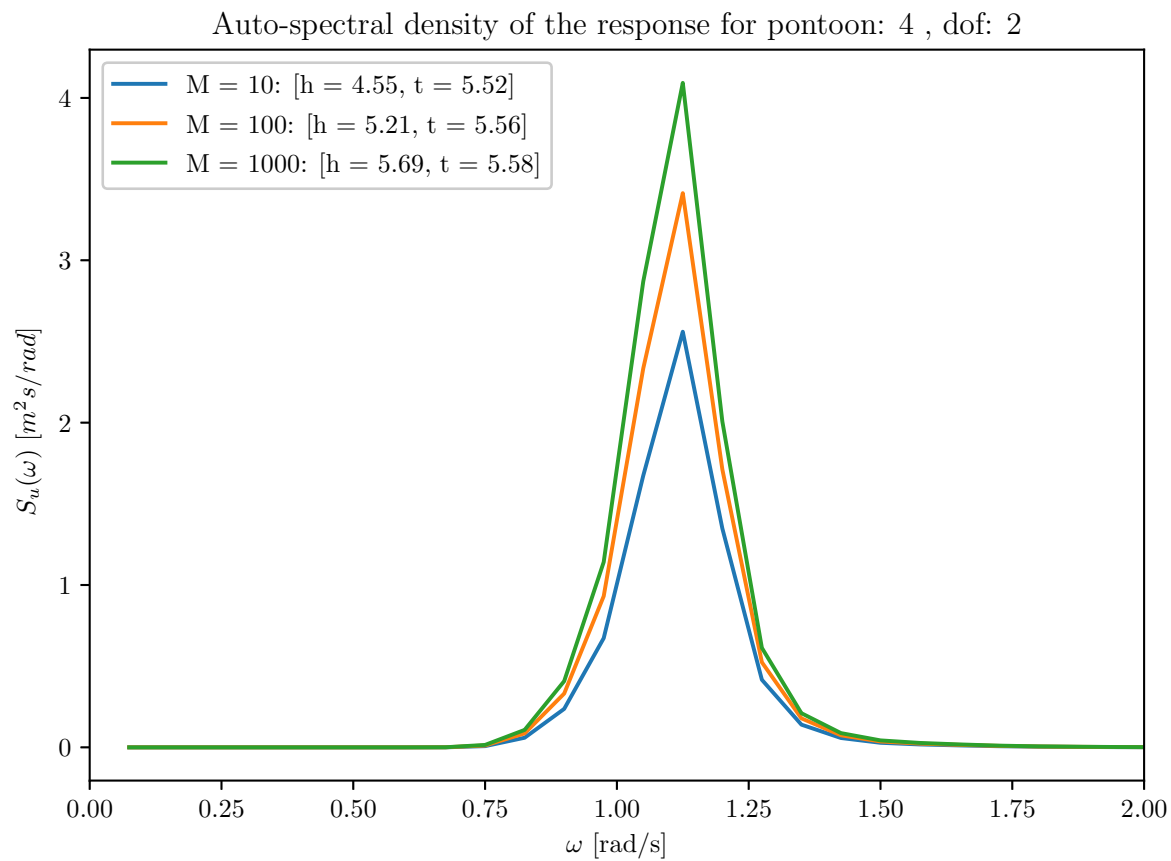


Figure 4.1.7: The response spectrum for pontoon 4, DOF 2 obtained with the design points from the exact IFORM-formulation.

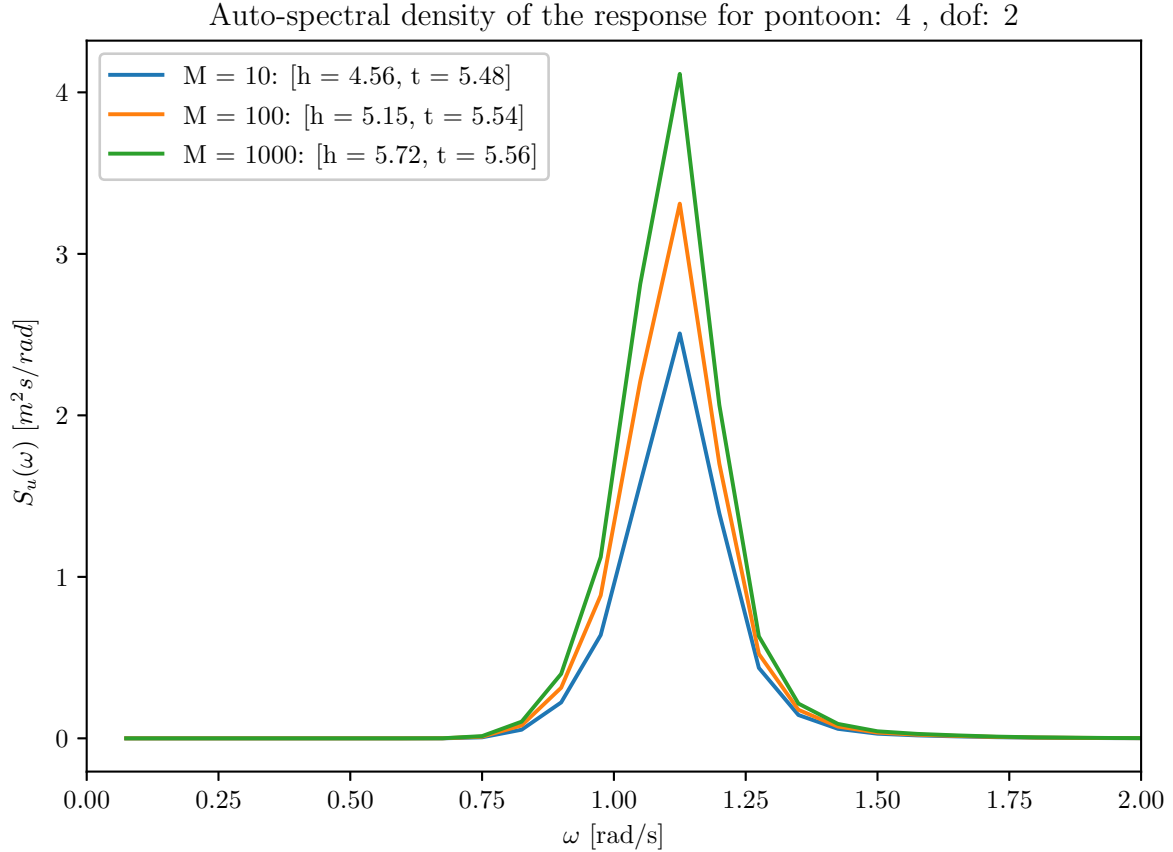


Figure 4.1.8: The response spectrum for pontoon 4, DOF 2 obtained with the design points from the approximate IFORM-formulation.

Figure B.1.1, B.1.2 and B.1.3 in Appendix B.1 show the iterated points in U-space for the exact formulation of IFORM. Likewise, the iterated points for the approximate formulation and the convergence pattern towards the design points can be seen from Figure B.2.1, B.2.2 and B.2.3 in Appendix B.2.

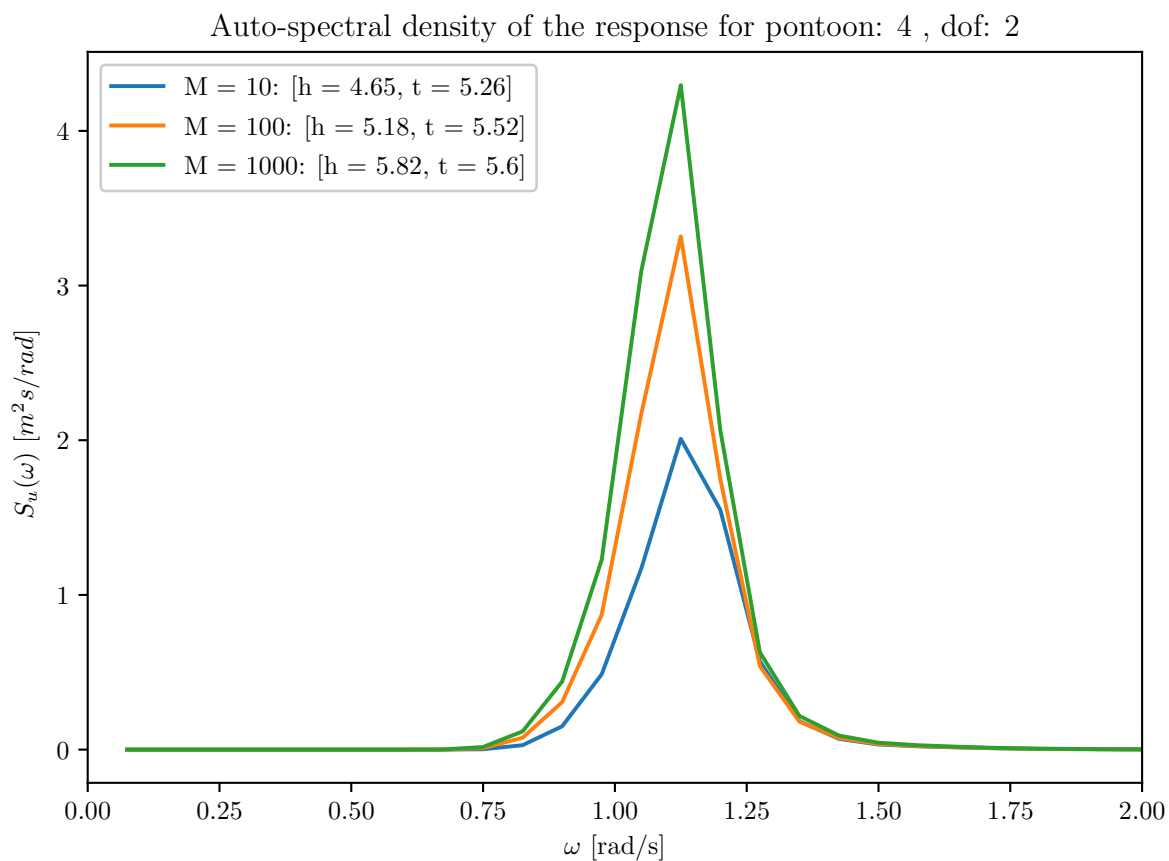
4.1.3 Environmental Contour Method (ECM)

The environmental parameters identified as the design points from ECM are presented in Table 4.1.6 along with the elapsed time for running the algorithm in Python. These sets of points gave the highest response along the M -year equivalent contours, as can be seen from Figure 3.5.3 and Table 3.5.4.

Table 4.1.6: Environmental parameters $[h, t]$ at the design points obtained from ECM.

M -year	Design points in physical space	Elapsed time [min]
10	[4.65, 5.26]	3
100	[5.18, 5.52]	3
1000	[5.82, 5.60]	3

Furthermore, the auto-spectral density of the response as defined in Equation (2.10.13) calculated with the design points obtained for the considered return periods is plotted in Figure 4.1.9:

**Figure 4.1.9:** The response spectrum of pontoon 4, DOF 2 obtained with the design points from ECM.

The cumulative distribution functions for the long-term extreme response for a fractile value of $p = 0.80$ are plotted in Figure 4.1.10, 4.1.11 and 4.1.12 for return periods of 10, 100 and 1000 years.

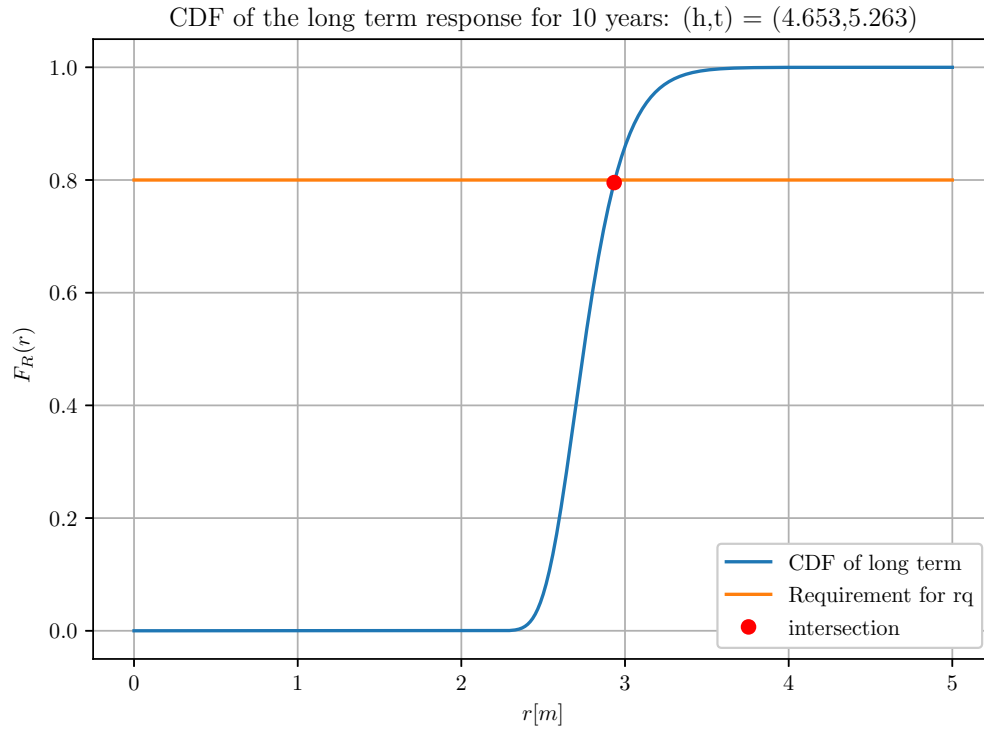


Figure 4.1.10: CDF of the long-term extreme response from ECM for a fractile value of $p = 0.80$ and return period $M = 10$ years.

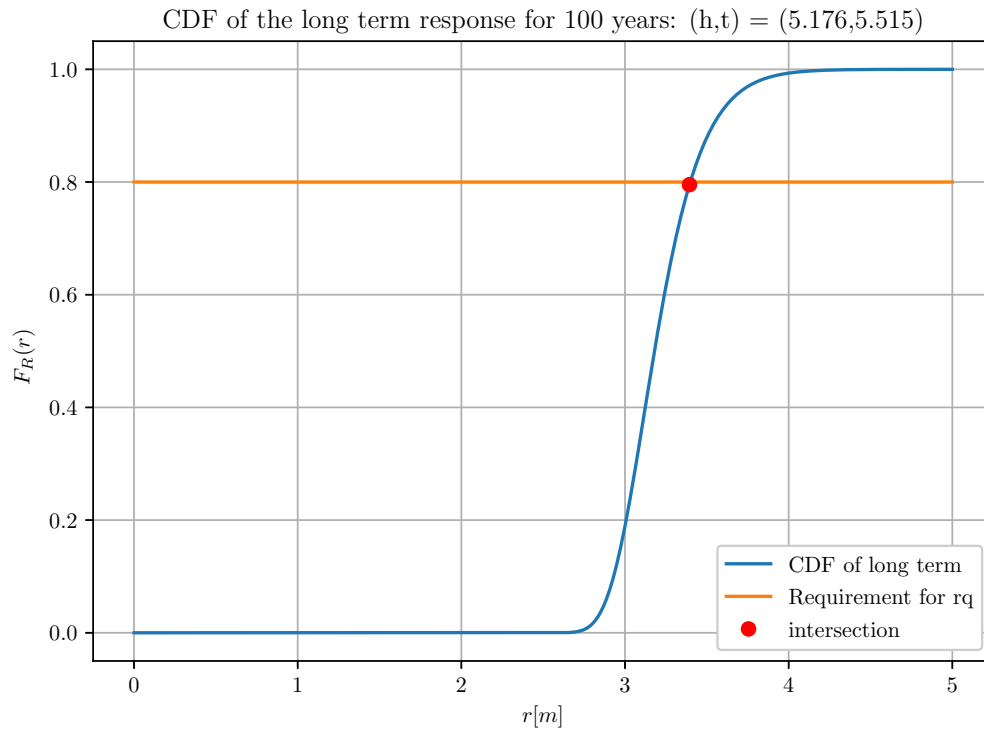


Figure 4.1.11: CDF of the long-term extreme response from ECM for a fractile value of $p = 0.80$ and return period $M = 100$ years.

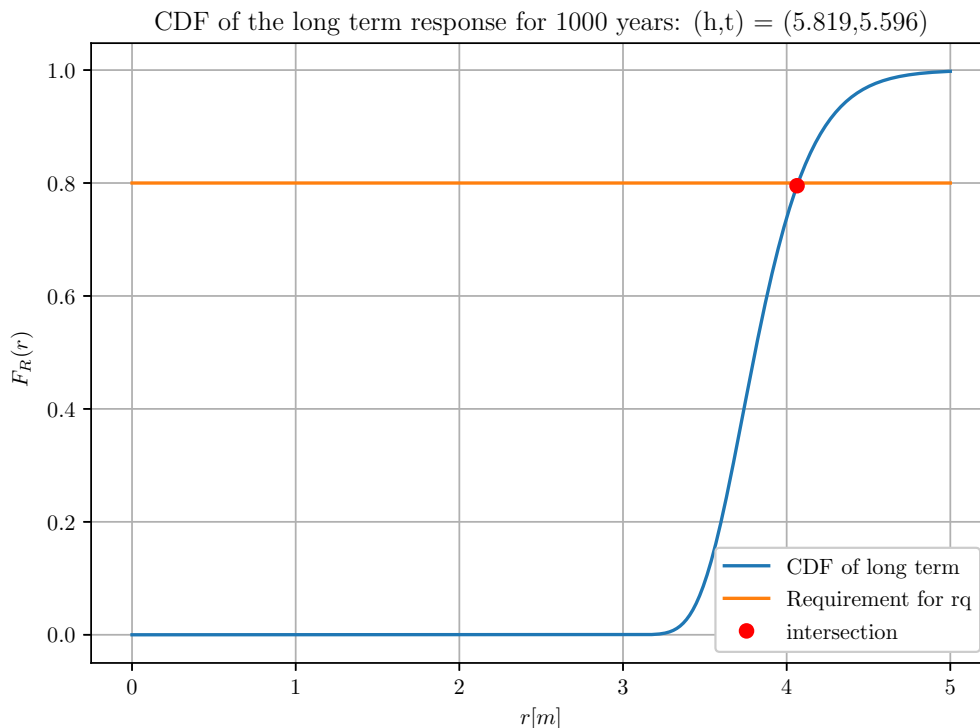


Figure 4.1.12: CDF of the long-term extreme response from ECM for a fractile value of $p = 0.80$ and return period $M = 1000$ years.

In Table 4.1.7 the characteristic responses for fractile values of 0.80, 0.85, 0.90 and 0.95 are summarized for the M -year return periods. The figures of the CDFs corresponding to the fractile values of 0.85, 0.90 and 0.95 can be found in Appendix C.1.

Table 4.1.7: Characteristic long-term responses from ECM for exceedance probabilities corresponding to return periods of $M = 10, 100$ and 1000 years.

M -year	Characteristic response			
	$p = 0.80$	$p = 0.85$	$p = 0.90$	$p = 0.95$
10	2.94	2.99	3.06	3.16
100	3.57	3.63	3.71	3.84
1000	4.09	4.16	4.25	4.40

4.1.4 IFORM and ISMCS

Figure 4.1.13, 4.1.14 and 4.1.15 show two CDFs for long-term extreme response. The orange CDF represents the Crude Monte Carlo Simulation while the blue CDF is biased

towards the design points obtained from IFORM. The exceedance probability corresponding to a given return period is represented by the green horizontal line. Furthermore, Table 4.1.8 contains the response value at the intersections between the CDFs and the line representing the exceedance probability, identified by the blue and red dots in the figures. The characteristic long-term extreme responses are read from these points. Elapsed time for running the algorithm is also presented in this table.

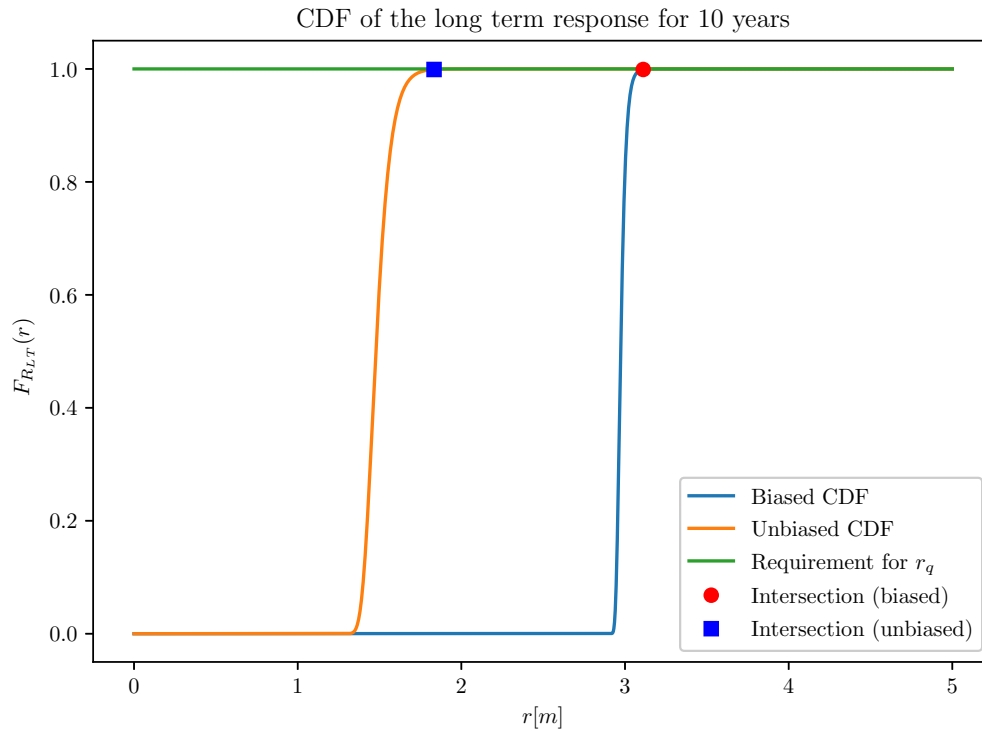


Figure 4.1.13: CDF of the long-term extreme response from Crude Monte Carlo Simulation with and without Importance Sampling for a return period of $M = 10$ years.

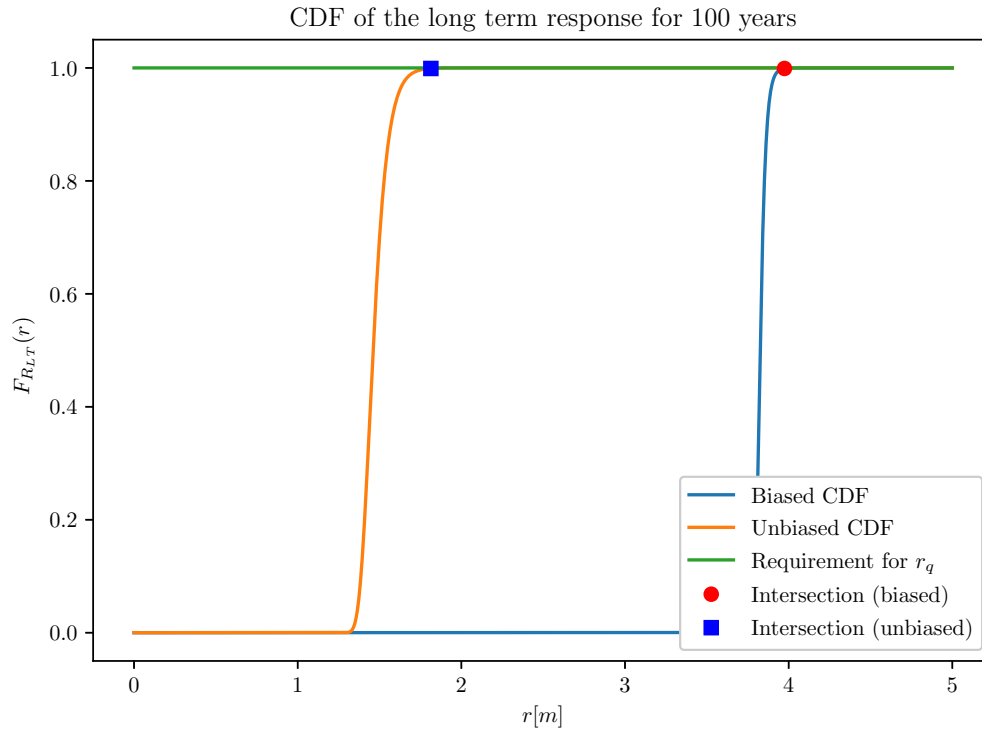


Figure 4.1.14: CDF of the long-term extreme response from Crude Monte Carlo Simulation with and without Importance Sampling for a return period of $M = 100$ years.

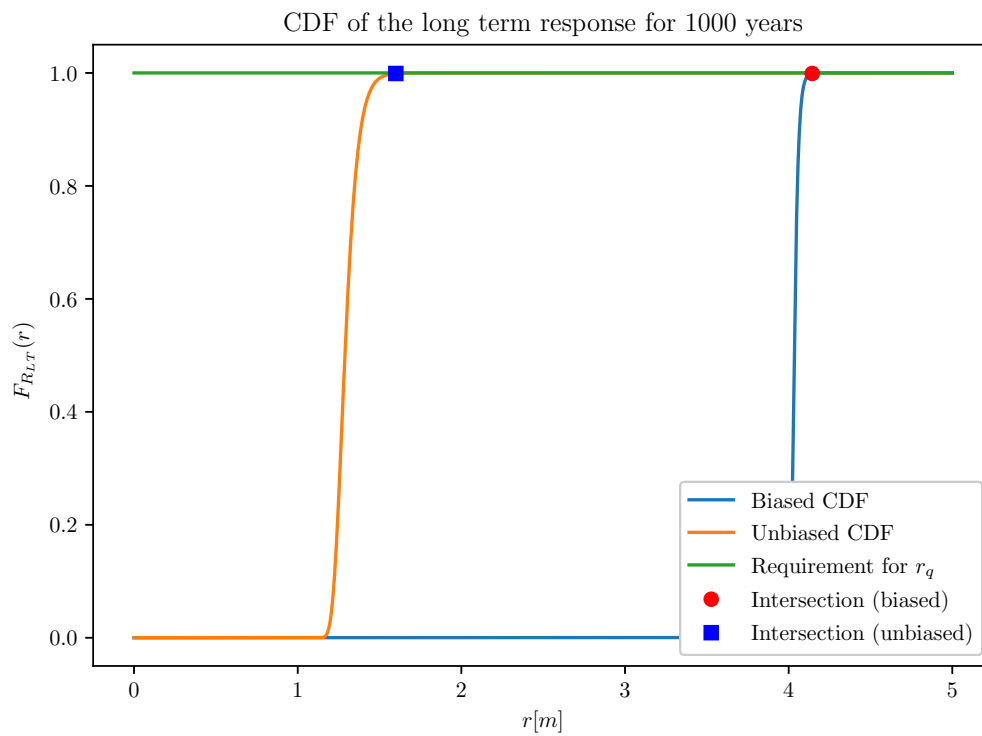


Figure 4.1.15: CDF of the long-term extreme response from Crude Monte Carlo Simulation with and without Importance Sampling for a return period of $M = 1000$ years.

Table 4.1.8: Characteristic long-term extreme responses from Crude Monte Carlo Simulation with and without Importance Sampling for return periods of $M = 10, 100$ and 1000 years.

M-year	Unbiased response [m]	Biased response [m]	Elapsed time [min]
10	1.83	3.11	5
100	1.81	3.97	5
1000	1.60	4.14	5

4.1.5 Gaussian Process Regression (GPR)

Figure 4.1.16 shows three groups of curves containing the training and test points where the characteristic responses are both predicted and evaluated in order to demonstrate the deviations between the two. Each group of curves contains the responses corresponding to return periods of 10, 100 and 1000 years in relation to the significant wave height h . The response values for the training points, predicted test points and evaluated test points are presented in Table 4.1.9, 4.1.10 and 4.1.11, respectively.

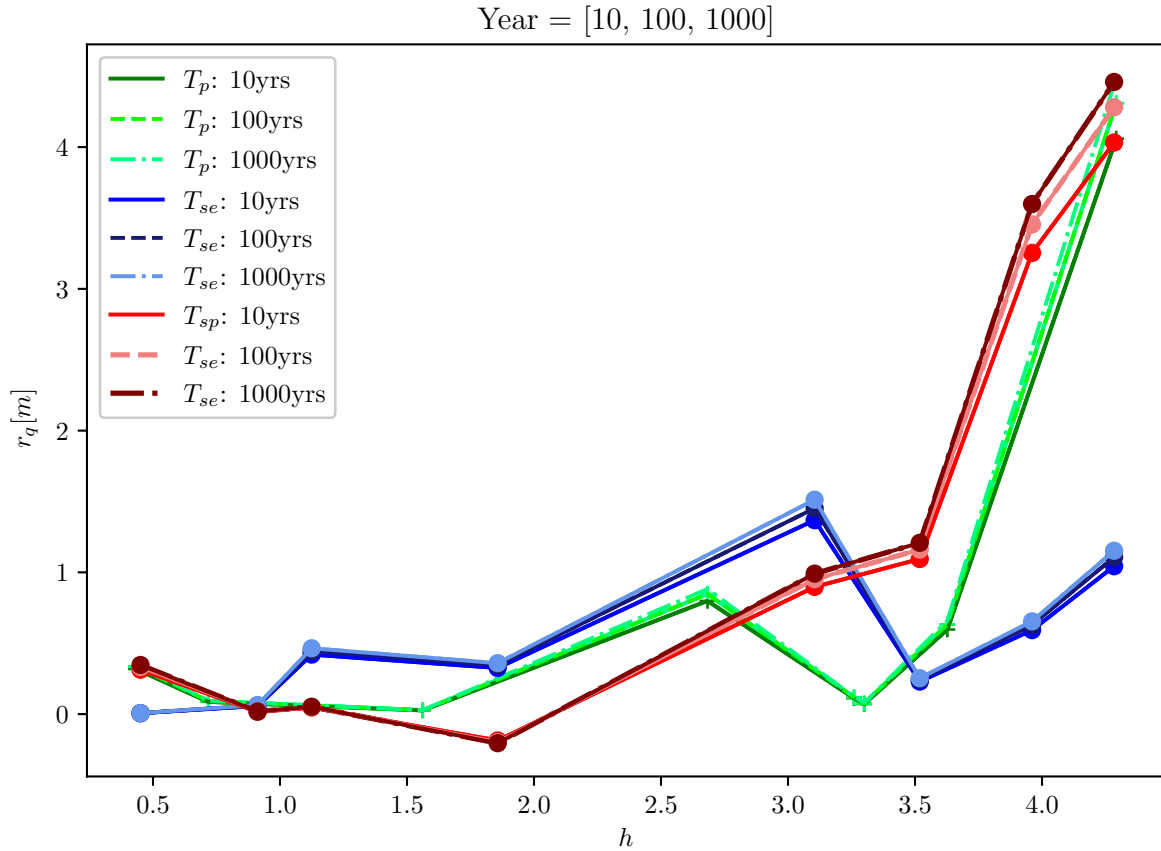


Figure 4.1.16: Characteristic responses for return periods of $M = 10, 100$ and 1000 years for training points and test points in relation to the significant wave height h . Here T_p , T_{se} and T_{sp} represent the training points, evaluated test points, and predicted test points, respectively.

Table 4.1.9: Characteristic response from the training points in GPR.

Training points		
$M=10$	$M=100$	$M=1000$
0.32	0.34	0.35
0.09	0.09	0.10
0.03	0.03	0.03
0.80	0.85	0.88
0.11	0.12	0.12
0.07	0.08	0.08
0.60	0.63	0.66
4.06	4.31	4.49

Table 4.1.10: Characteristic response from the predicted test points in GPR.

Predicted Test Points		
$M=10$	$M=100$	$M=1000$
0.31	0.33	0.35
0.02	0.02	0.02
0.05	0.05	0.05
-0.17	-0.20	-0.21
0.90	0.95	0.99
1.09	1.16	1.21
3.25	3.45	3.60
4.03	4.28	4.45

Table 4.1.11: Characteristic response from the evaluated test points in GPR.

Evaluated Test Points		
$M=10$	$M=100$	$M=1000$
0.01	0.01	0.01
0.06	0.06	0.06
0.42	0.45	0.46
0.33	0.35	0.36
1.37	1.45	1.51
0.23	0.24	0.25
0.59	0.63	0.65
1.04	1.11	1.15

The uncertainties related to the predicted characteristic response values are illustrated by the grey variance area in Figure 4.1.17:

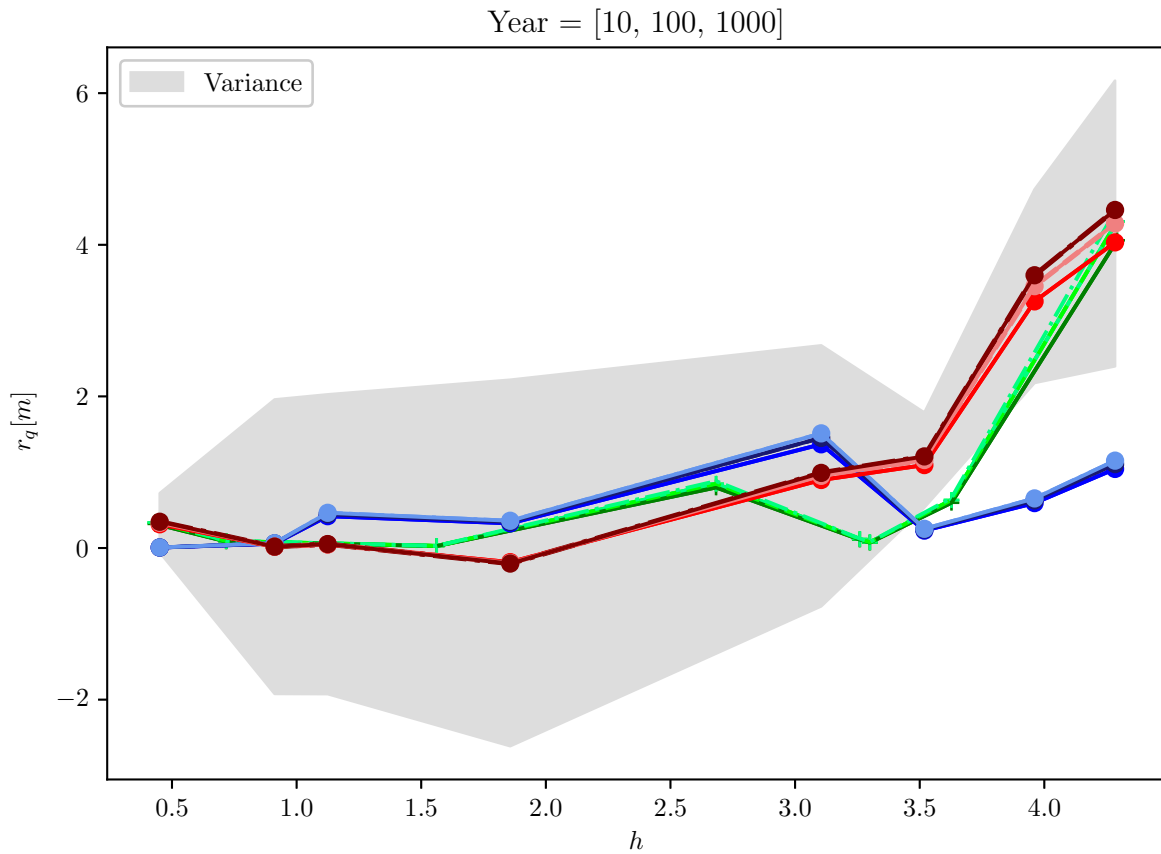


Figure 4.1.17: Variance of the predicted characteristic response values from GPR.

Figure 4.1.18 shows the randomly generated environmental parameters used as training and test points, as well as their position in the joint PDF. These points are also presented in Table 4.1.12.

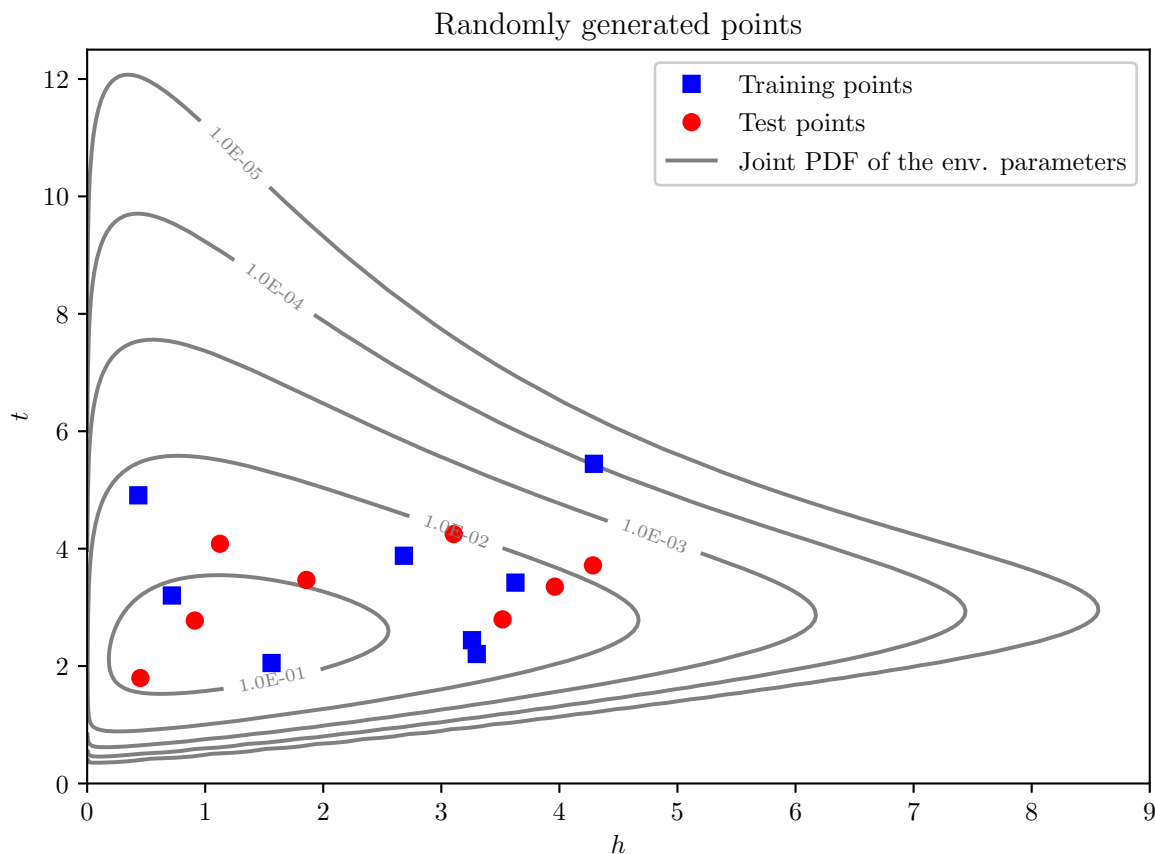


Figure 4.1.18: Randomly generated environmental parameters h and t for the training and test points.

Table 4.1.12: Randomly generated environmental parameters used as test and training points. Here h_{tp} and t_{tp} denote the training points, while h_{st} and t_{st} denote the test points for the significant wave height h and the zero-crossing period t .

Training Points		Test Points	
h_{tp}	t_{tp}	h_{st}	t_{st}
0.43	4.91	0.45	1.80
0.72	3.20	0.91	2.77
1.56	2.05	1.12	4.08
2.68	3.88	1.86	3.47
3.26	2.44	3.10	4.25
3.30	2.21	3.52	2.79
3.63	3.42	3.96	3.35
4.29	5.45	4.28	3.72

CHAPTER 5

Discussion

In this chapter the results presented in Chapter 4 are discussed and analysed. The effects of the assumptions made are debated and any deviations from the expected results are discussed. Consequences of any made presumption are also analysed and quantified.

5.1 Bridge Model

The bridge model used for this project is highly simplified compared to what is traditionally used for dynamical analysis of such a floating bridge, see for example Hermstad (2013) and Kvåle et al. (2016). Firstly, the span between each pontoon is modelled by a simple three-dimensional beam elements as opposed to a full truss element model. It might be argued that this is an oversimplification. However, the three-dimensional beam elements used are given mass and stiffness properties corresponding to an average cross-section of the full truss structure.

Another simplification made in the model is concerned with the pontoons. The Bergsøysund Bridge has three types of pontoons. The differences between these types of pontoons emerge from different geometry and ballasting. The three pontoon types are distributed such that the first type is located near the shore on each end of the bridge. The next type of pontoons, also consisting of two pontoons, are located intermediately between the shoreline and the middle of the bridge. Lastly, the third category of the pontoons, containing three pontoons, are located near the middle of the bridge span. It is these last types of pontoons which are used to represent all the pontoons in the bridge model.

Whether the assumption made for the pontoon types as described in the previous paragraph will have notable effects on the structural response may be subject for discussion. While it is highly likely that some effect would be found, the magnitude of this effect is not known. Since the pontoon type chosen in the model are the smallest of the three types, the inertia and therefore also the natural frequency of the bridge model will be less than for a more life-like model where also the bigger and heavier pontoons would be included.

It should be emphasized that the purpose of the bridge model is merely to serve as an example structure to which the considered calculation models can be applied. A more complete model would likely give even finer results but would also be much more time consuming and is therefore not prioritized in this project.

5.2 Natural Frequencies and Modes

The values for the natural frequencies and the mode shapes presented in Table 3.4.1 correspond quite well to what is found in the literature for the Bergsøysund Bridge (Kvåle et al., 2016). Natural frequencies and mode shapes are in general quite insensitive to the resolution of the finite element model. This means that accurate results can be obtained using a simplified finite element model, which is also observed here. This observation acts as a form of validation of this simplified bridge model, confirming its applicability for use as an exemplification for the long-term extreme response calculations conducted.

5.3 Discretization of Wave Angle and Frequency

Table 3.1.3 in Section 3.1.2 describes the discretization of the wave angles relative to the pontoons and the frequency used for these waves in the WADAM-analysis. The discretization used for these two quantities in the hydrodynamic modelling is important for the accuracy of the resulting hydrodynamic transfer function as well as for the hydrodynamic mass and damping matrices. This means that for the total analysis of the bridge model to be sufficiently accurate these two quantities also need to be accurately modelled.

Comparing the frequencies used for the hydrodynamic analysis with the natural frequencies obtained for the bridge model a rather good agreement is found. The natural frequencies shown in Table 3.4.1 are well within the frequency range for the hydrodynamic analysis which run from $7.5 \cdot 10^{-2}$ and up to 4 rad/s. The frequency discretization itself also seem to fit quite well to the natural frequencies. For frequency increments of $7.5 \cdot 10^{-2}$ rad/s all the natural frequencies in Table 3.4.1 are captured with sufficient accuracy.

When it comes to the discretization of the wave angles relative to the pontoons the comparison with the natural modes of the bridge model may appear slightly unclear. However, since the ten first modes in Table 3.4.1 are lateral, and not longitudinal, the most important modes are the ones ranging from about 45 to 135 degrees, as well as their 180 degree equivalents. With a fixed increment size of 10 degrees the considered wave

angle interval can be considered as sufficiently fine.

5.4 Full Integration

Section 3.5.2 shows that the Full Integration method is the most time-consuming method considered in this thesis. This is also the main preposition of this thesis; to find more efficient methods for full long-term analysis of extreme responses than Full Integration. In other words, the results from Full Integration contribute to further emphasize the need for more efficient calculation methods.

Although being both time-consuming and computationally expensive, the Full Integration method is recognized as being exact regarding the response values it return. This is because the approach takes into account sea states that contribute little or nothing to the overall loading on the structure being considered (Naess and Moan, 2013). This is illustrated as the integral of the joint probability density function over the environmental parameters of the significant wave height and the zero-crossing period are found to be of the value 0.9999. To achieve this value, step sizes giving 655 elements for the significant wave height and 150 elements for the zero-crossing period are chosen in the numerical integration conducted. With the integrated value being very close to unity, the assumption of exactness for this method can be said to be somehow valid. Therefore, the results from the other methods considered in this thesis can be held against the results from the full long-term approach based on the upcrossing rate model in order to evaluate their exactness.

As described in Section 2.6 both the exact and approximate formulations of the model based on the short-term extreme values are used for the cumulative distribution function. From Table 4.1.2 it is clear that the approximate formulation underestimates the response. The deviations for the responses are presented in Table 5.4.1 where it can be seen that the underestimation approaches 43.2 %. This is highly non-conservative. This underestimation shows that the chosen resolution of the environmental parameters for the approximate formulation should have been finer with a larger span. As for the models based on the short-term peaks and the exact formulation of the short-term extreme values, see Table 4.1.2, the results are quite similar to the model based on the upcrossing rate.

Table 5.4.1: Deviation in the results obtained from Full Integration based on the upcrossing rate model and the approximate formulation of the short-term extreme values model.

<i>M</i> -year	Upcrossing rate	Short-term extreme values (approximate)	Deviation
10	3.04	2.13	43.19 %
100	3.55	2.14	39.70 %
1000	4.06	2.35	42.12 %

5.5 IFORM

By considering Table 4.1.4 and 4.1.5 which present responses obtained from IFORM using the exact and approximate formulation, one can observe that the responses from the approximate formulation slightly falls on the non-conservative side when compared to the exact formulation. The maximum underestimation is 0.64 % for $M = 10$ years. On the contrary, the approximate formulation is slightly more efficient with one minute less run time. This difference in run time can be explained when the number of iterations n_{it} and the number of times the short-term response is calculated n_{st} are studied more carefully. The approximate formulation needs fewer iterations and short-term response evaluations in order to converge, resulting in a shorter run time.

5.6 Comparing Full Integration, IFORM and ECM

The characteristic extreme response values obtained from the methods of Full Integration, IFORM and ECM are quite similar to each other. This is demonstrated in Table 5.6.1 where the response values from the exact formulation of the Full Integration method based on the model of the upcrossing rate, the response values from ECM using a fractile value of $p = 0.8$ and the response values from IFORM based on the exact formulation are presented. By using the result from Full Integration as a basis, the deviations from these response values compared to the response values from ECM and IFORM are presented in percent in Table 5.6.1.

Table 5.6.1: Deviation of the response values obtained from IFORM (exact) and ECM when compared to the response values obtained for Full Integration (based on the upcrossing rate formulation).

	Characteristic response values			Deviation from Full Integration	
	Full Integration (upcrossing rate)	IFORM (exact)	ECM (p=0.8)	IFORM (exact)	ECM (p=0.8)
<i>M</i> -year					
10	3.05	3.14	2.94	2.95 %	3.6 %
100	3.55	3.73	3.57	5.07 %	0.56 %
1000	4.06	4.29	4.09	5.67 %	0.74 %

Comparing the design points obtained from the various methods is another way of controlling the quality or correlation of the results. Figure 5.6.1, 5.6.2 and 5.6.3 show the location of the design points from ECM and IFORM along with their *M*-year equivalent contours on the joint PDF over the environmental parameters. The contribution to the integrand in the Full Integration method is also plotted as a contour for the threshold values close to the characteristic response. This contribution contour is normalized, and the magnitude is given by the side bar in the figures.

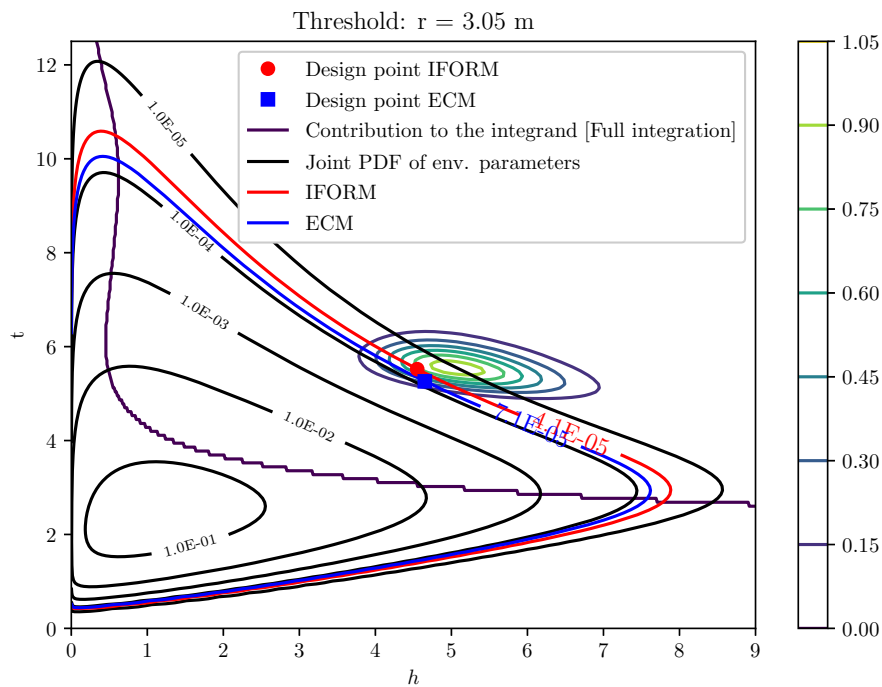


Figure 5.6.1: Location of the design points in the joint PDF over the environmental parameters and a contour of the contribution to the integrand in the method of Full Integration for a return period of $M = 10$ years.

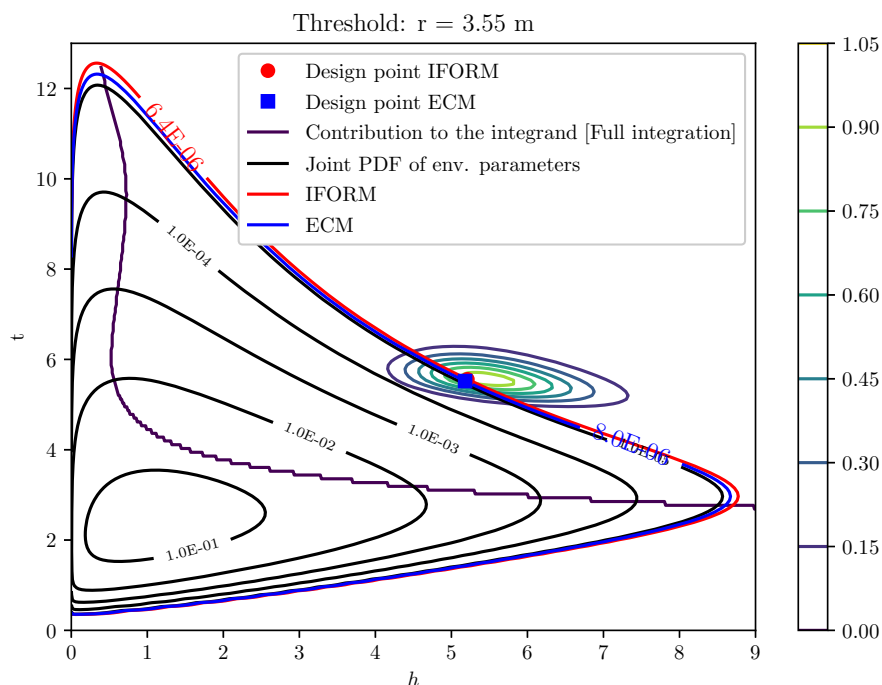


Figure 5.6.2: Location of the design points in the joint PDF over the environmental parameters and a contour of the contribution to the integrand in the method of Full Integration for a return period of $M = 100$ years.

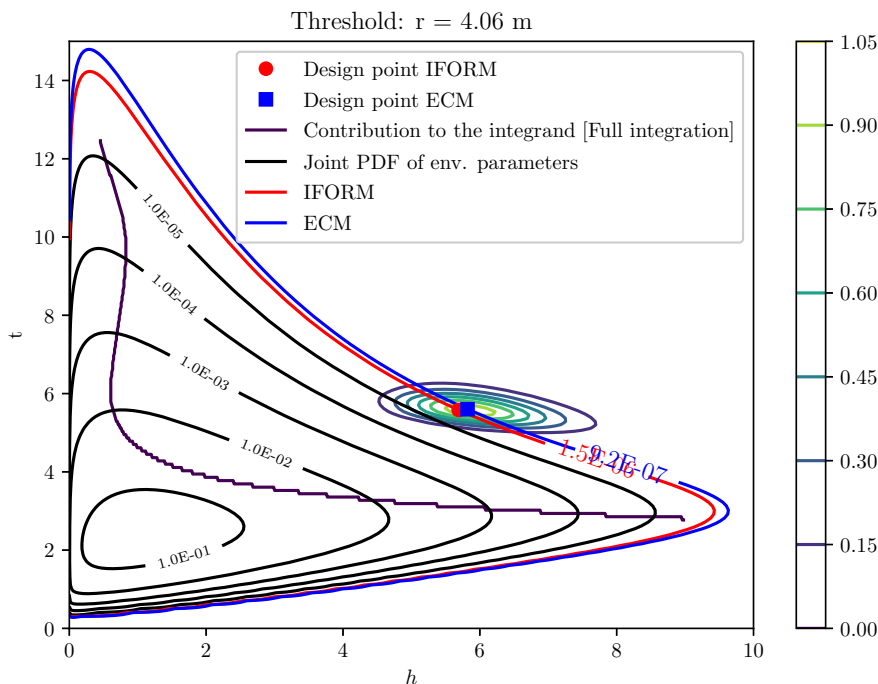


Figure 5.6.3: Location of the design points in the joint PDF over the environmental parameters and a contour of the contribution to the integrand in the method of Full Integration for a return period of $M = 1000$ years.

From the figures it can be seen that the location of the design points from ECM and IFORM lay in the vicinity of the concentrated contribution to the integrand. It seems reasonable that the design points are close to the areas where the contribution to the overall response is the highest. This further substantiates the confidence that all the considered methods have converged towards the actual response value.

The design points for return periods of $M = 10$, 100 and 1000 years obtained from IFORM (exact and approximate formulations) as well as from ECM are averaged and summarized in Table 5.6.2. Their probability of occurrence is also calculated from their joint PDF. It can be observed that this probability of occurrence decreases as the duration of the return period increases.

Table 5.6.2: Averaged design points obtained from IFORM (exact and approximate formulation) and ECM along with their respective probabilities of occurrence.

M -year	Averaged environmental parameters [h, t]	Probability of occurrence
10	[4.59, 5.42]	5.05e−05
100	[5.18, 5.54]	7.45e−06
1000	[5.74, 5.58]	1.27e−06

Despite its accuracy, it is clear that the method of Full Integration is not the most efficient. In this regard, Table 5.6.3 really shows the power of the other considered methods for long-term extreme response analysis. Here the run time for each method is compared to the run time for Full Integration. A considerable improvement in run time is found for these alternative methods. The elapsed time for the Full Integration method is in this table defined as the average run time for all the formulations used for Full Integration. The deviation in run time between each of these formulations is ± 3 minutes.

Table 5.6.3: Computational run time for all return periods M of the different methods where the run time for the Full Integration is used as the basis for the comparison.

Method	Elapsed time [min]	Efficiency
Full Integration	2475	1
IFORM (exact)	10	248 \times faster
IFORM (approximate)	8	310 \times faster
ECM	9	275 \times faster
CMCS	15	165 \times faster

The considerable time consumption for Full Integration might be lowered by calculating the CDF given by Equation (2.7.10) for a narrower and more relevant span of response thresholds. Further optimization of the WAWI-toolbox used to calculate the response spectrum might also be necessary. However, it can be argued that the method of Full Integration is inherently slow since the methods ECM, IFORM, ISMCS and GPR are also dependent on the same WAWI-toolbox while maintaining their efficiency. A general observation is that the need for calculating the moments in a "grid-like" manner is the biggest disadvantage of Full Integration. On the contrary, this "grid-like" approach

considers every single environmental parameter, resulting in the superior accuracy.

The approximate formulation of IFORM is the fastest of the considered methods by being 310 times faster than the method of Full Integration. This is a quite good result when the accuracy of this method is studied in relation to the Full Integration method based on the upcrossing rate formulation, see Table 5.6.4. Here the maximum deviation lies around 5.14 % for a return period of $M = 1000$ years. It is also worth noting that the approximate formulation in general exhibits higher accuracy than the exact formulation of IFORM when a similar quality control is conducted, see Table 5.6.1.

Table 5.6.4: Deviation of the responses obtained from the approximate formulation of IFORM compared to the responses obtained from Full Integration based on the upcrossing rate formulation for return periods of $M = 10, 100$ and 1000 years.

	Characteristic response [m]		Deviation from Full Integration
M -year	Full Integration (upcrossing rate)	IFORM (approximate)	IFORM (approximate)
10	3.04	3.12	2.56 %
100	3.55	3.72	4.57 %
1000	4.06	4.28	5.14 %

5.7 IFORM and ISMCS

The Monte Carlo Simulation method biased towards the design points obtained from IFORM is meant to accelerate the efficiency compared to the traditional Crude Monte Carlo Simulation. The main disadvantage of this biased method is having to assume that the design points from IFORM are available and that they are correct to begin with. Apart from that, this method showed acceptable accuracy for only 50 generated samples. The deviations compared to the characteristic responses from the method of Full Integration using the exact formulation are presented in Table 5.7.1. The largest deviation is 11.8 % for a return period of $M = 100$ years. This deviation is expected to be lower as more points are sampled and should eventually converge towards the results from IFORM given in Table 4.1.4.

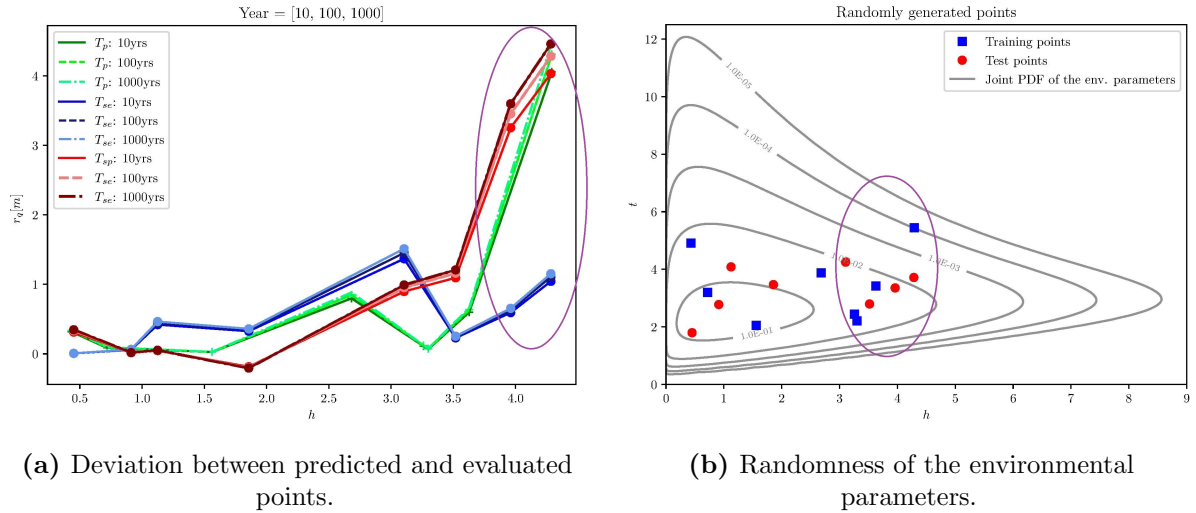
Table 5.7.1: Deviation between the characteristic responses obtained from the exact Full Integration method and IFORM-based Monte Carlo Simulation for return periods of $M = 10$, 100 and 1000 years.

	Characteristic response [m]		Deviation from Full Integration
M -year	Full Integration (exact)	IFORM and ISMCS	IFORM ISMCS
10	3.05	3.11	1.97 %
100	3.55	3.97	11.8 %
1000	4.06	4.14	1.93 %

5.8 Gaussian Process Regression (GPR)

The accuracy of the predicted values obtained from GPR are just as good as for the training points. Even though this is as expected, it presented great challenges to achieve reasonable training points with a fair amount of spreading and span such that the predicted values would have lower variance. From a first look at the joint PDF of the environmental parameters, see Figure 4.1.18, a somehow poor correlation between the wave height h and the zero-crossing period t can be observed. This affects the covariance matrix produced for the training and test points resulting in the massive variances for the predicted values, which is seen in Figure 4.1.16.

It is observed that the red curves (predicted points) follow the green curves (training points) rather accurately. Figure 5.8.1 shows this clearly. For the blue curves, which represent the evaluated test points, the same environmental parameters are used as for the predicted test points and therefore these are expected to exhibit some similarities. However, in this case the predicted values deviate more from the expected results due to big jumps in-between the randomly generated parameters used for the test and training points. This can be seen from Figure 5.8.1 (b) and the points responsible for this jump can be seen in Figure 5.8.1 (a):



(a) Deviation between predicted and evaluated points.

(b) Randomness of the environmental parameters.

Figure 5.8.1: Effects of the poor correlation between the significant wave height h and the zero-crossing period t .

The variance of the predicted points shown in Figure 4.1.17 tends to be strongly affected by whether there exists a training point close by. This is seen from the same figure for $h \approx 1.9$ meters where there is a lack of training points in the location of the test points and the variance is correspondingly bigger. On the contrary, the variance is significantly narrower at $h \approx 3.5$ meters where a training point is close to the test points. These results, which are achieved with only 8 training points, demonstrate the potential of the GPR-method in mapping the characteristic responses for different combinations of the environmental parameters. The method appears efficient compared to carrying out a Full Integration calculation or a Crude Monte Carlo Simulation.

5.9 Modelling the Environmental Parameters

The assumed probability density functions and their model parameters presented in Table 3.5.1 are assumed to be representative for sea states at the northwestern part of Norway. However, these models for the environmental parameters ought to be revisited given the magnitude of the extreme response achieved for the various return periods. The possibility of the models used in this thesis overestimating the actual environmental loads should be entertained. For greater accuracy and validity, the model for the environmental parameters should be developed from local measurements of the sea state around the bridge over an extended time period.

5.10 Magnitude of the Extreme Response

The extreme characteristic responses presented in Table 5.6.1 obtained from Full Integration, IFORM and ECM span from 3.05 to 4.29 meters for the various return periods. Although there are deviations between the methods, the responses are more or less of the same magnitude. A displacement response around ± 4 meters can be considered as an extreme load for any structure, especially for a floating bridge. How credible are these response values?

As discussed in Section 5.1, the simplification of the FE-model of the bridge might have resulted in an overall weaker structure. This presumably weaker structure might have lacked the resistance needed to withstand these extreme wave loads. For further validation, the bridge is tested against lower external forces. The marginalized mean values of the environmental parameters and their probability of occurrence presented in Table 5.10.1 are used to calculate the extreme long-term responses shown in Table 5.10.2. These responses are obtained by utilizing the conditional short-term extreme response given in Equation (2.6.12) along with the requirement for the characteristic response given by Equation (2.7.14).

Table 5.10.1: Marginalized mean values of the environmental parameters.

Marginal environmental parameters $[h, t]$	Probability of occurrence
[1.58, 2.87]	0.157

Table 5.10.2: Extreme responses obtained with marginalized mean values of the environmental parameters.

M-year	Extreme responses [m]
10	0.116
100	0.124
1000	0.130

It can be observed that the responses are considerably lower when smaller waves are taken into account. The responses achieved with the marginalized environmental parameters

span from 0.116 to 0.130 meters for the various return periods. This is approximately 96 % lower than the responses obtained with the design points from Full Integration, ECM and IFORM presented in Table 5.6.1. Based on the observation that the magnitude of the extreme response is affected to such a degree by the environmental parameters, it can be argued that the FE-model of the bridge has sufficient strength. When the probability of occurrence for the marginalized environmental parameters is compared to that of the design points in Table 5.6.1, it is evident that the values in Table 5.6.1 represent extremely rare events with massive wave loads. Furthermore, the accuracy of the environmental parameter representation as discussed in Section 5.9 will indeed affect the response. Higher response will naturally be obtained for an overestimated sea state.

CHAPTER 6

Conclusions

6.1 Conclusion

This thesis has presented and demonstrated several methods for estimating the long-term extreme response of floating bridges. Even though the primary objective is to present these methods, they are exemplified using a simplified model based on the Bergsøysund Bridge. The obtained lateral extreme responses are considered to be high as a result of multiple simplifications of the bridge model and assumptions made around the environmental parameters but also due to the magnitude of the assumed waves. However, the similarity in the magnitude of the responses from the three main methods (Full Integration, IFORM and ECM) together with the biased Monte Carlo Simulation substantiates the statement that these methods can be considered as cross-checked.

Both the exact and approximate formulations of IFORM estimated the results from Full Integration with high accuracy. One important observation is that the results from the approximate formulation of IFORM falls on the non-conservative side compared to the exact formulation while it overestimates the response when compared to the exact Full Integration results. When it comes to efficiency, the approximate formulation of IFORM is found to be superior. The approximate formulation of Full Integration based on the short-term extreme values also underestimates the response in an exaggerated manner and is therefore considered to be highly non-conservative. Regarding ECM, the responses are quite conservative and a fractile value of $p = 0.80$ is found to be suitable by comparison with the Full Integration and IFORM-results. Furthermore, the method of GPR showed solid potential in predicting the long-term extreme response but still exhibits some challenges with respect to stability.

6.2 Proposal for Further Work

Full Integration

- **Environmental parameters:** The limits and number of elements for the environmental parameters used in this thesis are found to be sufficient for the considered models except for the model based on the approximate formulation of the short-term extreme values. Higher limits with more elements for the

environmental parameters should be investigated to push the integral of their joint PDF as close to unity as possible and study the effect it has on the accuracy.

- **Efficiency:** Table 4.1.3 shows that the calculation of both the response spectrum and the spectral moments is very computationally expensive. A remedy for this can be to use a regressive approach. The topography of the moments as can be seen from Figure 3.5.1 is sufficiently well behaved to be fitted by for example GPR. The computation time is expected to be drastically reduced as the moments are calculated only at a few training points rather than in a "grid-like" manner as implemented in this thesis.

GPR

- **Importance Sampling:** In order to generate stable training points with high relevance, an Importance Sampling technique similar to what is described in Section 2.14 can be used. The environmental parameters generated are then weighted such that the generated random samples are biased towards the region that contributes the most to the response.
- **Kernel types:** The challenges related to the randomness and poor correlation of the environmental parameters is one of the reasons for the large variance observed for the predicted points. Besides increasing the amount of training points, different kernel types with more flexibility should be investigated. This would be kernels with more parameters than the Matérn kernel or even combinations of several kernels as is discussed by Duvenaud (2014).

Environmental Parameters

- **Modelling the Environmental Parameters:** For a more accurate representation of the sea state, local measurements around the bridge should be used to estimate the environmental parameters.

Bibliography

- Aas-Jacobsen (2021). *Unique combination of floating bridge and cable-stayed bridge*. <https://www.aas-jacobsen.com/projects/nordhordlandsbrua/>. (Accessed on March 26, 2021).
- Abaqus (2014). *Beam element library*. <https://abaqus-docs.mit.edu/2017/English/SIMACAEELMRefMap/simaelm-r-beamlibrary.htm>. (Accessed on March 08, 2021).
- Battjes, J. A. (1972). *Long-Term Wave Height Distributions at Seven Stations Around the British Isles*. <https://link.springer.com/content/pdf/10.1007/BF02312702.pdf>. (Accessed on March 22, 2021).
- Borgman, L. E. (1967). *Ocean wave simulation for engineering design*. tech. rep. (Accessed on June 02, 2021).
- de Freitas, N. (2013). *Machine learning - Introduction to Gaussian processes* [Video]. YouTube. <https://youtu.be/4vGiHC35j9s>. (Accessed on May 12, 2021).
- Det Norske Veritas (2010). *Recommended Practice: Environmental Conditions and Environmental Loads*. <https://rules.dnvgl.com/docs/pdf/dnv/codes/docs/2010-10/rp-c205.pdf>. (Accessed on February 27, 2021).
- Duvenaud, D. K. (2014). *Automatic Model Construction with Gaussian Processes*. <https://www.cs.toronto.edu/~duvenaud/thesis.pdf>, University of Cambridge. (Accessed on May 14, 2021).
- European Roads (2014). *Nordhordlandsbrua*. <https://flickr.com/photos/chriszwolle/14511251244/in/faves-192992855@N04/>. (Accessed on May 14, 2021).
- Genton, M. G. (2001). *Classes of Kernels for Machine Learning: A Statistics Perspective*. <https://dl.acm.org/doi/10.5555/944790.944815>, Department of Statistics, North Carolina State University. (Accessed on March 10, 2021).
- Giske, F.-I. G. (2017). *Long-Term Extreme Response Analysis of Marine Structures Using Inverse Reliability Methods*. <https://ntnuopen.ntnu.no/ntnu-xmlui/Finn-Idar>. (Accessed on February 7, 2021).

Giske, F.-I. G., Leira, B. J., and Øiseth, O. (2017). *Full Long-Term Extreme Response Analysis of Marine Structures Using Inverse FORM*. <https://ntnuopen.ntnu.no/ntnu-xmlui/Finn-Idar>. (Accessed on February 22, 2021).

Gramstad, O., Agrell, C., Bitner-Gregersen, E., Guo, B., Ruth, E., and Vanem, E. (2019). *Sequential sampling method using Gaussian process regression for estimating extreme structural response*. <https://www.journals.elsevier.com/marine-structures>, Marine Structures. (Accessed on March 05, 2021).

Hartz, B. J. and Mukherjee, B. (1977). *Dynamic response of a floating bridge to wave forces*. International Conference on Bridging Rion-Antirion. Patras, Greece. (Accessed on June 02, 2021).

Haver, S., Bruserud, K., and Baarholm, G. S. (2013). *Environmental contour method: An approximate method for obtaining characteristic response extremes for design purposes*. <https://www.semanticscholar.org/paper/Environmental-contour-method%3A-An-approximate-method-Haver-Bruserud/b7051259382a786da8d91ba0dc4772cdbf290006>. (Accessed on March 02, 2021).

Hermstad, S. M. (2013). *Dynamic Analysis of the Bergsøysund Bridge in the Time Domain*. <https://ntnuopen.ntnu.no/ntnu-xmlui/handle/11250/237296>. (Accessed on March 08, 2021).

Heuberger, C. (2018). *Assessment of the dynamic response of a floating pontoon bridge with a fiber reinforced polymer superstructure*. <https://repository.tudelft.nl/>. (Accessed on April 12, 2021).

Holand and Langen, I. (1972). *Salhus floating bridge: theory and hydrodynamic coefficients*. tech. rep. (Accessed on June 02, 2021).

Kvåle, K. A., Sigbjornsson, R., and Øiseth, O. (2016). *Modelling the stochastic dynamic behaviour of a pontoon bridge: A case study*. <https://www.elsevier.com/locate/compstruc>. (Accessed on February 7, 2021).

Kvåle, K. A. (2017). *Structural Monitoring of an End-Supported Pontoon Bridge*. <https://doi.org/10.1016/j.marstruc.2016.12.004>. (Accessed on May 14, 2021).

- Kvåle, K. A. and Petersen (2018). *The Bergsøysund Bridge monitoring project*. <https://www.ntnu.edu/kt/research/dynamics/monitoring/bergsøysund>. (Accessed on March 26, 2021).
- Köhler, J. (2018). *L06 - Introduction to Structural Reliability: First Order Reliability Method*. TKT4196 - Aspects of Structural Safety. <https://ntnu.blackboard.com>. (Accessed on February 22, 2021).
- Langen, I. and Sigbjörnsson, R. (1979). *Frequency Domain Analysis of a Floating Bridge Exposed to Irregular Short-Crested Waves*. SINTEF, Trondheim. (Accessed on February 19, 2021).
- Langen, I. and Sigbjörnsson, R. (1980). *On stochastic dynamics of floating bridges*. Engineering Structures, vol.2, no. 4, pp. 209–216. (Accessed on June 02, 2021).
- Melchers, R. E. and Beck, A. T. (2008). *Structural Reliability Analysis and Prediction*. <https://www.wiley.com/en-us/Structural+Reliability+Analysis+and+Prediction>, John Wiley and Sons Ltd. (Accessed on March 29, 2021).
- Monsrud, J. (2009). *Transport i Norge*. https://www.ssb.no/a/publikasjoner/pdf/sa_105/sa_105.pdf. (Accessed on May 20, 2021).
- Murphy, K. (2007). *Multivariate Gaussians*. <https://www.cs.ubc.ca/~murphyk/Teaching/CS340-Fall107/reading/gauss.pdf>. (Accessed on March 25, 2021).
- Naess, A. and Moan, T. (2013). *Stochastic Dynamics of Marine Structures*. Cambridge University Press, New York. (Accessed on February 5, 2021).
- Newland, D. E. (2012). *An Introduction to Random Vibrations, Spectral & Wavelet Analysis*. Dover, third edition.
- Øiseth, O. (2020). *A Note on Long-Term Distribution of Wind Induced Load Effects With Applications to Structures With High Natural Periods*. (Accessed on February 17, 2021).
- Sagrilo, L., Naess, A., and Doria, A. (2011). *On the long-term response of marine structures*. <https://www.journals.elsevier.com/applied-ocean-research>, Applied Ocean Research. (Accessed on March 25, 2021).

Sweitzer, K., Bishop, N., and Genberg, V. (2004). *Efficient Computation of Spectral Moments for Determination of Random Response Statistics*. <http://citeseerx.ist.psu.edu/viewdoc/download;jsessionid=8BF485537BFB5541467FB257D8CA90B7?doi=10.1.1.1002.6562&rep=rep1&type=pdf>. (Accessed on March 30, 2021).

Weisstein, E. W. (2021). *Positive Definite Matrix*. <https://mathworld.wolfram.com/PositiveDefiniteMatrix.html>. (Accessed on May 12, 2021).

Williams, M. (2016). *Structural Dynamics*. Broken Sound Parkway NW: CRC Press. (Accessed on June 02, 2021).

Winterstein, S. R. and Haver, S. (1993). *Environmental Parameters For Extreme Response Inverse Form With Omission Factors*. Proceedings of the 6th International Conference on Structural Safety and Reliability. Innsbruck, Austria,. (Accessed on March 03, 2021).

Xu, Y., Øiseth, O., Moan, T., and Naess, A. (2018). *Prediction of long-term extreme load effects due to wave and wind actions for cable-supported bridges with floating pylons*. <https://ntnuopen.ntnu.no/ntnu-xmlui/handle/11250/2587163>. (Accessed on February 27, 2021).

Appendices

Appendix A

A.1 Dimensions of Mid-Span Pontoon

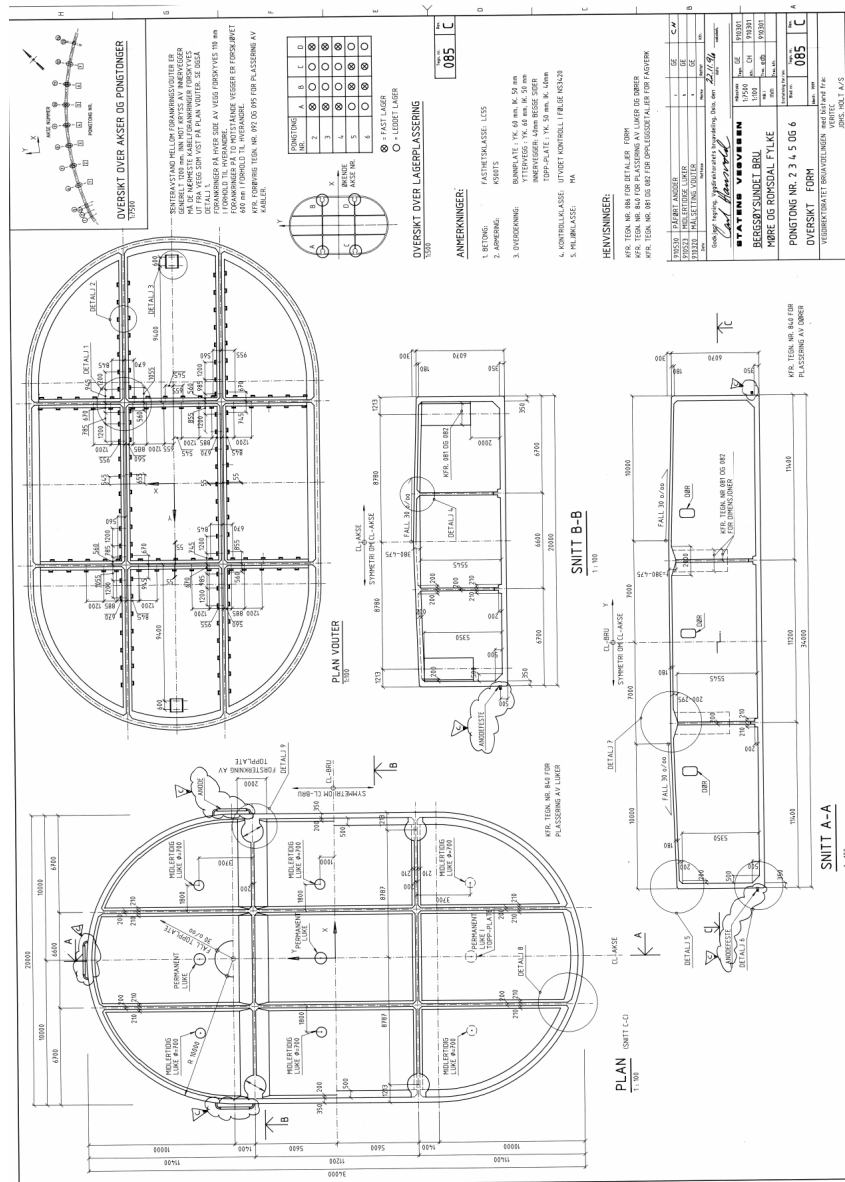


Figure A.1.1: Geometrical dimensions of pontoon 4 from the Bergøysund Bridge (Hermstad, 2013).

Appendix B

B.1 Iteration Points in U-space for Exact IFORM-Formulation

Iteration points obtained in U-space for 10 -year response

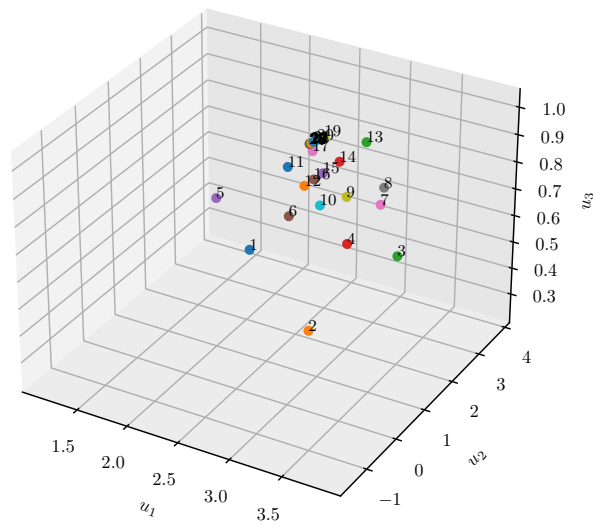


Figure B.1.1: 10-year return period.

Iteration points obtained in U-space for 100 -year response

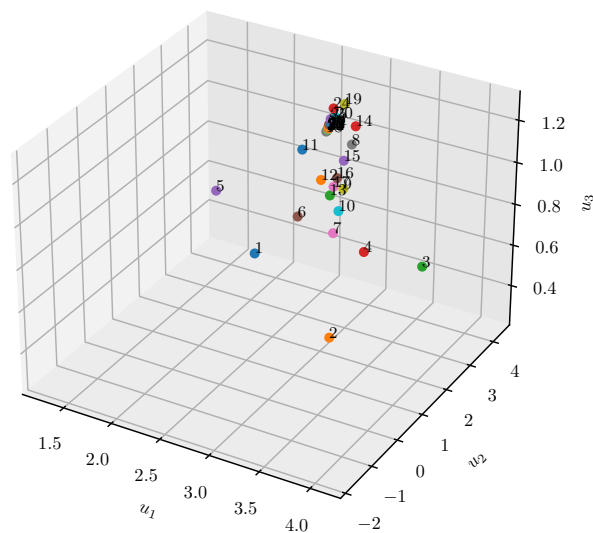


Figure B.1.2: 100-year return period.

Iteration points obtained in U-space for 1000 -year response

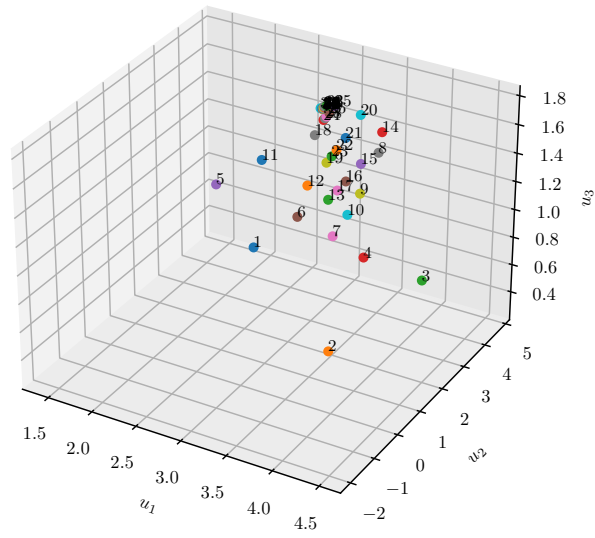


Figure B.1.3: 1000-year return period.

B.2 Iteration Points in U-space for Approximate IFORM-Formulation

Iteration points obtained in U-space for 10 -year response

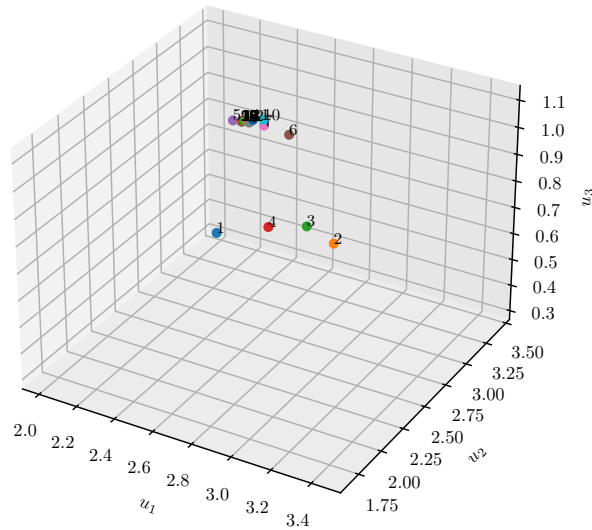


Figure B.2.1: 10-year return period.

Iteration points obtained in U-space for 100 -year response

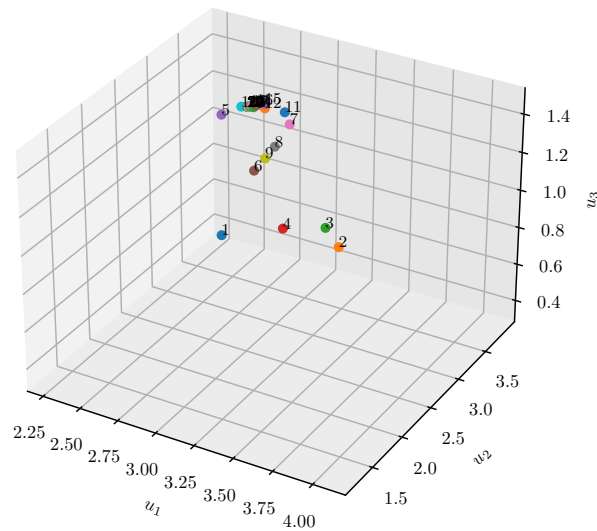


Figure B.2.2: 100-year return period.

Iteration points obtained in U-space for 1000 -year response

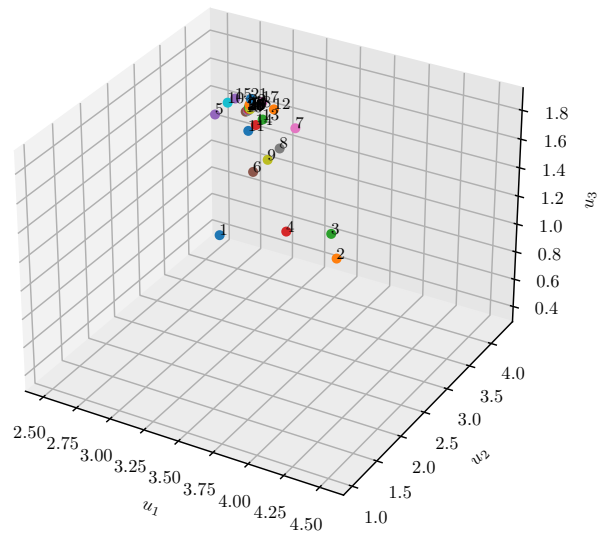


Figure B.2.3: 1000-year return period.

Appendix C

C.1 CDF for the Long-Term Extreme Response from ECM

Cumulative Distribution Functions from the Environmental Contour Method for the long-term extreme response for various fractile values p and return periods M .

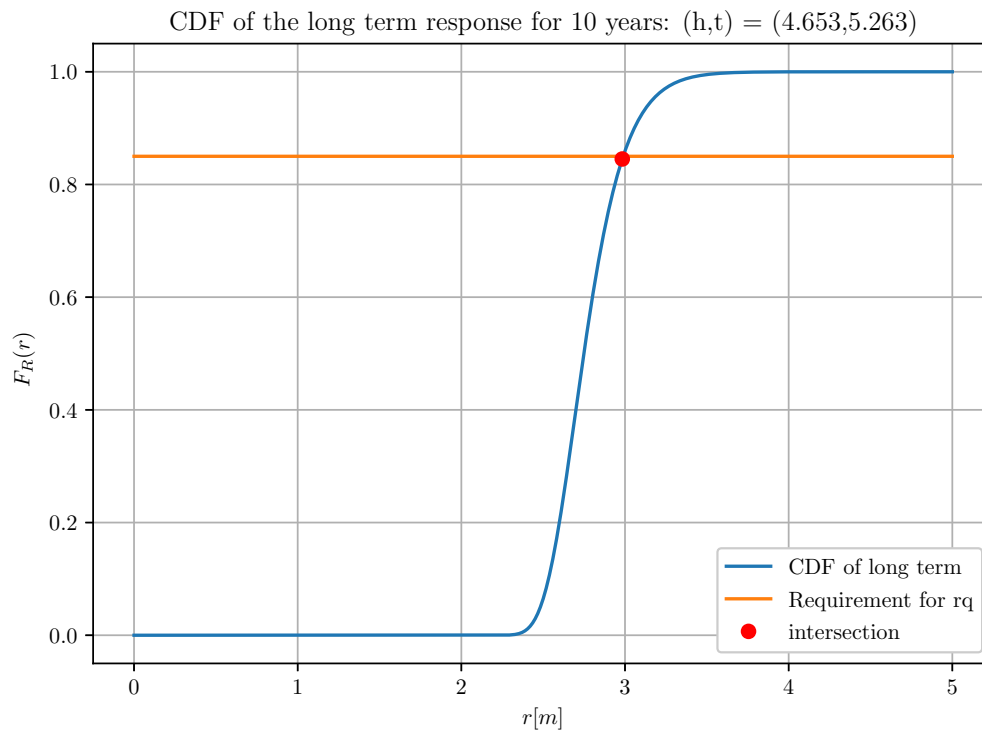


Figure C.1.1: $p = 0.85$, $M = 10$.

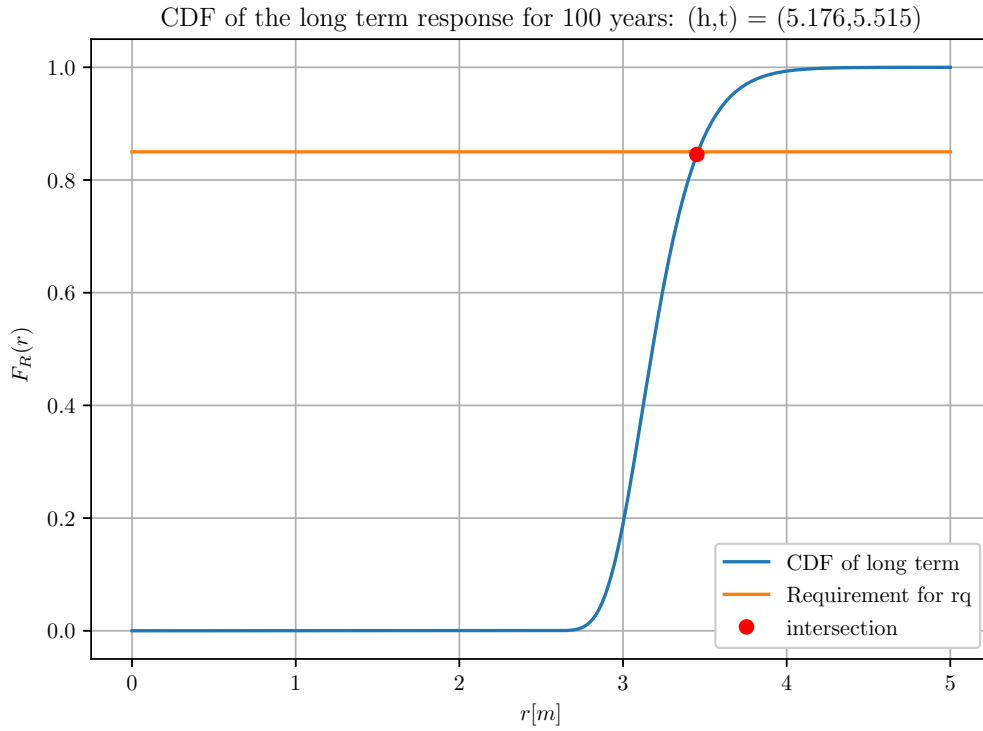


Figure C.1.2: $p = 0.85$, $M = 100$.

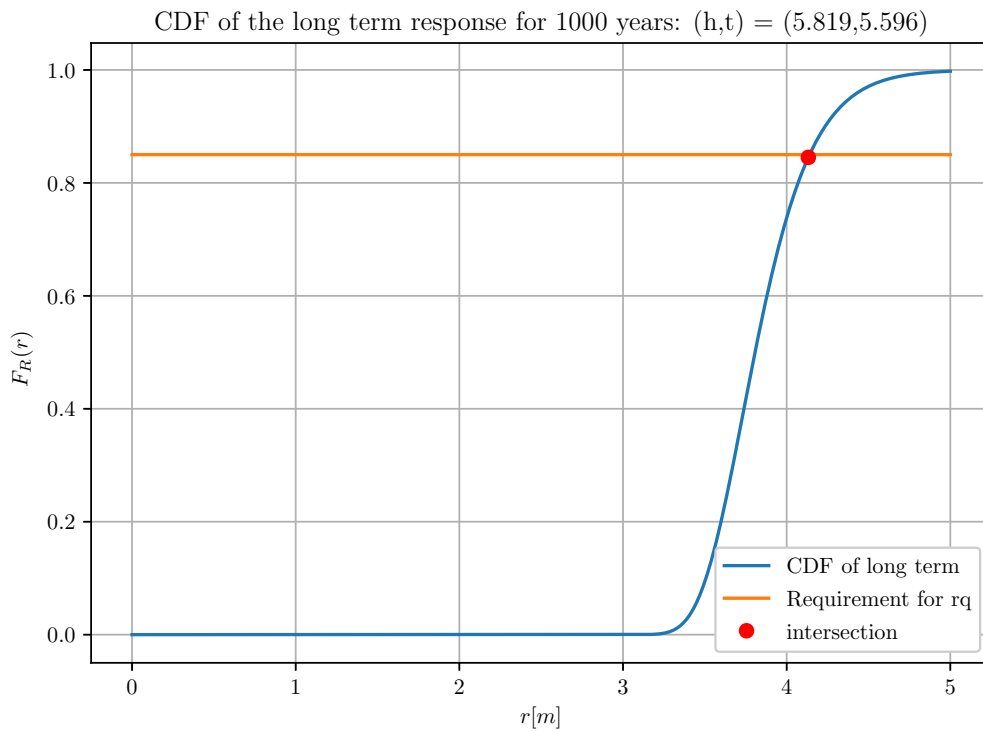


Figure C.1.3: $p = 0.85$, $M = 1000$.

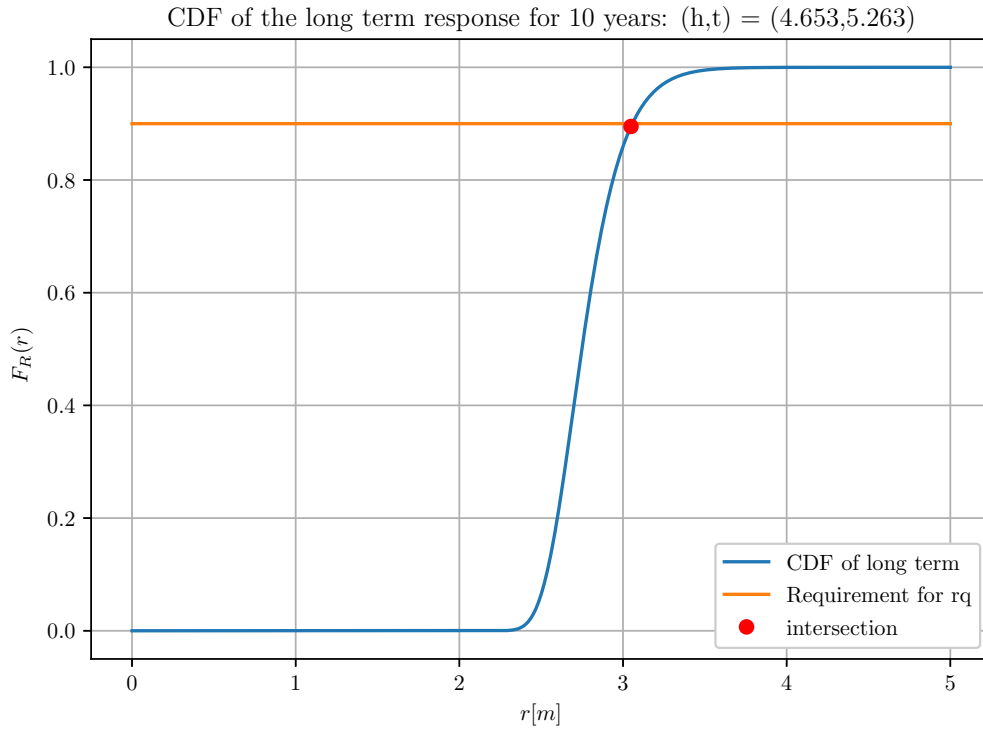


Figure C.1.4: $p = 0.90$, $M = 10$.

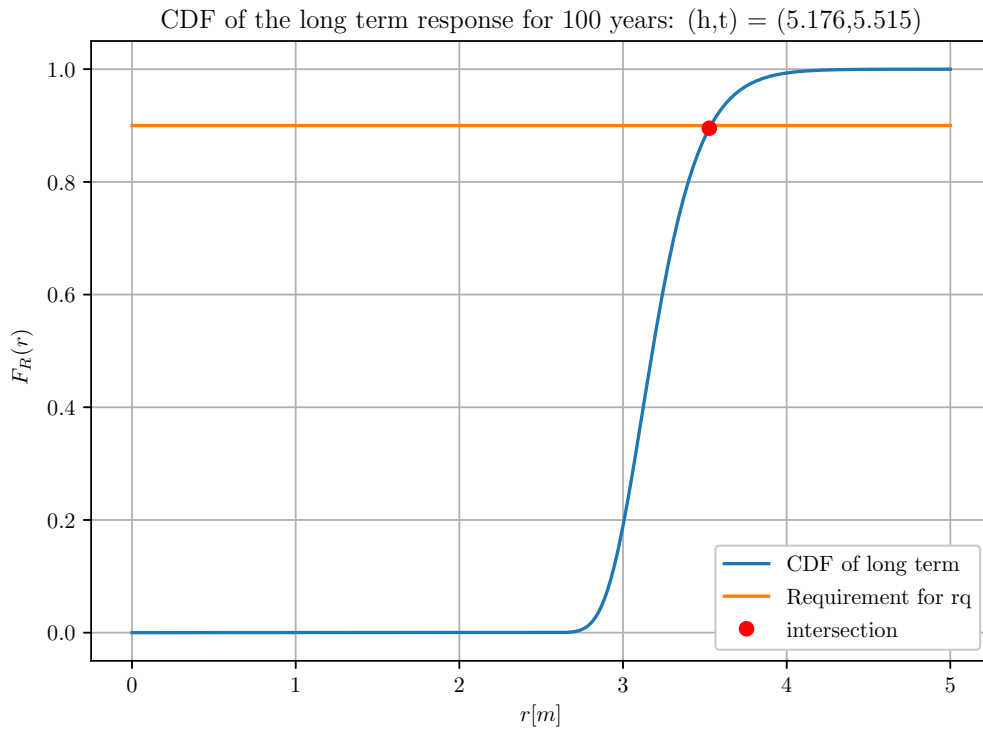


Figure C.1.5: $p = 0.90$, $M = 100$.

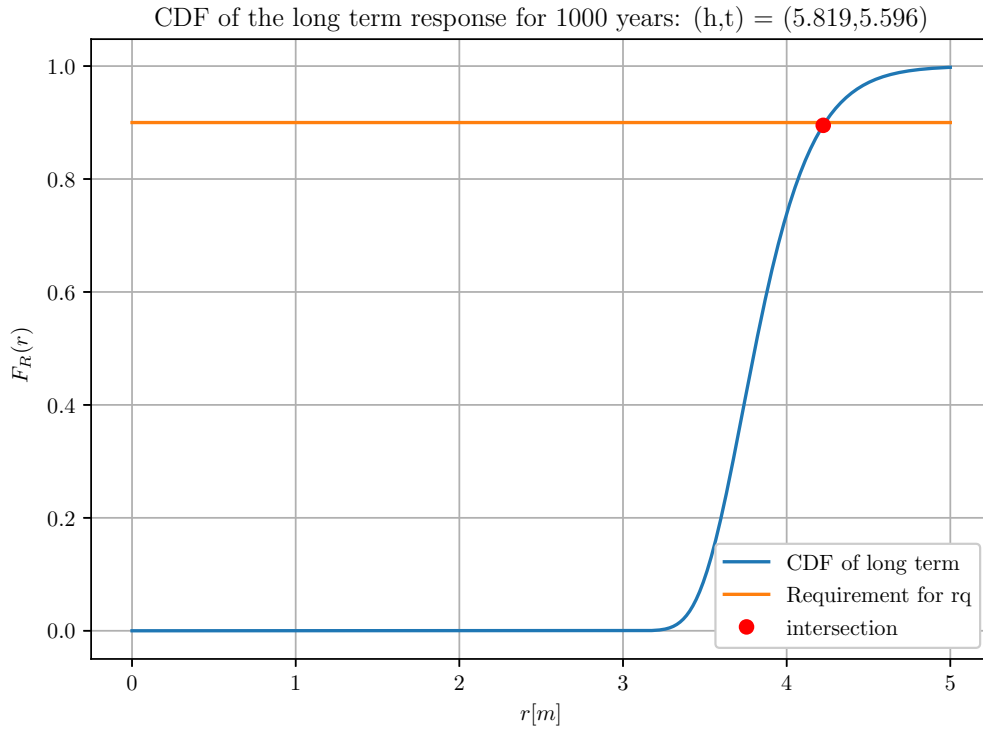


Figure C.1.6: $p = 0.90$, $M = 1000$.

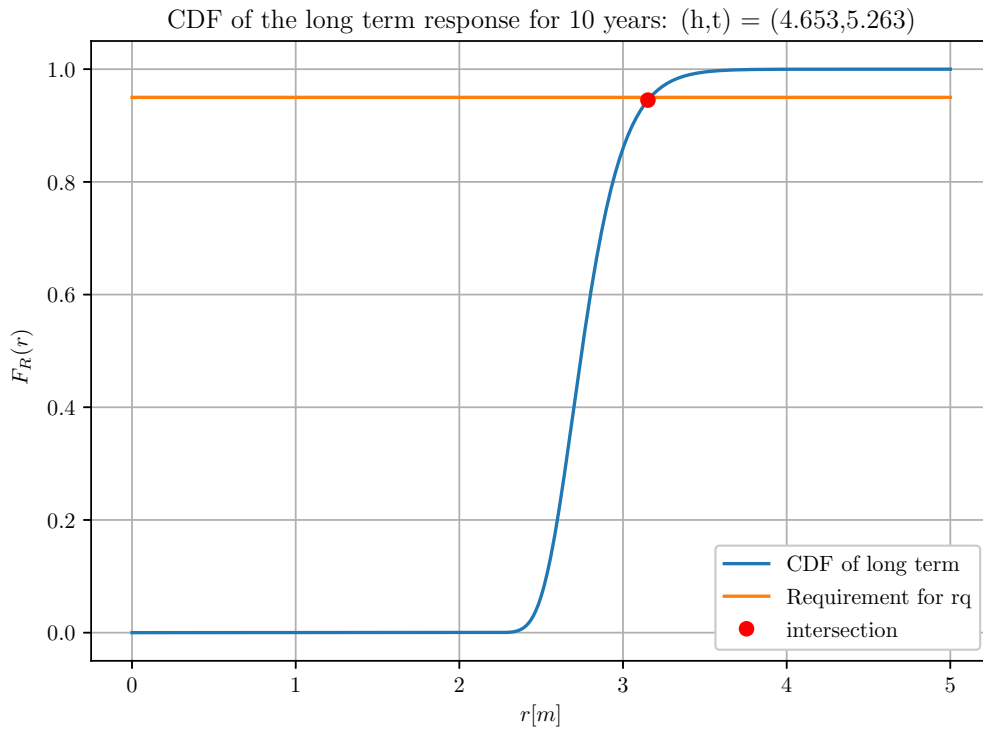


Figure C.1.7: $p = 0.95$, $M = 10$.

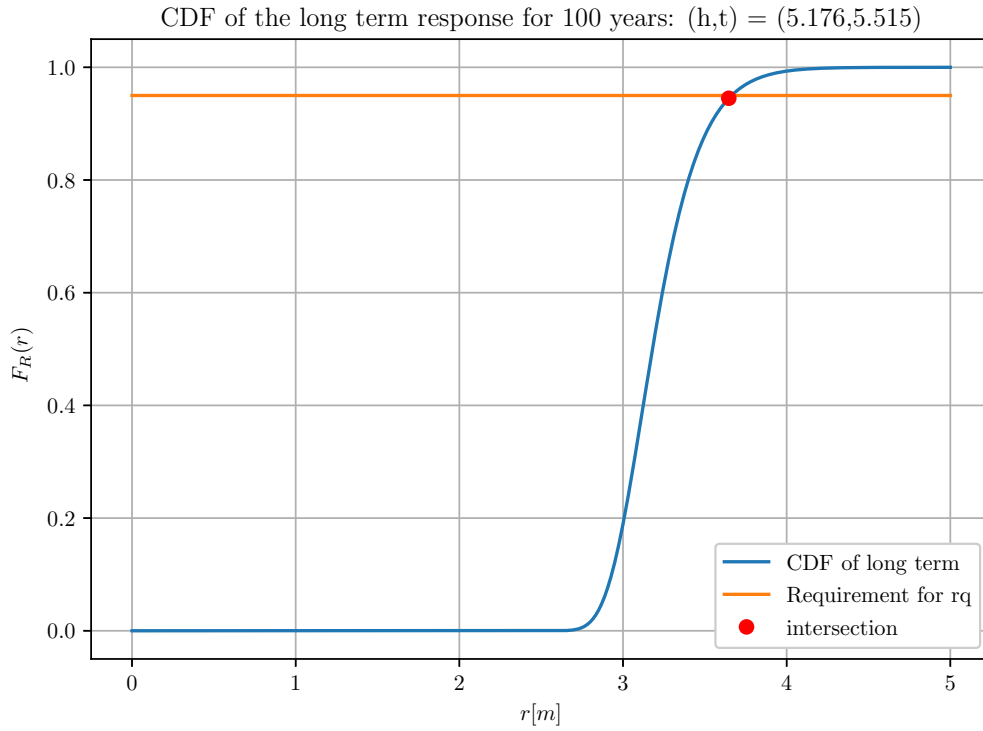


Figure C.1.8: $p = 0.95$, $M = 100$.

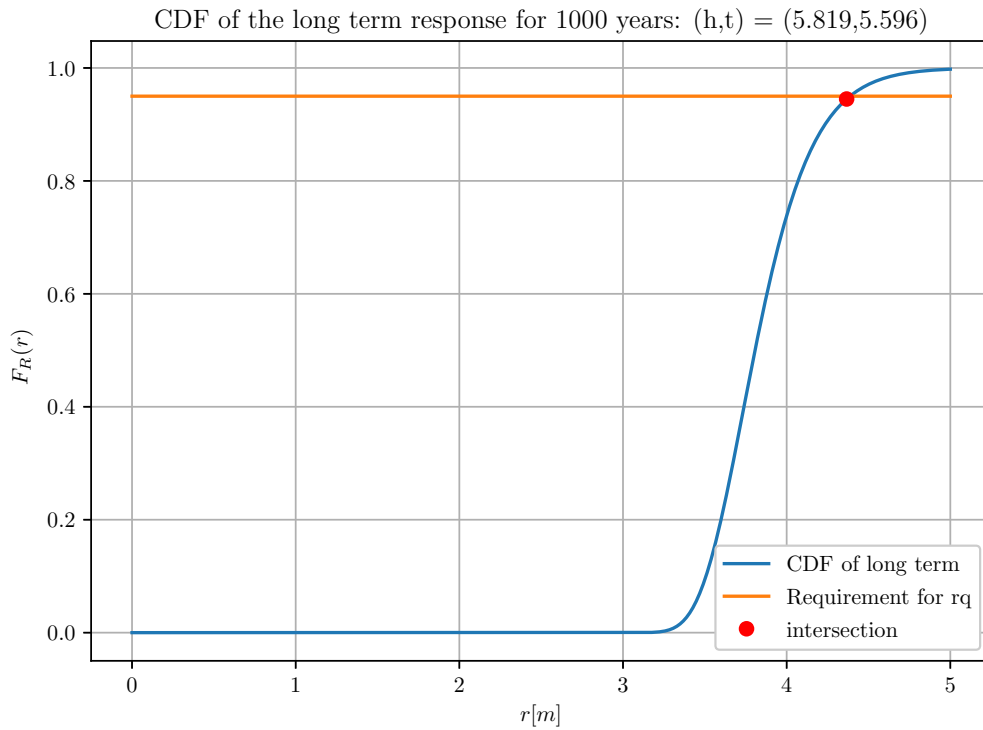


Figure C.1.9: $p = 0.95$, $M = 1000$.

